STRUCTURE and *fluorescence* of *photonic colloidal* CRYSTALS

STRUCTURE and *fluorescence* of *photonic colloidal* CRYSTALS

ACADEMISCH PROEFSCHRIFT

ter verkrijging van de graad van doctor
aan de Universiteit van Amsterdam,
op gezag van de Rector Magnificus
prof. dr. J. J. M. Franse
ten overstaan van een door het college voor promoties
ingestelde commissie in het openbaar te verdedigen
in de Aula der Universiteit
op dinsdag 9 november 1999 te 15.00 uur

door

mischa megens

geboren te ’s-Hertogenbosch

Promotor	Prof. Dr. A. Lagendijk
Copromotor	Dr. W. L. Vos
Commissie	Dr. A. van Blaaderen
	Prof. Dr. J. F. van der Veen
	Prof. Dr. J. W. Verhoeven
	Dr. G. H. Wegdam
	Prof. Dr. C. Weisbuch
Paranimfen	Toeja Megens
	Feike Hacquebord

Faculteit Wiskunde, Informatica, Natuurkunde en Sterrenkunde

This work is part of the research program of the “Stichting voor Fundamenteel Onderzoek der Materie (FOM)”, which is financially supported by the “Nederlandse Organisatie voor Wetenschappelijk Onderzoek (NWO)”.

Cover: colloidal crystals of silica-1 spheres in deionized water, illuminated from the back, and magnified about 120×. The radius of the spheres is 138 nm.

Contents

1
Introduction

1.1 Spontaneous emission

It is now commonly accepted that spontaneous emission is not an immutable property of the emitter, but it depends on the density of modes of the light field at the location of the emitter. This dependence was originally noted by Purcell[1] and it is embodied in Fermi's Golden Rule.[2] According to the Golden Rule, the rate of emission can be interpreted as the product of the square of the transition matrix element with the density of states. In this picture, the transition dipole moment of the emitter couples to the zero-point fluctuations of the electric field. The change in spontaneous emission can also be understood semiclassically, as an impedance of the surrounding medium or as a back action of the environment on the emitter. Experimentally, the influence of the density of modes was first demonstrated by Drexhage in 1966,[3] in his measurements of the excited state lifetime of europium ions at various distances from a metallic mirror. More recently, the field of quantum optics has witnessed a flourishing of sophisticated experiments, demonstrating that the spontaneous emission rate can be enhanced or reduced with respect to vacuum by placing emitters in a high-quality resonant or non-resonant cavity, respectively.[4–6] For light, currently no more than partial suppression is achieved (lifetimes extended by up to a factor of 2 in refs. 3,7), in small volumes,[5,7,8] and in a narrow wavelength range.[4] Photonic crystals promise the complete suppression of spontaneous emission over extended spatial volumes and large bandwidths.

1.2 Photonic crystals

Photonic crystals are three-dimensional periodic dielectric structures in which the refractive index varies on lengths of the order of the wavelength of light.[9–12] The propagation of light in such photonic materials is analogous to the well-known wave-like propagation of electrons in crystalline solids.[13,14] The periodic structure gives

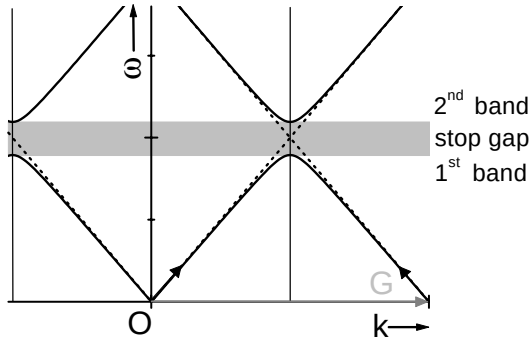

Figure 1.1 *Dispersion relation in a homogeneous medium (···), The band structure is obtained from a two-band model. The photonic strength* Ψ *is* 0.2.

rise to Bragg diffraction, that is associated with stop bands for propagation in certain directions. If the light is very strongly coupled to the crystal, a photonic band gap is expected, a frequency band in which no light can propagate through the crystal in *any* direction. One of the most important consequences of photonic band gaps is that spontaneous emission of excited atoms with a transition frequency in the gap is inhibited.[9,15] This inhibition of emission is expected to lead to novel phenomena in optics and quantum optics[9,12] and may serve as the basis for lasers without threshold[16] and highly efficient light emitting diodes.[17]

1.3 Photonic band structure

In Fig. 1.1 we show the dispersion relation, the relation between the wavevector $\mathbf{k}$ and the frequency ω, both of a homogeneous medium and of a photonic crystal. In the homogeneous medium, the optical modes are plane waves with a linear dispersion relation, the straight lines $\omega = ck$. In analogy with the electron wavefunctions in a crystalline solid, the optical modes in a periodic material are Bloch waves, functions that have the periodicity of the lattice with an additional phase factor $\exp(i\mathbf{k}\cdot\mathbf{r})$.[13,14] Periodic structures can diffract a wave, changing the wavevector by a reciprocal lattice vector; the dispersion relation of the diffracted wave is indicated by the straight line dispersion relation that is shifted by a reciprocal lattice vector $\mathbf{G}$. The two waves correspond to an incident and a reflected wave. The straight lines intersect at the edge of the Brillouin zone. In photonic crystals, the variation of the refractive index causes splittings at the edge of the Brillouin zone,

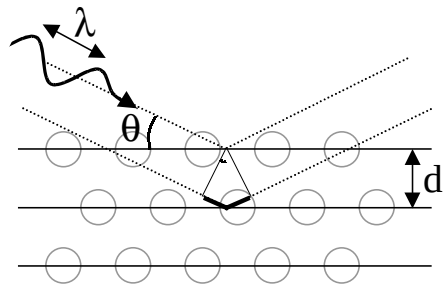

Figure 1.2 *Bragg reflection occurs when light reflected from a set of lattice planes interferes constructively; the extra path length indicated by the thick line equals an integral number of wavelengths.*

producing bands separated by stop gaps. Bloch waves with frequencies in the bands resemble normal plane waves. Toward the edge of a band, the Bloch waves become standing waves. The nodes of the low frequency mode occur predominantly in the high refractive index material, the modes of the high frequency mode occur in the low refractive index material.[18] Waves with frequencies within the stop gaps are Bragg reflected and cannot propagate through the crystal.

1.4 Bragg reflection

Bragg reflection plays a prominent role in optical experiments on photonic crystals. It occurs whenever there is constructive interference of waves reflected from a set of lattice planes, as illustrated in Fig. 1.2. The reflection appears only for specific wavelengths λ and angles θ, given by Bragg's law $2d\sin\theta = n\lambda$, where d is the distance between lattice planes and the integer n is the order of Bragg reflection. If a crystal is sufficiently well-ordered that the reflections from many lattice planes interfere constructively, then the Bragg reflection will be very strong, close to 100%. The associated extinction will be very large, increasing exponentially with sample thickness. Light cannot propagate in the direction of a Bragg reflection: the Bragg reflections correspond to the stop gaps in the photonic band structure.

If light is strongly diffracted by the scatterers, then a small number of lattice planes suffice to reflect an incident wave. The wavelength λ and angle θ then do not need to conform to Bragg's law exactly: the interference still will be constructive for the limited number of lattice planes involved. As a consequence, the Bragg reflections extend over a range of frequencies, corresponding to the width of the stop gaps.

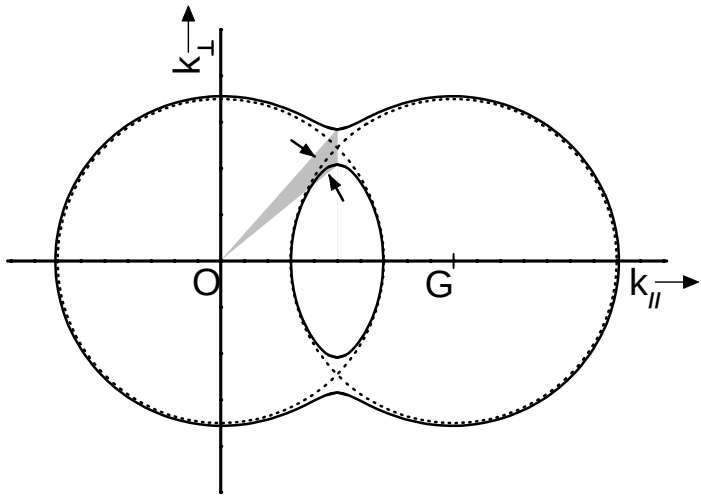

Figure 1.3 *Dispersion surface at fixed frequency according to dynamical diffraction theory, in a photonic crystal (—) and in a homogeneous medium (···). The arrows indicate the angular width of the stop gap (shaded). The photonic strength* Ψ *is* 0.15*. Only perpendicular polarization is shown.*

1.5 Dynamical diffraction

If the interaction between light and a photonic crystal is very strong, the stop gaps in all directions will overlap, creating a band gap. Spontaneous emission at frequencies within a band gap will be inhibited. If the interaction is not so strong, then the stop gaps will cover only part of the available directions for emission, as indicated in Fig. 1.3. The modification of the spontaneous emission rate will be proportionally smaller.

A clear illustration of the connection between the stop gaps and the spontaneous emission rate is provided by dynamical diffraction theory (as opposed to kinematical diffraction, ordinary Bragg reflection).[19] The theory considers reflections at a fixed wavelength. In free space, the wavevector $\mathbf{k}$ traces out a sphere of radius $k = \omega/c$ at fixed frequency. The intersection of this sphere with a plane is shown in Fig. 1.3 as a circle. The dynamical diffraction theory usually considers two such circles, corresponding to the incident and the reflected wave. The centers of the circles are one reciprocal lattice vector $\mathbf{G}$ apart. At the intersection of the spheres the dispersion curves split, due to the interaction between the waves. The splitting produces a stop gap, like in Fig. 1.1, but as a function of diffraction angle instead of frequency. The stop gaps cover only a small range of directions, unless the light is very strongly coupled to the photonic crystal.

One would expect that light emitted in the direction of a stop gap is attenuated, whereas the light can propagate perfectly well in other directions. This propagating light is observed outside the crystal, as we show in chapter 5. Contrary to expectations, light is observed to emerge also in the direction of the stop gaps. This light originates from emission in the other directions. The emitted light is scattered in the direction of stop gaps by a small concentration of defects that always occur in any crystal. As a result, light is observed even in the direction of stop gaps. In the presence of a photonic band gap, the scattered light is strongly attenuated because the stop gaps extend over all directions. Thus the spectrum of sources inside photonic crystals reveals unambiguously whether a photonic band gap has been achieved. Furthermore, the scattering relates the photonic crystals to the disordered photonic materials: the periodic structure of a photonic crystal could facilitate the localization of light, vigorously pursued in multiply scattering media.[10,20]

1.6 Photonic strength

The interaction strength between light and a photonic crystal can be conveniently expressed by a parameter Ψ defined as the ratio of the optical volume per particle – the polarizability $4\pi\alpha$ – to the physical volume per particle V.[21] This concept of photonic strength applies both for dielectric media and for atoms in optical lattices.[22] For dielectrics, the spatial variation of the refractive index appears in the polarizability $4\pi\alpha$ via the ratio m of the refractive indices of the particles and the surrounding medium. As an illustration we have plotted this photonic strength Ψ for polystyrene and silica spheres in water as a function of filling fraction φ in Fig. 1.4. In the same plot, we also show the width of the lowest stop gap obtained from numerical band structure calculations. It turns out that the photonic strength Ψ closely approximates the stop gap width. This supports the merit of Ψ as a measure of the strength of interaction between light and a crystal.

The coupling strength Ψ between light and photonic crystals has a clear optimum as a function of the volume fraction φ occupied by the spheres. With increasing volume fraction, the coupling first increases because of the increasing size of the scatterers; at higher volume fractions it decreases because the crystal scatters less efficiently. At high sphere densities the roles of the spheres and the liquid are reversed: the light is diffracted by the liquid in between the spheres and the spheres act as background medium. To illustrate this, we have also plotted the photonic strength parameter Ψ with an inverted refractive index ratio in Fig. 1.4. This photonic strength more closely approximates the numerically obtained widths at high densities.

1.7 Making photonic crystals

Yablonovitch was the first to demonstrate the feasibility of creating a photonic band gap for microwaves, using a structure of drilled holes.[9,23] Although disputed at first,[24,25] the existence of microwave band gaps is now firmly established. Yablonovitch suggested to use the same approach to create a photonic band gap for visible light. Indeed photonic structures have been realized for far infrared wavelengths, by etching instead of drilling the holes,[26] but the etching technique is not readily extended to submicron length scales; current nanotechnology focuses mainly on patterning two-dimensional surfaces rather than making three-dimensional structures.[27] Nevertheless, heroic attempts have been made to create three-dimensional crystals by etching. The largest structure to date measures 16 stacked two-dimensional layers comprising one unit cell.[28] Creating large three-dimensional regular structures of dielectric scatterers with wavelength size has proven to be a major technological challenge. Our approach is to use self-organizing colloidal suspensions of small spheres.

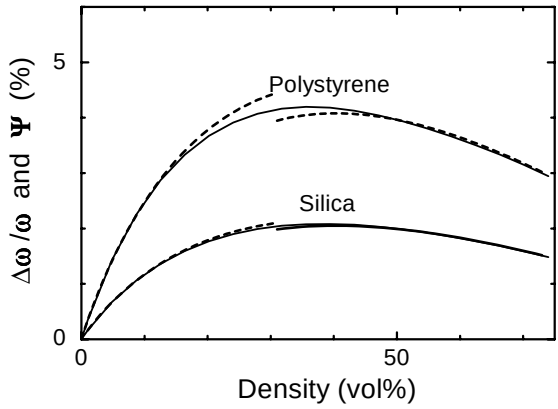

Figure 1.4 *Photonic strength parameter* Ψ *(- -) and relative (111) stop gap width* $\Delta\omega/\omega$ *(—) as a function of density, for fcc lattices of polystyrene or silica spheres in water (refractive index contrast* $m = 1.59/1.33 = 1.20$ *and* $m = 1.45/1.33 = 1.09$*). The photonic strength is obtained using* m *at low densities and* $1/m$ *at high densities. The stop gap widths result from numerical band structure calculations.*

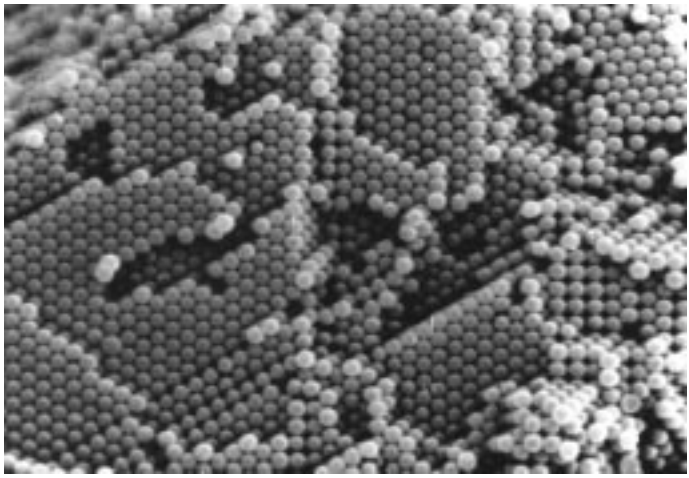

Figure 1.5 *Scanning electron micrograph of a three-dimensional crystal of polystyrene spheres with radii of* 213 *nm. Picture courtesy of J. Wijnhoven.*

1.8 Colloidal crystals

Colloids are very suitable to realize photonic materials since they naturally possess the right size and spontaneously form bulk three-dimensional crystals. The periodicity of the material makes Bragg reflections appear as a beautiful iridescence. Colloidal crystals can be produced artificially, but they also occur naturally.[29] A familiar example is the precious gem opal, which consists of silicate particles.[30] An example of such a crystal is shown in Fig. 1.5.

It is crucial to know the structure of self-organizing photonic colloidal crystals, since their optical properties are intimately connected to the crystal structure. For dilute or index matched colloids, the crystal structure is accurately known, but not for dense colloids with strong refractive index variations, desirable for photonic crystals. The strong interaction between photonic crystals and light causes multiple scattering which hampers structure determination by light scattering or other optical methods.[21] Therefore, we have performed a synchrotron small angle x-ray scattering study, see chapters 7 and 8. We observe large numbers of x-ray Bragg diffraction peaks of photonic colloidal single crystals. The colloidal particles order in face centered cubic (fcc) structures, with a high degree of localization about their lattice sites. This is an excellent starting point for photonic band gap crystals.[31] These results have both encouraged the search for materials with a full photonic band gap based on colloids, and they have stimulated interest in x-ray diffraction as a tool for colloid research.

Colloidal spheres can be doped with fluorescent dye molecules[32,33] to observe the influence of photonic band structure on the spontaneous emission. Fluorescent dyes are very suitable because of their high quantum efficiency and ease of excitation. Fluorescent dye molecules are sensitive not only to the photonic band structure however; they are also affected by chemical interactions with their environment[34] and they influence each other directly via nonradiative electromagnetic interactions when they are close together, see chapter 3. In the study of spontaneous emission in photonic crystals, these interactions are intolerable so low dye concentrations and appropriate shielding of the dye molecules are essential.

We have specially prepared silica spheres with a suitably low dye content to study photonic effects. From these colloidal spheres, we have grown crystals with wide stop bands. The stop gaps extend over ~ 15 nm in wavelength, a substantial part of the dye's emission spectrum. The crystals have dimensions up to 0.5 mm, so they affect the density of modes over an extended spatial volume. The screened Coulomb interaction of our charged spheres provides considerable flexibility: the density of the crystals can be tuned via the ionic strength of the suspending liquid. The crystal densities are optimal from a photonic point of view, see Fig. 1.4, and the stop gaps in the photonic band structure overlap with the dye's emission spectrum.

1.9 The optimal photonic crystal

The strength of the interaction between light and a photonic crystal depends critically on the relative spatial variation of the refractive index. Creating a complete photonic band gap requires both a sufficiently large refractive index contrast m, a suitable crystal structure, and an optimal filling fraction, see Fig. 1.4. Initially the fcc crystal structure was considered the best candidate, since this structure has the most spherical Brillouin zone.[9,23] However, it turned out that for spherical scatterers on an fcc lattice there is no band gap between the lowest bands due to a polarization degeneracy. Early theoretical investigations considered only scalar waves. Light has a polarization however, so one should consider vector waves for accurate photonic band structure calculations. It turns out that creating a band gap for vector waves is much more challenging than for scalar waves.[23,35] Calculations for a fcc lattice of spherical scatterers indicate that a band gap will open up between the 8^{th} and the 9^{th} branch of the dispersion relation for refractive index ratios $m > 2.9$.[31,36] The optimal filling depends on the refractive index contrast. As a rule of thumb, the optical path lengths in the high and low index materials should be equal, to enhance interference. As a consequence, a proportionately lower density of high index material is favorable.

Very recently a new class of strongly photonic crystals has been developed,[37,38]

having the appropriate density of high index material and a favorable connected structure.[39] The crystals are made by filling the voids in an artificial opal with a solid of high refractive index and subsequently removing the opal. In this way, crystals of air spheres in titania (TiO_2) could be synthesized.[37] These three-dimensional crystals currently hold the record of the strongest photonic interaction, almost forming a band gap.[40] The fabrication technique is rapidly becoming the method of choice for the synthesis of strongly photonic crystals,[41] as it holds great promise for the near future. Experiments are underway to make air-sphere crystals of semiconductors, with a refractive index of more than 3, which would open up a full photonic band gap at optical frequencies.

References

1. E. M. Purcell, 'Spontaneous emission probabilities at radio frequencies", *Phys. Rev.* **69**, 681 (1946).
2. E. Fermi, 'Quantum theory of radiation', *Rev. Mod. Phys.* **32**, 87-132 (1932).
3. K. H. Drexhage, 'Influence of a dielectric interface on fluorescence decay time', *J. Lumin.* **1**, 693-701 (1970).
4. D. J. Heinzen, J. J. Childs, J. E. Thomas, and M. S. Feld, 'Enhanced and Inhibited Visible Spontaneous Emission by Atoms in a Confocal Resonator', *Phys. Rev. Lett.* **58**, 1320-1323 (1987).
5. W. Jhe, A. Anderson, E. A. Hinds, D. Meschede, L. Moi, and S. Haroche, 'Suppression of spontaneous decay at optical frequencies: Test of vacuum-field anisotropy in confined space', *Phys. Rev. Lett.* **58**, 666-669 (1987).
6. S. Haroche, in *Systèmes fondamentaux en optique quantique/Fundamental systems in quantum optics*, edited by J. Dalibard, J.-M. Raimond, and J. Zinn-Justin (North-Holland, Amsterdam, 1992), pp. 767-940.
7. P. T. Worthing, R. M. Amos, and W. L. Barnes, 'Modification of the spontaneous emission rate of Eu^{3+} ions embedded within a dielectric layer above a silver mirror', *Phys. Rev. A* **59**, 865-872 (1999).
8. F. De Martini, G. Innocenti, G. R. Jacobovitz, and P. Mataloni, 'Anomalous spontaneous emission time in a microscopic optical cavity', *Phys. Rev. Lett.* **59**, 2955-2958 (1987).
9. E. Yablonovitch, 'Inhibited spontaneous emission in solid-state physics and electronics', *Phys. Rev. Lett.* **58**, 2059-2062 (1987).
10. S. John, 'Strong localization of photons in certain disordered dielectric superlattices', *Phys. Rev. Lett.* **58**, 2486-2489 (1987).
11. *Development and applications of materials exhibiting photonic band gaps*, edited by C. M. Bowden, J. P. Dowling, and H. O. Everitt. ", *J. Opt. Soc. Am.*

B **10**, special issue (1993).
12. *Photonic band gap materials*, edited by C. M. Soukoulis, NATO ASI Vol. E: 315 (Kluwer, Dordrecht 1996).
13. N. W. Ashcroft and N. D. Mermin *Solid state physics* (Holt, Rinehart, and Winston, New York, 1976).
14. C. Kittel, *Introduction to solid state physics* (Wiley, New York, 1986).
15. V. P. Bykov, 'Spontaneous emission from a medium with a band structure', *Sov. J. Quant. Electron.* **4**, 861-871 (1974).
16. Y. Yamamoto and R. E. Slusher, 'Optical processes in microcavities', *Phys. Today* **46 no. 6**, 66-72 (1993); S. John, in Ref. 12, p. 563.
17. J. D. Joannopoulos, P. R. Villeneuve, and S. Fan, 'Photonic crystals: putting a new twist on light', *Nature* **386**, 143-149 (1997).
18. J. D. Joannopoulos, R. D. Meade, and J. N. Winn, *Photonic crystals: molding the flow of light* (Princeton, NJ, 1995).
19. J. M. Cowley, *Diffraction physics* (North-Holland, Amsterdam, 1990).
20. D. S. Wiersma, P. Bartolini, A. Lagendijk, and R. Righini, 'Localization of light in a disordered medium', *Nature* **390**, 671-673 (1997); F. Scheffold, R. Lenke, R. Tweer, and G. Maret, 'Localization or classical diffusion of light?', *Nature* **398**, 206-207 (1999).
21. W. L. Vos, R. Sprik, A. van Blaaderen, A. Imhof, A. Lagendijk, and G. H. Wegdam, 'Strong effects of photonic band structures on the diffraction of colloidal crystals', *Phys. Rev. B* **53**, 16231-16235 (1996); ''Erratum", *ibid.* **55**, 1903 (1997); In ref. 12, p. 107.
22. P. S. Jessen and I. H. Deutsch, 'Optical lattices', *Adv. At. Mol. Opt. Phys.* **37**, 95-138 (1996).
23. E. Yablonovitch and T. J. Gmitter, 'Photonic band structure: The face-centered-cubic case', *Phys. Rev. Lett.* **63**, 1950-1953 (1989);
    E. Yablonovitch, T. J. Gmitter, and K. M. Leung, 'Photonic band structure: The face-centered-cubic case employing nonspherical atoms', *ibid.* **67**, 2295-2298 (1991).
24. J. Maddox, 'Photonic band-gaps bite the dust', *Nature* **348**, 481 (1990).
25. E. Yablonovitch and K. M. Leung, 'Hope for photonic bandgaps', *Nature* **351**, 278 (1991).
26. R. Biswas, E. Ozbay, and K. M. Ho, 'Photonic band gaps with layer-by-layer double-etched structures', *J. Appl. Phys.* **80**, 6749-6753 (1996).
27. T. F. Krauss, R. M. De La Rue, and S. Brand, 'Two-dimensional photonic-bandgap structures operating at near-infrared wavelengths', *Nature* **383**, 699-702 (1996);
    D. Labilloy, H. Benisty, C. Weisbuch, T. F. Krauss, R. M. De La Rue, V. Bardinal, R. Houdr, U. Oesterle, D. Cassagne, and C. Jouanin, 'Quantitative mea-

surement of transmission, reflection, and diffraction of two-dimensional photonic band gap structures at near-infrared wavelengths', *Phys. Rev. Lett.* **79**, 4147-4150 (1997).

28. N. Yamamoto and S. Noda, 'Fabrication and optical properties of one period of a three-dimensional photonic crystal operating in the 5-10 μm wavelength region', *Jpn. J. Appl. Phys.* **38**, 1282-1285 (1999).
29. R. J. Hunter, *Foundations of colloid science* (Clarendon, Oxford, 1992).
30. J. V. Sanders, 'Colours of precious opal', *Nature* **204**, 1151-1153 (1964).
31. H. S. Sözüer, J. W. Haus, and R. Inguva, 'Photonic bands: Convergence problems with the plane-wave method', *Phys. Rev. B* **45**, 13962-13972 (1992).
32. A. van Blaaderen and A. Vrij, 'Synthesis and characterization of colloidal dispersions of fluorescent, monodisperse silica spheres', *Langmuir* **8**, 2921-2931 (1992).
33. N. A. M. Verhaegh and A. van Blaaderen, 'Dispersions of Rhodamine-labeled silica spheres: synthesis, characterization, and fluorescence confocal scanning laser microscopy', *Langmuir* **10**, 1427-1438 (1994).
34. H. J. Verhey, B. Gebben, J. W. Hofstraat, and J. W. Verhoeven, 'Detection of nanoscale events in dispersed polymer particles containing a charge-transfer fluorescence probe', *J. Polymer Sci.* **33**, 399-405 (1995).
35. K. M. Ho, C. T. Chan, and C. M. Soukoulis, 'Existence of a photonic gap in periodic dielectric structures', *Phys. Rev. Lett.* **65**, 3152-3155 (1990).
36. K. Busch and S. John, 'Photonic band gap formation in certain self-organizing systems', *Phys. Rev. E* **58**, 3896-3908 (1998).
37. J. E. G. J. Wijnhoven and W. L. Vos, 'Preparation of photonic crystals made of air spheres in titania', *Science* **281**, 802-804 (1998).
38. B. T. Holland, C. F. Blanford, and A. Stein, 'Synthesis of macroporous minerals with highly ordered three-dimensional arrays of spheroidal voids', *Science* **281**, 538-540 (1998).
39. E. N. Economou and M. M. Sigalas, 'Classical wave propagation in periodic structures: cermet versus network topology', *Phys. Rev. B* **48**, 13434-13438 (1993).
40. M. S. Thijssen, R. Sprik, J. E. G. J. Wijnhoven, M. Megens, T. Narayanan, A. Lagendijk,and W. L. Vos, 'Inhibited light propagation in photonic air-sphere crystals', *Phys. Rev. Lett.* **Oct.**, (1999).
41. A. A. Zakhidov, R. H. Baughman, Z. Iqbal, C. X. Cui, I. Khayrullin, S. O. Dantas, I. Marti, and V. G. Ralchenko, 'Carbon structures with three-dimensional periodicity at optical wavelengths', *Science* **282**, 897-901 (1998);
S. H. Park and Y. Xia, 'Macroporous membranes with highly ordered and three-dimensionally interconnected spherical pores', *Adv. Mater.* **13**, 1045-1048 (1998);

Y. A. Vlasov, N. Yao, and D. J. Norris, ‘Synthesis of photonic crystals for optical wavelengths from semiconductor quantum dots’, *Adv. Mater.* **11**, 165-168 (1999);
G. Subramania, K. Constant, R. Biswas, M. M. Sigalas, and K.-M. Ho, ‘Optical photonic crystals fabricated from colloidal systems’, *Appl. Phys. Lett.* **74**, 3933-3935 (1999).

2

Transmission and diffraction by photonic colloidal crystals

2.1 Introduction

The ambition of extensive research efforts on photonic crystals is to increase the coupling between light and a photonic crystal. A strong coupling will lead to new effects such as localization of light or inhibition of spontaneous emission.[1,2] The coupling strength between light and a crystal can be expressed by a parameter Ψ defined as the ratio of the optical volume per particle - the polarizability - to the physical volume per particle.[3] Several optical studies have already been reported on weakly photonic colloidal crystals ($\Psi < 0.05$), see ref. 4–6. In particular, Tarhan and Watson[7] have resolved the stop bands and the dispersion curves in a colloidal single crystal. The coupling strength Ψ between light and photonic crystals can be increased by using colloids with a higher refractive index and by raising the volume fraction φ of the particles. The effect of increased volume fraction has been investigated in optical diffraction experiments on colloidal crystals with refractive index ratios m of the particles and the medium of up to 1.45, and $\Psi < 0.6$.[3] It was found that the photonic band structures result in *apparent* Bragg spacings that strongly depend on the wavelength of light.[3] If a photonic material is sufficiently well-ordered, the Bragg reflections acquire a finite width. This width is inherently photonic, *i.e.* it is not due to finite crystal size or scattering from defects. The stop band width is directly related to the photonic strength Ψ, therefore the width is pertinent to the assessment of a photonic crystal's coupling strength. Here we present measurements of stop bands in the transmission of colloidal crystals.

2.2 Experiment

We have investigated the effects of volume fraction on the transmission of colloidal crystals, whose structure and orientation was determined by small angle x-ray scattering. We have grown colloidal crystals from polystyrene and silica particles with radii r between 100 and 220 nm, suspended in water, methanol, ethanol, or dimethylformamide. Polystyrene colloids were bought from Duke Scientific, silica colloids were made by Stöber synthesis.[8] The samples were sealed in glass capillaries (Vitro Dynamics). Crystals with volume fractions $\varphi > 50\%$ were made by sedimentation under gravity. Crystals with lower volume fractions were made by deionizing the dispersions with resin (BioRad AG501-X8) and adding resin to the capillaries. Optical transmission spectra were measured using a BioRad FTS60A fourier transform spectrometer and a high pressure xenon lamp. The spectra were referenced to the supernatant liquid or to empty capillaries. Knowledge of the crystal structure and orientations is essential to interpret the optical experiments. We determined the structure and orientation of the crystals using small angle x-ray diffraction. This technique probes a much wider range in reciprocal space than optical diffraction, which considerably facilitates structure identification. Moreover, the interpretation of x-ray diffraction is not compounded by multiple scattering effects. The use of a synchrotron beam[9] proves to be a key asset, because the beam can be focused to a small spot, while retaining enough flux to keep collection times reasonable.

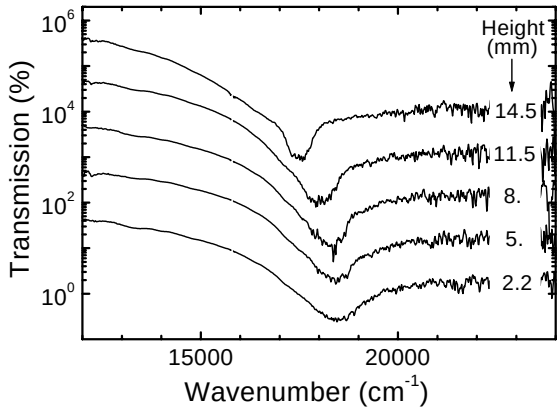

Figure 2.1 *Optical transmission spectra for various heights in a sedimented colloidal crystal of polystyrene spheres in methanol (sample #232). The radius of the spheres is* 100.9 ± 0.5 *nm, the size variation is only* 2.1%. *The curves for heights beyond* 2.2 *mm have been offset by a factor of* 10 *for clarity; the heights are indicated on the right hand side.*

2.3 Transmission spectra

Optical transmission spectra at various heights in a polycrystalline sample of polystyrene spheres in methanol are shown in Fig. 2.1. The transmissions have a clear minimum at a frequency of about 18000 cm^{-1}. This minimum corresponds to a wavelength of ~ 550 nm for Bragg diffraction in back reflection. It is associated with the stop gap in the L point of the Brillouin zone of fcc crystals. The corresponding lattice planes are the close-packed (111) planes oriented parallel to the cell walls. The low transmission beyond the stop band is caused by crystallites that have different orientations, hence they reflect at shorter wavelengths. The presence of such tilted crystallites was inferred from our SAXS diffraction patterns which reveal a polycrystalline average.

With increasing height, the volume fraction is expected to decrease in sedimented samples.[10] Fig. 2.1 shows that the optical frequency of the stop band decreases with increasing height. The L gap frequencies are expected to be equal to 2 times the 111 lattice spacing, multiplied by the effective refractive index of the

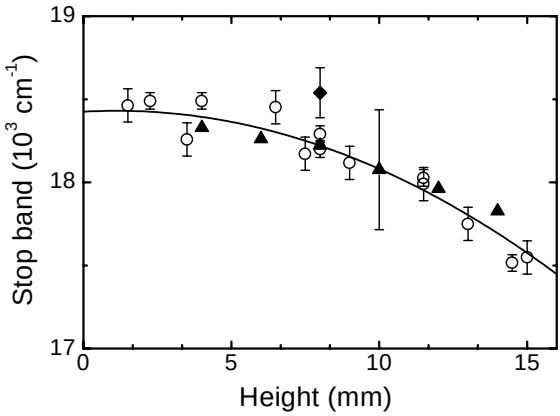

Figure 2.2 *Variation of the center frequency of the fcc L stop band with height in the sample of Fig. 2.1. The open circles are optical transmission measurements. The triangles indicate stop gap frequencies calculated from twice the 111 lattice spacing (measured by SAXS) times the Maxwell-Garnett effective refractive index; the error bar gives an indication of the accuracy. The solid diamond is from a similar calculation, but using an optically determined lattice spacing.*[3] *Note that the 111 lattice spacing is the only one that can be accessed optically. In contrast, synchrotron SAXS yields many more reflections, which demonstrates the power of this technique.*

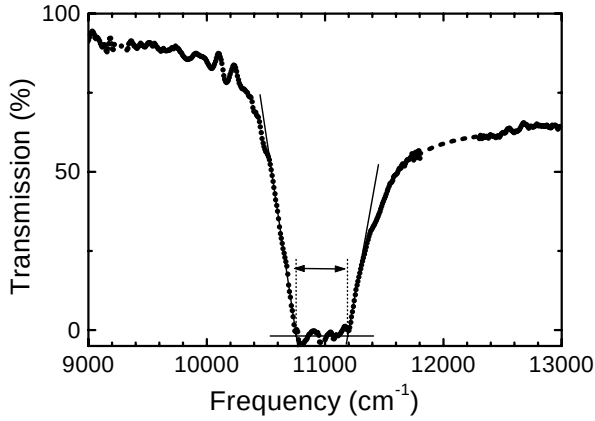

Figure 2.3 *Optical transmission spectrum of a colloidal crystal of polystyrene spheres in water (sphere radius* 111 *nm, sample #260) at a relatively low density of* 12 *vol%. The high transmission at high frequencies suggests that the sample is comparatively well ordered. The abrupt bends at low transmission on this plot with a linear scale provide a natural measure for stop band width, indicated by the arrow.*

crystal. We have accurately determined the position of the stop bands in the spectra for comparison with crystal structure information from our x-ray diffraction experiments, and from optical diffraction.[3] The results are plotted in Fig. 2.2. By using the x-ray data for the spacings and Maxwell-Garnett effective-medium theory for the refractive index,[11] we obtain good agreement. The good agreement between the two data sets is the first experimental observation demonstrating that the Maxwell-Garnett effective refractive index accurately describes the low-lying stop gaps in the band structure.

2.4 Width of the stop bands

The width of the stop bands is directly related to the strength of interaction between light and crystals, and an accurate knowledge of the stop band widths is therefore of utmost importance. The edges of the stop band are clearest at the top of the sample, where the slope of the transmission is largest, see Fig. 2.1. The attenuation in the stop band is also largest here. The distinctness of the stop band edges decreases from top to bottom in the sample, simultaneously with the crystallite size and the attenuation. Since the stop bands in Fig. 2.1 do not possess an obvious edge frequency there is inevitably some arbitrariness in choice of width.[12] Fortunately, a

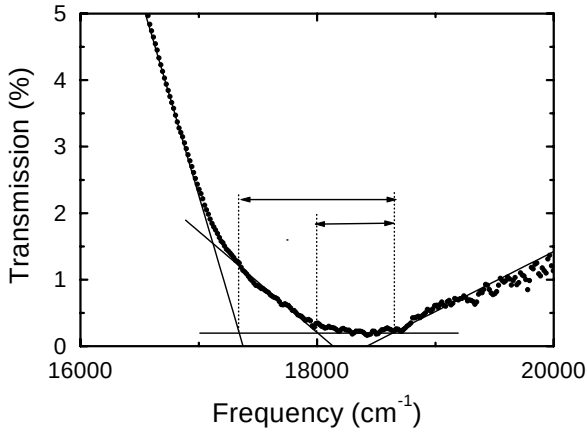

Figure 2.4 *Optical transmission as a function of wavenumber in the colloidal sample of Fig. 2.1, at a height of* 4 *mm. Two estimates for the width of the stop band, using straight line approximations for the transmission, are indicated. We used the mean of these estimates to represent the width.*

natural measure of the width is suggested by the transmission plotted on a linear scale as in Fig. 2.3. The low and high frequency edges of the transmission stop band are well approximated by straight lines. We have estimated the width from the intersection of these straight lines with a horizontal line through the transmission minimum, as indicated in Fig. 2.4.

In Fig. 2.5 we have plotted the relative widths of the L gap versus volume fraction φ for crystals of polystyrene spheres in water (refractive index ratio $m = 1.59/1.33 = 1.20$). The stop band width increases because the photonic strength increases with the density of scatterers, to $\sim 5\%$ at a volume fraction of $\sim 40\%$. Beyond this volume fraction, the width is about constant or slightly decreasing. A decrease is expected for large φ, because in the limit of a homogeneous filling (with $\varphi = 100\%$) there is no more scattering, and hence the width of the stop gaps is zero. The variation in the experimental data is attributed to disorder in the colloidal crystals, which causes smearing of the band edges. The drawn curve in Fig. 2.5 is the result of band structure calculations.[13,14] The curve increases to 4.2% at $\varphi \sim 35$ vol%, in agreement with the experimental data. As expected, the theoretical stop gap width decreases at higher volume fractions. The observation of a maximum width as a function of φ confirms earlier suggestions that the photonic strength has an optimum as a function of φ.[17,3]

A photonic strength parameter that incorporates this effect is the polarizability

per unit cell, which is also the starting point of an analysis by Spry and Kosan[19]

$$\Psi = 3\frac{m^2-1}{m^2+2}3\varphi \mathrm{j}_1(GR), \tag{2.1}$$

where G is the length of the 111 lattice vector, R is the radius of the spheres,[18] and $\mathrm{j}_1(x) = (\sin x - x\cos x)/x^3$ is proportional to the Fourier transform of a unit sphere. For normal incidence on lattice planes parallel to the crystal surface, the photonic strength Ψ is precisely equal to the relative stop band width as defined in Fig. 2.4. We have plotted the expression for Ψ in Fig. 2.5, taking $m = 1.59/1.33$ as appropriate for a high index material in a low index background like our polystyrene spheres in water. The photonic strength decreases at higher volume fractions, due to the density-dependence of the Fourier component $\mathrm{j}_1(GR)$. The photonic strength agrees well with the measured stop band widths, and it closely approximates the numerically obtained widths at low volume fractions. At high volume fractions the expression Eq. 2.1 cannot be expected to accurately predict the stop gap widths, since at high sphere densities the roles of the spheres and the liquid are reversed: the light is diffracted by the liquid in between the spheres and the spheres act as

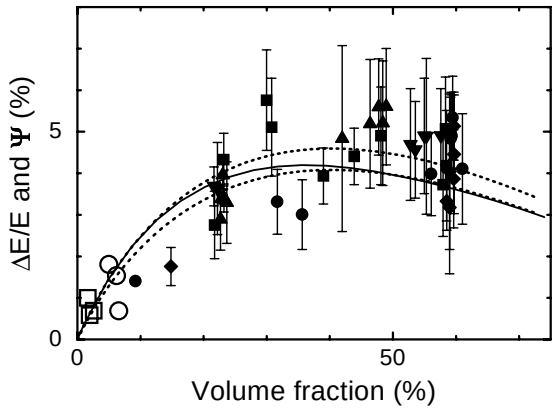

Figure 2.5 *The width of the stop gap divided by the energy of the L gap as a function of volume fraction, for crystals of polystyrene spheres in water. The open circles at low volume fractions are taken from literature.*[4–7] *The filled symbols are our results for many different samples. The error bars for the widths correspond to the two different estimates indicated in Fig. 2.4. The drawn curve is the result of numerical band structure calculations.*[14] *The dotted curves are photonic strength parameters Ψ, with $m = 1.59/1.33$ (upper dotted curve), applicable at low densities, and with $m = 1.33/1.59$ (lower dotted curve), appropriate for high densities.*

background. An inverted refractive index ratio $m = 1.33/1.59$ is therefore more appropriate. To illustrate this, we have also plotted the photonic strength parameter Ψ with the inverted refractive index ratio in Fig. 2.5. This photonic strength more closely approximates the numerically obtained widths at high densities.

The close correspondence between the photonic strength and the stop gap width contrasts remarkably with the results of a forthright two-band approximation. In a two-band model, the width of the stop gap is controlled by the Fourier component G of either $m^2 - 1$ or $1 - 1/m^2$, depending on whether one expands the electric or the magnetic field. Both the electric and the magnetic form of the stop gap width have been plotted in Fig. 2.6. Both expansions predict too large stop gap widths, whereas these same expansions form the basis of the numerical band structure calculations. Surprisingly, if one expands $(m^2-1)/(m^2+2)$, then the two-band model prediction for the stop gap width is indistinguishable from Eq. 2.1. Apparently the polarizability of a single sphere represents the interaction between light and a photonic crystal fairly well. It has even been put forward that there is a direct correspondence between the gaps calculated by plane wave expansion and the Mie resonances of an isolated sphere.[20]

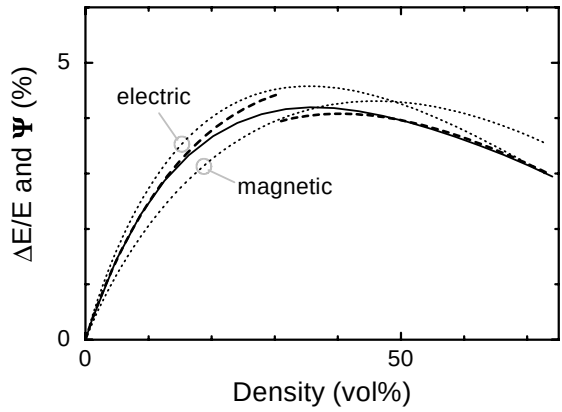

Figure 2.6 *Photonic strength parameter Ψ (- -) and relative stop gap width $\Delta E/E$ (— and $\cdots$) as a function of density, for fcc lattices of polystyrene spheres in water (refractive index contrast $m = 1.59/1.33 = 1.20$). The photonic strength is obtained using $m = 1.59/1.33$ at low densities, and with $m = 1.33/1.59$ at high densities. The stop gap widths result from numerical band structure calculations (—) and from two-band models based on expansion of the electric or the magnetic field ($\cdots$).*

2.5 Conclusions

We have investigated the effects of volume fraction on the transmission of colloidal crystals, whose structure and orientation were determined by small angle x-ray diffraction. The optical transmission spectra reveal minima corresponding to stop gaps in the photonic band structure on the edge of the Brillouin zone. The positions of the optically measured stop bands agree well with lattice spacings measured by SAXS. The stop bands have a relative width of up to 5% of the gap frequency, in accord with numerical band structure calculations. The maximum in the relative width confirms the notion that the strength of the interaction between photonic crystals and light has an optimum as a function of volume fraction. The photonic strength parameter Ψ takes this effect into consideration. It agrees well with the observed stop band widths in transmission and closely approximates the numerical results. Recently it has been shown that the stop gaps can also be measured in reflection.[21] Such reflection measurements yield very accurate results; the stop gap widths are again in excellent agreement with the photonic strength Ψ.

References

1. E. Yablonovitch, 'Inhibited spontaneous emission in solid-state physics and electronics', *Phys. Rev. Lett.* **58**, 2059-2062 (1987).
2. S. John, 'Strong localization of photons in certain disordered dielectric superlattices', *Phys. Rev. Lett.* **58**, 2486-2489 (1987).
3. W. L. Vos, R. Sprik, A. van Blaaderen, A. Imhof, A. Lagendijk, and G. H. Wegdam, 'Strong effects of photonic band structures on the diffraction of colloidal crystals', *Phys. Rev. B* **53**, 16231-16235 (1996); 'Erratum', *ibid.* **55**, 1903 (1997); In ref. 16, p. 107.
4. P. A. Rundquist, P. Photinos, S. Jagannathan, and S. A. Asher, 'Dynamical Bragg diffraction from crystalline colloidal arrays', *J. Chem. Phys.* **91**, 4932-4941 (1989).
5. Y. Monovoukas, G. G. Fuller, and A. P. Gast, 'Optical anisotropy in colloidal crystals', *ibid.* **93**, 8294-8299 (1990).
6. J. Martorell and N. M. Lawandy, 'Spontaneous emission in a disordered dielectric medium', *Phys. Rev. Lett.* **66**, 887-890 (1991).
7. Ì. Ì. Tarhan and G. H. Watson, 'Photonic band structure of fcc colloidal crystals', *Phys. Rev. Lett.* **76**, 315-318 (1996).
8. See *e.g.* A. van Blaaderen, J. van Geest, and A. Vrij, 'Monodisperse colloidal silica spheres from tetraalkoxysilanes: particle formation and growth mechanism', *J. Coll. Interf. Sci.* **154**, 481 (1992).

9. P. Bösecke, O. Diat, and B. Rasmussen, 'High-brilliance beamline at the European Synchrotron Radiation Facility', *Rev. Sci. Instrum.* **66**, 1636-1638 (1995).
10. R. Piazza, T. Bellini, and V. Degiorgio, 'Equilibrium sedimentation profiles of screened charged colloids: A test of the hard-sphere equation of state', *Phys. Rev. Lett.* **71**, 4267-4270 (1993);
M. A. Rutgers, J. H. Dunsmuir, J.-Z. Xue, W. B. Russel, and P. M. Chaikin, 'Measurement of the hard-sphere equation of state using screened charged polystyrene colloids', *Phys. Rev. B* **53**, 5043-5046 (1996).
11. J. C. Maxwell-Garnett, 'Colors in metal glasses and in metallic films', *Phil. Trans. Royal Soc. A* **203**, 385-420 (1904); 'Colors in metal glasses, in metallic films, and in metallic solutions', *ibid. A* **205**, 237-288 (1906).
12. K. W.-K. Shung and Y. C. Lai, 'Surface effects and band measurements in photonic crystals', *Phys. Rev. B* **48**, 11265-11269 (1993).
13. K. M. Leung and Y. F. Liu, 'Photon band structures: the plane-wave method', *Phys. Rev. B* **41**, 10188-10190 (1990).
14. We used the computer code of Rudolf Sprik, provided at URL 'http:// www.wins.uva.nl/ research/ scm/ sprik/ pbs.htm'. The programs use the well trusted plane wave expansion of the Maxwell equations in electric field or in magnetic field form.[15,16] We took into account 4 shells of reciprocal space points, which corresponds to 339 plane waves.
15. See *e.g.* J. D. Joannopoulos, R. D. Meade, and J. N. Winn, 'Photonic crystals; molding the flow of light', (Princeton University Press, 1995).
16. *Photonic band gap materials*, edited by C. M. Soukoulis, NATO ASI Vol. E: 315 (Kluwer, Dordrecht 1996).
17. S. John, in Ref. 16, p. 563.
18. The product *GR* only depends on volume fraction; for the 111 stop gap of an fcc lattice of spheres, $GR = 2\pi\sqrt{3}(3\varphi/16\pi)^{1/3}$. As a consequence, the expression for the photonic strength is fully determined by the volume fraction φ and the refractive indices.
19. R. J. Spry and D. J. Kosan, 'Theoretical analysis of the crystalline colloidal array filter', *Appl. Spectroscopy* **40**, 782-784 (1986).
20. E. Lidorikis, M. M. Sigalas, E. N. Economou, and C. M. Soukoulis, 'Tight-binding parametrization for photonic band gap materials', *Phys. Rev. Lett.* **81**, 1405-1408 (1998).
21. M. S. Thijssen, R. Sprik, J. E. G. J. Wijnhoven, M. Megens, T. Narayanan, A. Lagendijk, and W. L. Vos, 'Inhibited light propagation in photonic air-sphere crystals', *Phys. Rev. Lett.* **Oct.**, (1999).

3
Nonradiative energy transfer

3.1 Introduction

One of the most important consequences of photonic band structures is that spontaneous emission of excited atoms or molecules can be inhibited.[1] Fluorescent dye molecules are very suitable to observe the influence of photonic band structure on the spontaneous emission because of their high quantum efficiency and ease of excitation. However fluorescent dyes are sensitive not only to the photonic band structure, they are also affected by chemical interactions with their environment and they influence each other directly via nonradiative electromagnetic interactions when they are close together. The influence of the environment is particularly important; in fact organic dyes are utilized as sensitive probes for the chemistry of their surroundings.[2] In an early study of spontaneous emission in photonic crystals, the dye was dissolved in the liquid medium between colloidal particles.[3] Later it was recognized that chemical interactions of the dye with the particle surfaces lead to complications.[4,5]

Arguably a cleaner way to study photonic effects is to shield the dye by incorporating it inside colloidal particles, *e.g.* silica spheres,[6] so the dye's environment is constant. Incorporating dye molecules in solids compared to liquid solutions is also attractive because of the increased photostability and fluorescence yield.[7] In liquid solutions the quantum efficiencies of most organic dyes are strongly reduced when relatively low dye concentrations of $\sim 10^{-4}$ M are exceeded. This concentration quenching or self-quenching effect is due to nonradiative energy transfer between dye molecules.[8] The effect illustrates that it is crucial to identify the spectroscopic properties of a dye in its environment before studying the photonic effects.

Another interest in dyed particles stems from colloid science. Van Blaaderen *et al.* synthesized silica colloids with dye incorporated.[6] Such particles have made possible measurements of particle diffusion by fluorescence recovery after photo-

bleaching,[9] and direct imaging of dense colloidal structures by confocal fluorescence microscopy.[10] Nevertheless, several questions concerning the incorporation of dye inside colloids remain open, for example it is not clear whether the dye is dispersed homogeneously through the solid matrix of the colloids. A spectroscopic study is expected to give more insight. To elucidate how the dye is incorporated in the silica particles, we have studied the influence of the amount of labeling (the number density of dye molecules in a particle) on the spectroscopic properties.

3.2 Experimental

We studied fluorescein isothiocyanate (FITC) dye that is incorporated inside colloidal silica spheres. FITC dye was chosen because it is suitable for fluorescence recovery and confocal microscopy studies.[9,10] This fluorophore is often used for microscopy on biological samples. Many studies have investigated the spectral properties of this dye[12] and its photostability when bound to cell components.[13]

A series of colloidal dispersions was prepared following the synthesis of Stöber *et al.*,[14] and modified as described by Van Blaaderen *et al.*[6] to incorporate dye into the spheres. This procedure yields almost perfectly spherical particles with a narrow size distribution. In this case the size polydispersity, determined by transmission electron microscopy, was 6%. The final radii of the colloidal dispersions F1 to F5 are all approximately the same, only the dye concentration is doubled from one dispersion to the next, see table 3.1. The preparation is described in detail in ref. 15. After the synthesis, the spheres were resuspended in dimethylformamide (DMF), chosen to match the refractive index of the liquid to that of the particles, in order

Table 3.1 *Size of the silica spheres, as determined by transmission electron microscopy and static light scattering, the concentration c of dye inside the particles, and the average distance between dye molecules R.*

System	Radius (nm)		Dye concentration	Intermolecular
	TEM	SLS	c (mM)	separation R (nm)
F1	208	188	0.49	15.0
F2	218	194	1.18	11.2
F3	224	197	2.7	8.5
F4	237	210	6.0	6.5
F5	250	223	11.9	5.2
F6	341	305	31.	3.8

to minimize scattering effects on absorption and fluorescence properties. Samples for the time-resolved fluorescence measurements were taken from the stock dispersions and transferred to 0.4 mm thick glass capillaries (Vitro Dynamics). Decay curves were corrected for a weak long-lived luminescence from impurities in the glass of the capillaries.

The labeling efficiency was determined by dissolving the particles in a NaOH solution, liberating the dye molecules, and measuring the absorbance of the resulting transparent solutions compared to a calibration series, consisting of FITC dye dissolved in a mixture of NaOH solution and DMF. Absorption spectra were measured on dilute suspensions in 1 cm glass cuvettes with a Shimadzu Spectronic 200 UV double-beam spectrometer using DMF as a reference. Emission spectra were measured on the undiluted stock suspensions with a Bio-Rad FTS-60A Fourier-Transform Spectrometer. The samples were contained in 2.5 cm diameter cylindrical flasks and illuminated by an argon ion laser. Excitation at 458, 476.5, or 488 nm wavelength gave identical spectra. Fluorescence was detected in backscattering, to minimize the inner filter effect.

Time-resolved fluorescence curves were obtained using a time-correlated single photon counting technique,[16] see Fig. 3.1. The dye in the sample is excited in the UV at a wavelength of around 320 nm by the second harmonic of a cavity-dumped dye laser. This dye laser is synchroneously pumped by a mode-locked Nd^{3+}:YAG laser, whose output is first pulse-compressed and frequency-doubled. The actively mode-locked Nd^{3+}:YAG laser (Spectra Physics 3800) generates about 12 W of output power in TEM00 mode at 1064 nm wavelength. When the laser is

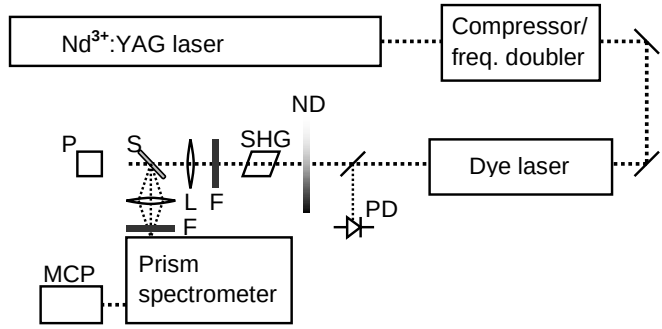

Figure 3.1 *Outline of the setup for time-resolved fluorescence measurements. PD: photodiode; ND: adjustable neutral density filter; SHG: second harmonic generating crystal; F: color filters; L: lenses; P: power meter diode; MCP: micro channel plate detector.*

mode-locked well, it produces pulses of 100–150 ps full width at half maximum (FWHM), as measured with a fast 25 GHz photodiode (New Focus). The pulses are shortened to $5-10$ ps in a pulse compressor (Spectra Physics 3595) to achieve a high peak power for second harmonic generation. When properly aligned, the system wil generate up to 950 mW of 532 nm second harmonic output; at least 600 mW is required for reliable operation. Care should be taken to avoid Q-switching of the YAG laser as this may damage the second harmonic generating crystal. The second harmonic output is stabilized by deflecting part of the infrared YAG laser beam with an acousto-optic modulator in a servo loop. This reduces the fluctuations in the second harmonic intensity, at the price of a reduction in output power. The second harmonic output was stabilized at 400 mW to comfortably pump the dye laser. The synchronously mode-locked, cavity-dumped dye laser (Spectra Physics 3500) uses Kiton Red dye in the wavelength range 600 to 660 nm. The repetition rate of the cavity dumper was 80 kHz. The output of the dye laser is frequency doubled, resulting in an excitation beam of < 1 ps pulses with a wavelength of 320 nm and a beam diameter of 1 mm at the sample. The beam power was always less than 1 μW. The sample was placed at an angle in order to prevent direct reflection from entering the detector. A Schott RG490 color filter removes the residual laser light. The fluorescence was detected at an angle of 90° to the excitation beam by a Hamamatsu R3809U micro channel plate detector. By adjusting an aperture in front of the detector, we could maintain a maximum count rate of 12 kcounts/s. The signal from the detector is amplified and fed to a constant fraction discriminator (Tennelec TC454) and time to amplitude converter (TAC, Tennelec TC864). A photodiode monitors the dye laser output for triggering the TAC. The time difference between the excitation pulse and the micro channel plate detector signal is recorded by a multi-channel analyzer. The discriminator was modified to accommodate a short delay corresponding to the risetime of the detector pulses. The zero crossing level of the discriminator was carefully optimized for best time resolution.

The instrument response of the setup is shown in Fig. 3.2. It consists of a main pulse and pre- and after-peaks at integer multiples of the dye laser round trip time of 12.3 ns. We achieve a suppression of pre- and afterpeaks compared to the main pulse of $1:250$. The time resolution is 52 ± 3 ps FWHM, measured using scattered red light from the dye laser. The resolution is determined by the transit time spread of the micro channel plate detector, which is specified to be 24 ps, by the jitter of the discriminator due to fluctuations in the detector signal, and by noise of the multi channel analyzer since the gain setting of the TAC is relatively low. The dye laser generates pulses of sub-picosecond duration, and the jitter in the electronics is negligible: we have observed that the correlation between two photodiodes is only ~ 3 ps wide.

To determine the effect of excitation intensity, a variable intensity filter was

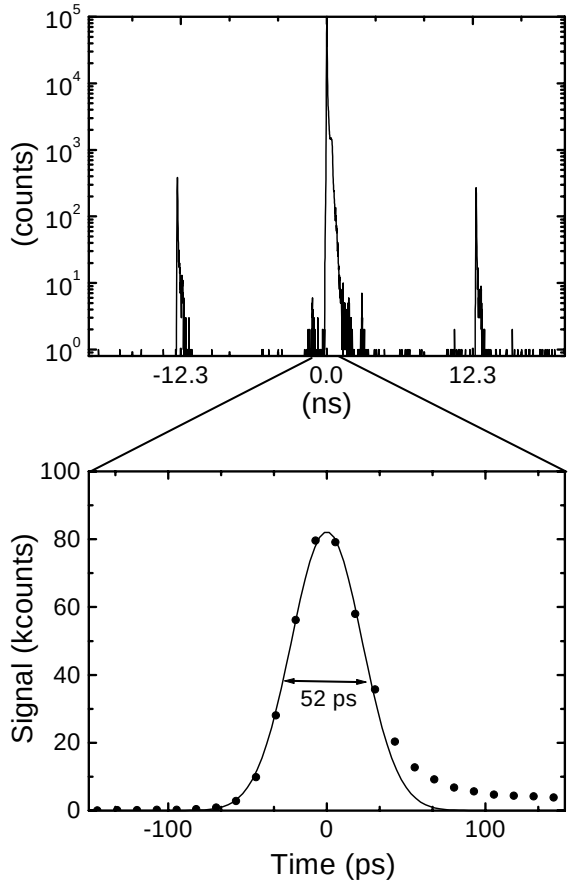

Figure 3.2 *Instrument response (time-resolved scattered red light from the dye laser), showing the main peak accompanied by pre- and after-peaks corresponding to the round trip time in the dye laser (above), and the full width at half maximum (enlargement, below).*

placed in front of the second harmonic generating crystal. Due to the frequency doubling process the intensity varied quadratically with variation of the attenuation. In order to measure the relative intensity of the excitation pulse a power meter was placed immediately behind the sample in the impinging beam. For the depolarization measurements we placed 10 mm polarizing prisms in the excitation beam and in front of the detector to select polarizations parallel and perpendicular to the incoming beam. For spectrally resolved measurements we employed a Carl Leiss prism monochromator, calibrated using the spectral lines of a neon lamp. The resolving power of the spectrometer is about 15 nm with the 1 mm slit widths used.

3.3 Results

Absorption and emission spectra of a suspension of the F4 spheres are shown in Fig. 3.3. The spectra are slightly asymmetric. This is a usual phenomenon in absorption and emission of FITC, both in solution and when bound to proteins.[17,18] No evidence is found for a FITC dimer absorption peak.[19] The spectra provide an excellent example of the Franck-Condon principle[17]: the emission spectrum is nearly a mirror image of the absorption. Both the absorption and the emission maximum shift to longer wavelengths as the particles' dye content is increased. The shift is 10 nm in going from the lowest to the highest dye concentration; it is fully completed already at a dye concentration of 6 mM. The Stokes shift, the difference between absorption and emission maxima, is constant at 40 nm.

The mechanism that causes the concentration dependent shift in the absorption and fluorescence spectra reveals itself in the time dependence of the fluorescence. If the shift is the result of self-quenching due to interactions between close pairs of dye molecules, then it should be accompanied by a reduction of the fluorescence lifetimes. A high probability of energy transfer between dye molecules reduces the time that molecules remain in their excited state. In contrast, if quenching were only due to formation of nonfluorescent dimers then no change in lifetime would be expected since these dimers do not contribute to the signal. To discriminate between these two situations, we have performed time-resolved fluorescence

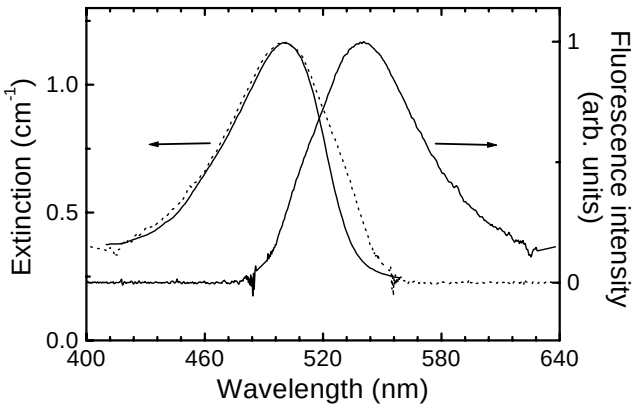

Figure 3.3 *Absorption and emission spectra (solid curves) of FITC-labeled silica spheres (designation F4) suspended in DMF. The absorption spectrum is nearly a mirror image of the fluorescence (indicated by the dotted curve). The mirror wavelength is* 520 *nm. The nonzero baseline is due to extinction from scattering.*

measurements.

Time-resolved total (*i.e.* spectrally integrated) fluorescence curves are shown in Fig. 3.4. At long times t the slope of the time-resolved fluorescence curves agrees with a lifetime of 3.8 ns expected for a free FITC molecule.[2] This long-time component probably corresponds to single FITC molecules in silica. With increasing dye concentration a fast component becomes more pronounced. In order to have a measure of the fluorescence lifetime, we determined the mean decay time $\langle\tau\rangle$ (*i.e.* the first moment) from the curves. We have plotted this mean lifetime in Fig. 3.5. It becomes rapidly smaller at higher dye contents, indicating the appearance of faster relaxation pathways. The change in time-dependence reveals that the concentration effect is caused by self-quenching of closely spaced molecules, as opposed to the formation of nonfluorescent dimers.

We can estimate the rate of energy transfer $n_{\mathrm{D}\to\mathrm{A}}$ between donor and acceptor molecules using the following expression due to Förster[20]:

$$n_{\mathrm{D}\to\mathrm{A}} = \frac{1}{\tau_0}\left(\frac{R_0}{R}\right)^6. \tag{3.1}$$

Here τ_0 is the reciprocal of the rate constant for spontaneous emission of the donor,

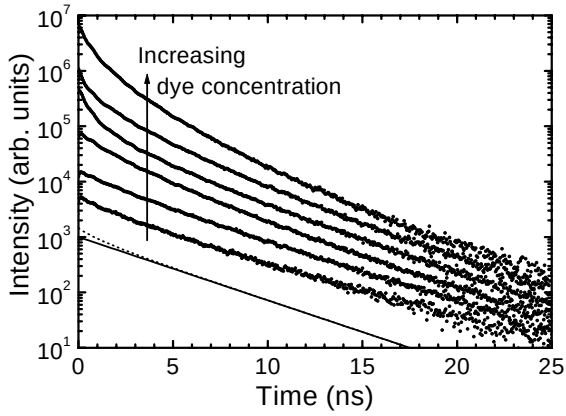

Figure 3.4 *Time-resolved fluorescence of various concentrations of FITC dye inside colloidal silica spheres. The curves have been offset for clarity. The dye concentration in the spheres increases from bottom to top. The straight line indicates a single exponential with a lifetime of* 3.8 *ns. The dotted curve corresponds to Eq. 3.3 with maximum curvature. Clearly the curvature is insufficient to account for the data.*

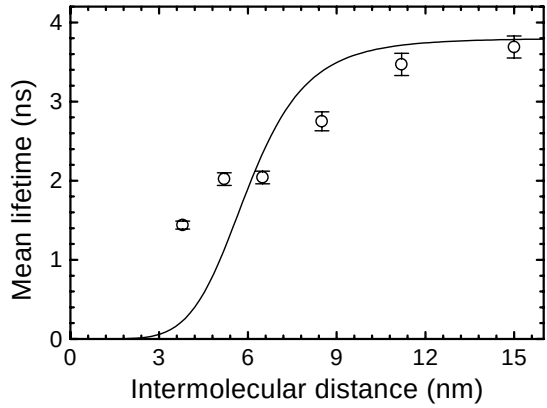

Figure 3.5 *Mean fluorescence lifetime as a function of the average intermolecular distance of FITC molecules in the spheres. The lifetimes were obtained from the experimental data in Fig. 3.4. The curve is an energy transfer model with a critical Förster distance of* 6.0 *nm and a lifetime of* 3.8 *ns.*

R is the distance between donor and acceptor and R_0 is the critical Förster distance – the distance at which half of the donors is deactivated by resonant energy transfer to an acceptor, which is about 5.0 nm for fluorescein.[17] For the average distance between dye molecules in the particles, we used $R = c^{-1/3}$, where c is the number of molecules per unit volume. This distance is on the order of the critical Förster distance for energy transfer in the more heavily doped samples, therefore quenching effects are to be expected. Adding rate constants, we find that the dependence of the mean lifetime $\langle\tau\rangle$ on the intermolecular distance is given by $1/\langle\tau\rangle = 1/\tau_0 + n_{\mathrm{D}\to\mathrm{A}}$. A reasonable fit is obtained for $\tau_0 = 3.8$ ns and $R_0 = 6.0$ nm, as shown in Fig. 3.5.

We have separately measured the fluorescence polarized parallel and perpendicular to the polarization of the light that excites the dye. The measured parallel and perpendicular components showed no detectable difference in time dependence, so the method did not allow observation of depolarization due to energy transfer. If there is energy transfer between molecules then one expects a decrease in fluorescence polarization with increased dye concentration. When a molecule is excited in a certain polarization direction it will preferentially emit with this same polarization. However, when the excitation is transferred to acceptors with a different orientation than the donor molecule, then the fluorescence becomes depolarized. Therefore, the difference in time dependence between fluorescence detected parallel or perpendicular to the polarization direction of the excitation beam would in principle provide information on the energy transfer process.

We can exclude Mie resonances and cooperative effects between spheres due to scattering[5] as a reason for the departure from single-exponential decay in Fig 3.4. In our case the refractive index difference between the spheres and the suspension liquid was much too small. As an extra test we measured the decay curves of spheres suspended in water, where the index difference is much larger. Although care had to be taken to prevent excessive leaching of the dye due to hydrolysis of the outer layers of the silica spheres, it was found that the decay was the same.

3.4 Quenching models

We have attempted to describe the fluorescence decay curves by three different models: quenching of excitations at the sphere's surface, a fractal distribution of dye molecules, and mutual annihilation of excitations.

In the first model, the excitations migrate diffusively through the sphere but are completely quenched when they reach the surface. Assuming an initially homogeneous density $u(r,t)$ of excited molecules, the decay is described by the diffusion equation

$$\frac{\partial u}{\partial t} = -\frac{u}{\tau_0} + D\nabla^2 u = -\frac{u}{\tau_0} + D\left(\frac{\partial^2}{\partial r^2} + \frac{2}{r}\frac{\partial}{\partial r}\right)u \tag{3.2}$$

with boundary conditions $u(R_S,t) = 0$ and $u(r,0) = u_0$. Here, $D = n_{\mathrm{D}\to\mathrm{A}}R_0^2/6$ is the effective diffusion coefficient, and R_S is the radius of the sphere. The solution of Eq. 3.2 is integrated over the sphere's volume to obtain the total fluorescence:

$$I(t) = u_0\frac{6}{\pi^2}\sum_{n=1}^{\infty}\frac{1}{n^2}\exp(-t/\tau_0 - n^2\pi^2 Dt/R_S^2) \tag{3.3}$$

Only the lower eigenmodes of the diffusion equation contribute appreciably. The formula clearly shows the competition between the spontaneous emission and the quenching at the surface. Unfortunately, Eq. 3.3 does not describe the data in Fig. 3.4 very well, as is illustrated by the dotted curve in the figure. The curvature of the line has been set to the extreme by adjusting the diffusion and emission timescales. Even so the curvature is insufficient to describe the experimental results, in particular at high dye concentrations. Also, the probability of an excitation reaching the sphere's surface is very small: according to the energy transfer rates $n_{\mathrm{D}\to\mathrm{A}}$ calculated before, the excitations in the most heavily doped sample can migrate an average of only 5.5 steps of $R_0 \sim 5$ nm before it decays radiatively. The traversed distance is much smaller than the size of the spheres: the radiative rate in the leading order term in Eq. 3.3 is three orders of magnitude larger than the surface quenching rate. This separation is even larger for the other samples. We conclude, therefore, that surface quenching does not play an important role in the quenching process.

Secondly, we tried to fit the time-resolved fluorescence curves to a model of Klafter and Blumen[21,22] describing the decay of an excited donor in the presence of acceptors which are randomly distributed on a fractal of Hausdorff dimension d:

$$I(t) = I_0 \exp(-t/\tau_0 - P(t/\tau_0)^{d/s}), \tag{3.4}$$

with s the order of the molecular interaction ($s = 6$ for the usual Förster dipole-dipole mechanism) and P a fitting constant which should be proportional to the acceptor concentration. For integral dimensions Eq. 3.4 reduces to familiar results of Förster.[23] The data of Fig. 3.4 could be fitted very well with Eq. 3.4, but the fit resulted in low values of d, between 0.3 and 1.5. Such low values for d are unrealistic; usually d is roughly between 1.5 and 3.[21,22,24]

A third model is to assume quenching by annihilation of excitations (singlet-singlet annihilation). In a system where rapid migration homogenizes the density of the excitations the corresponding rate equation is[25]

$$\frac{du}{dt} = -\frac{u}{\tau_0} - \kappa u^2, \tag{3.5}$$

where κ is the rate constant of the second order process. Solving this equation results in

$$\frac{1}{u(t)} = (\kappa\tau_0 + \frac{1}{u_0}) \exp(t/\tau_0) - \kappa\tau_0. \tag{3.6}$$

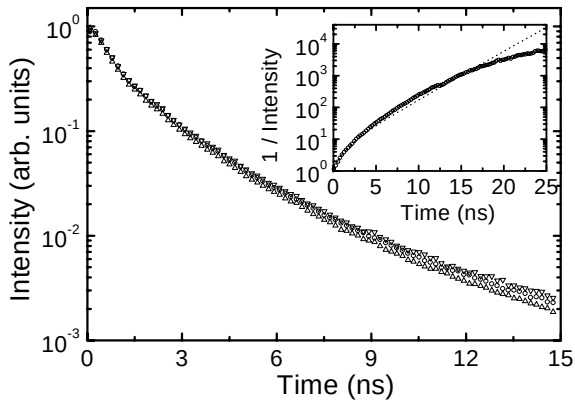

Figure 3.6 *Time-resolved fluorescence curves of the sample with the highest dye content (*31 *mM, F6, up triangle), and the influence of lowering the excitation power by a factor of* 2 *(*○*) and* 6 *(*▽*). The inset shows a fit of the excitation annihilation model Eq. 3.5 to these data.*

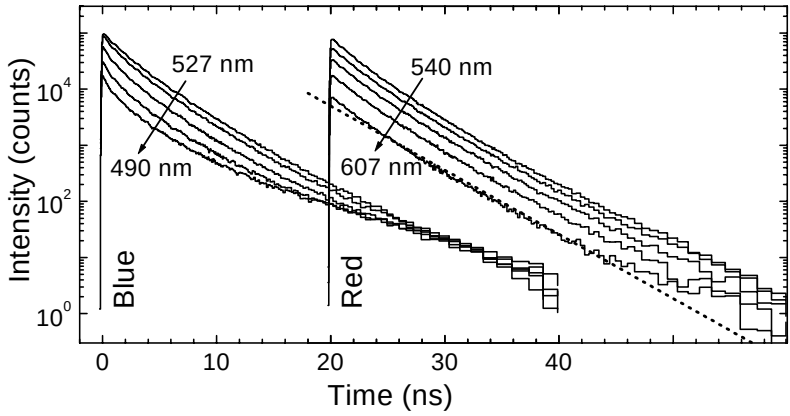

Figure 3.7 *Time-resolved emission of* 2.7 *mM dye inside colloidal silica spheres (with designation F3), spectrally resolved on the blue side (left) and red side (shifted right) of the dye's emission maximum. Clearly the influence of the energy transfer process is most pronounced at the blue side of the spectrum. The vertical distance between the curves reflects the shape of the emission spectrum,* i.e. *the curves have not been offset, in order to show the relative importance of the various spectral contributions to the total fluorescence. The straight line (dotted) corresponds to a single exponential with a lifetime of* 3.8 *ns.*

If we fit this to our measurements on the most heavily doped sample (Fig. 3.6, inset), we obtain a reasonable fit for $1/\tau_0 = 0.29$ ns^{-1} and $\kappa = 2.3 \pm 0.3$ ns^{-1}. Thus, the coefficient of the second order process is an order of magnitude greater than that of the first order process. If this model describes the situation well then the shape of the decay curve should depend strongly on the initial excitation density u_0. If u_0 is lowered then the probability that two excitations meet is lowered and the decay curve should look more like a single-exponential process. We verified this by decreasing the excitation intensity by a factor of 2 and 6, respectively. The resulting decay curves in Fig. 3.6, however, did not change at all, making singlet-singlet annihilation an unlikely explanation. Alternatively, intensity-independent decay can sometimes be produced by singlet-triplet annihilation. Since triplet states are efficient quenchers and long-lived (longer than our pulse separation) they could build up from pulse to pulse until a steady state is reached.[26] However, the intensity in our experiments was far too low to create enough triplets for such a process: We have at most 2×10^7 photons/pulse, whereas the number of spheres in the beam is $\sim 10^7$. Thus, there cannot be more than a few excitations per particle of which only a small fraction (1/1000th) are triplets.

Thus, none of these quite diverse quenching models explain the data very well. Since all the models assume a homogeneous distribution of FITC molecules this could be an indication that the distribution is not homogeneous. Possibly the dye molecules have a tendency to be incorporated into the spheres in clusters where there is rapid energy transfer.

To investigate the clustering of dye molecules inside the silica, we have measured time-resolved fluorescence at various wavelengths in the dye's emission spectrum, motivated by the concentration dependent shift of the emission spectra. This shift suggests that the clusters have different emission wavelengths than isolated dye molecules. If the time dependence of fluorescence from the clusters also differs from that of the isolated molecules, then the time dependence of the fluorescence will vary with wavelength. This would give an indication of the origin of the shape of the time-resolved fluorescence curves in Fig. 3.4. Time-resolved fluorescence curves of the F3 silica spheres are shown in Fig. 3.7. At the long wavelength side of the emission, the fluorescence curves are all very similar. In contrast, on the short wavelength side the curves start to bend: the initial decay is much faster (almost a factor of two) and a significant long time tail develops, even though the dye concentration inside the silica is only moderately high, 2.7 mM. The substantial bending of the fluorescence curves changes the emission spectrum only slightly because the tail does not contribute much to the total fluorescence yield. The bending occurs precisely at the side of the emission spectrum which overlaps most with the absorption band, see Fig. 3.3. The rate of nonradiative transfer, or equivalently the transfer distance R_0, increases with this overlap, resulting in steeper curves at short wavelengths in Fig. 3.7. To clarify the origin of the long time part of these curves, we have examined the data in Fig. 3.7 from a different perspective. In Fig. 3.8 we have plotted spectra at different instants after excitation. Initially the spectra shift to the red as time passes, but later on a sizeable blue component becomes visible.[27] The initial redshift can be explained by the enhanced nonradiative transfer due to spectral overlap of the absorption and emission bands. The observed blue component could be due to fluorescence from clusters of dye molecules. However it is not clear how the appearance of a blue component due to clustering can be reconciled with the observed redshift of the emission spectrum with increasing dye concentration.

3.5 Conclusions

We have studied the influence of the number density of dye molecules on the spectroscopic properties of fluorescein isothiocyanate (FITC) dye that is incorporated inside colloidal silica spheres. A redshift of 10 nm occurred in the absorption and

fluorescence spectra on traversing the concentration range 0.5 to 5 mM (inside silica). Simultaneously, the fluorescence lifetimes of the dye were strongly reduced, pointing to energy transfer taking place between dye molecules. The fluorescence decay curves could not be described satisfactorily with models involving second-order processes, or surface quenching, or a fractal distribution of dye molecules. A possible explanation is that the FITC molecules are not distributed homogeneously, but form clusters with intermolecular distances of less than the Förster distance. Such cluster formation would explain why quenching effects are observed already at low dye concentrations, and it is in agreement with spectrally resolved fluorescence decay measurements.

These findings have consequences for the use of dye-labeled silica particles with various experimental techniques. In the study of multiple scattering and photonic band structure effects, energy transfer effects within the spheres are intolerable so low dye concentrations are essential. Our results indicate that dye concentrations should not be higher than 1 mM. We have specially prepared silica spheres doped with a suitably low dye content to study photonic effects. The synthesis of these colloids is described in the next chapter.

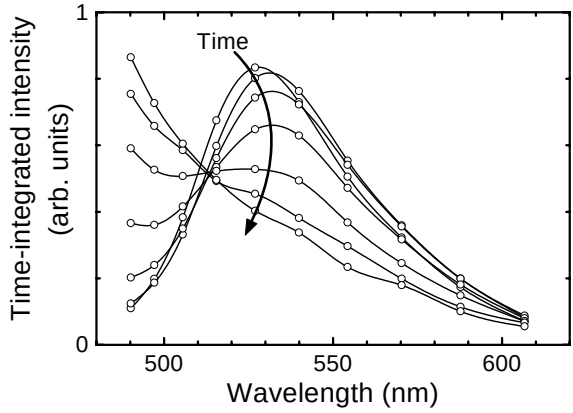

Figure 3.8 *Emission spectra of the F3 silica spheres, at different instants after excitation. The data have been obtained by integrating the curves in Fig. 3.7 over successive* 6 *ns long intervals. The spectra have been normalized to the area observable in the plot.*[27] *The curves are splines, serving as guides to the eye.*

References

1. E. Yablonovitch, 'Inhibited spontaneous emission in solid-state physics and electronics', *Phys. Rev. Lett.* **58**, 2059-2062 (1987).
2. R. P. Haugland and K. D. Larison (Eds.), *Handbook of fluorescent probes and research chemicals* (Molecular Probes Inc., 1996).
3. J. Martorell and N. M. Lawandy, 'Observation of inhibited spontaneous emission in a periodic dielectric structure', *Phys. Rev. Lett.* **65**, 1877-1880 (1990).
4. P. K. John, Y.-t. Zhu, Y. S. Liu, S. K. Wong, and W. R. Ware, 'Fluorescence lifetime measurements in monodispersed suspensions of polystyrene spheres', *J. Opt. Soc. Am. B* **10**, 356-359 (1993);
   N. M. Lawandy, 'Fluorescence-lifetime measurements in monodispersed suspensions of polystyrene particles: comment', *J. Opt. Soc. Am. B* **10**, 2144-2146 (1993).
5. M. Tomita, K. Ohosumi, and H. Ikari, 'Enhancement of molecular interactions in strongly scattering dielectric composite optical media', *Phys. Rev. B* **50**, 10369-10372 (1994).
6. A. van Blaaderen and A. Vrij, 'Synthesis and characterization of colloidal dispersions of fluorescent, monodisperse silica spheres', *Langmuir* **8**, 2921-2931 (1992).
7. D. Avnir, V. R. Kaufman, and R. Reisfeld, 'Organic fluorescent dyes trapped in silica and silica-titania thin films by the sol-gel method. Photophysical, film and cage properties', *J. Non-Cryst. Solids* **74**, 395-406 (1985);
   J. M. McKiernan, S. A. Yamanaka, B. Dunn, and J. I. Zink, 'Spectroscopy and laser action of rhodamine 6G doped aluminosilicate xerogels', *J. Phys. Chem.* **94**, 5652-5654 (1990).
8. See *e.g.* E. L. Wehry, and L. B. Rogers, in: D. M. Hercules (Ed.), *Fluorescence and phosphorescence analysis* (Interscience: New York, 1966), pp. 81-149.
9. A. Imhof, A. van Blaaderen, G. Maret, J. Mellema, and J.K.G. Dhont, 'A comparison between the long-time self-diffusion and low shear viscosity of concentrated dispersions of charged colloidal silica spheres', *J. Chem. Phys.* **100**, 2170-2181 (1994).
10. A. van Blaaderen, A. Imhof, W. Hage, and A. Vrij, 'Three-dimensional imaging of submicrometer colloidal particles in concentrated suspensions using confocal scanning laser microscopy', *Langmuir* **8**, 1514-1517 (1992);
    A. van Blaaderen and P. Wiltzius, 'Real-space structure of colloidal hard-sphere glasses', *Science* **270**, 1177-1179 (1995).
11. N. A. M. Verhaegh and A. van Blaaderen, 'Dispersions of rhodamine-labeled silica spheres: synthesis, characterization, and fluorescence confocal scanning laser microscopy', *Langmuir* **10**, 1427-1438 (1994).

12. R. M. Young, J. K. Arnette, D. A. Roess, and B. G. Barisas, 'Quantitation of fluorescence energy transfer between cell surface proteins via fluorescence donor photobleaching kinetics', *Biophys. J.* **67**, 881-888 (1994).
13. L. Song, E. J. Hennink, I. T. Young, and H. J. Tanke, 'Photobleaching kinetics of fluorescein in quantitative fluorescence microscopy', *Biophys. J.* **68**, 2588-2600 (1995).
14. W. Stöber, A. Fink, and E. Bohn, 'Controlled growth of monodisperse silica spheres in the micron size range', *J. Colloid Interface Sci.* **26**, 62-69 (1968).
15. A. Imhof, M. Megens, J J. Engelberts, D. T. N. de Lang, R. Sprik, and W. L. Vos, 'Spectroscopy of fluorescein (FITC) dyed colloidal silica spheres', *J. Phys. Chem. B* **103**, 1408-1415 (1999).
16. D. Bebelaar, 'Time response of various types of photomultipliers and its wavelength dependence in time-correlated single-photon counting with an ultimate resolution of 47 ps FWHM', *Rev. Sci. Instrum.* **57**, 1116-1125 (1986).
17. J. R. Lakowicz, *Principles of fluorescence spectroscopy* (Plenum Press: New York, 1983).
18. R. C. Nairn, *Fluorescent protein tracing*, 4th Ed., (Churchill Livingstone: Edinburgh, 1976).
19. *Dye lasers*, edited by F. P. Schäfer (Springer Verlag, Berlin, 1977).
20. Th. Förster, 'Transfer mechanisms of electronic excitation', *Discuss. Faraday Soc.* **27**, 7-17 (1959).
21. J. Klafter and A. Blumen, 'Fractal behavior in trapping and reaction', *J. Chem. Phys.* **80**, 875-877 (1984).
22. P. Levitz, J. M. Drake, and J. Klafter, 'Critical evaluation of the application of direct energy transfer in probing the morphology of porous solids', *J. Chem. Phys.* **89**, 5224-5236 (1988).
23. Th. Förster, 'Zwischenmolekulare Energiewanderung und Fluoreszenz', *Ann. Phys., Leipzig* **2**, 55-75 (1948).
24. K. Nakashima, J. Duhamel, and M. A. Winnik, 'Photophysical processes on a latex surface: electronic energy transfer from rhodamine dyes to malachite green', *J. Phys. Chem.* **97**, 10702-10707 (1993).
25. R. M. Noyes 'Effects of diffusion rates on chemical kinetics', in *Progress in reaction kinetics I* (Pergamon, Oxford, 1961).
26. S. L. Shapiro, *Ultrashort light pulses: picosecond techniques and applications*, 2nd Ed. (Springer Verlag, Berlin, 1984), p. 343.
27. As a consequence of the normalization, the blue component seems to grow. However one should realize that the blue component is decreasing in time; it only comes into view because the red components decay faster.

4
Growth of crystals from dye-doped colloids

4.1 Introduction

To meet the specific needs of experiments on fluorescence in photonic crystals, we have synthesized dye-doped colloidal silica spheres. Most of the fluorescence experiments were performed using crystals prepared from these specially synthesized colloids. We will discuss the particle synthesis and the preparation of photonic crystals from the synthesized particles, but first we will turn to the rationale underlying the synthesis.

Experiments on fluorescence in photonic colloidal crystals make high demands upon the properties of the colloidal particles used to form the crystals. The size of the particles should be on the order of optical wavelengths, the typical length scale in photonic crystals. The particles should readily form large crystals, so one can obtain samples that are sufficiently large to do experiments on. This requires particles which all have the same size, *i.e.* a size polydispersity of less than 6%.[1–3] To make the crystals fluorescent, the crystals should contain fluorescent molecules with a high quantum efficiency, like fluorescent dye. The fluorescent properties of the dye molecules should be isolated as much as possible from the material properties of the crystals. The molecules should preferably reside inside the colloidal particles rather than on the surface or outside in the suspending liquid, to prevent unwanted chemical interactions of the dye with the liquid or with particle surfaces.[4] To prevent the fluorescent molecules from disturbing the photonic band structure, absorption of light should be avoided. Absorption impedes multiple scattering, which is essential for photonic band structure to develop. To reduce absorption, the density of fluorescent molecules should be kept low. A low dye concentration will also prevent nonradiative transfer between dye molecules. The density of fluorescent molecules in commercially available polystyrene or PMMA spheres is usually high, close to the quenching concentration, as they have been designed to maximize the fluorescence.

A bright fluorescence facilitates detection of small numbers of spheres, important for example in biological applications.[5] Due to the high dye density, commercially available dyed spheres are not suitable for our purposes, so we synthesized spheres ourselves. Silica was chosen because it is inert and methods exist to incorporate dye in silica spheres.[6] The synthesis was performed by J. E. G. J. Wijnhoven in collaboration with the Van 't Hoff Laboratory, University of Utrecht.[6,7]

From the colloids, we prepared colloidal crystals by sedimentation. An important factor in the preparation of photonic crystals is the density of spheres, since it determines the position of the stop gaps in the photonic band structure. For our fluorescence experiments it is crucial that the stop gap overlaps with the dye's emission spectrum. Practical usefulness of photonic colloidal crystals depends on the availability of sufficiently large single crystals. Crystals with linear dimensions on the order of 10^4 unit cells (mm sizes) have been reported, albeit for dilute, weakly photonic samples with densities $\varphi < 1$ vol%.[8,9] The largest crystals are grown close to the freezing curve, where the nucleation rate is so small that few crystal grains nucleate and grow.[10] Dense crystals with $\varphi \sim 50$ vol% have been made with sterically stabilized colloids, but the crystallites are smaller with linear dimensions of $20 - 100$ μm.[12] We have grown charge stabilized single crystals with volume fractions up to 60 vol% and dimensions up to 0.5 mm (see Fig. 4.2, 7.1). The density of these crystals can be adjusted by adding salt to the suspending medium. The ionic strength of the liquid influences the extent of the double layer, *i.e.* the region of charge imbalance between the electrically charged surface of the spheres and the counter-ions in solution. In highly deionized suspensions, colloidal particles can carry an extended double layer of up to 500 nm thickness.[11,12] Adding salt to the suspension screens the Coulomb interaction and compresses the double layer. Spheres with an extended double layer will start to interact at larger separation, resulting in crystals with a lower volume fraction. From a photonic point of view, optimal volume fractions for crystals of silica spheres are in the range of 30–40%. Experiments in this intermediate density range are exceptional. Previously, interest in colloid physics has mainly focused on the one hand on hard sphere like colloids, with densities of about 50 vol%, and on the other hand on charge stabilized colloids with very low ionic strength and hence low densities, on the order of a few volume percent.[12,14] We have investigated the sedimentation and crystal formation in colloidal suspensions with intermediate volume fractions, highlighting the interplay between sedimentation and charge stabilization.

4.2 Synthesis

The synthesis of the silica spheres is a multi step process. In order to obtain spheres that are sufficiently monodisperse, the synthesis was started by forming silica seeds in a micro emulsion.[15,16] To obtain larger spheres, extra layers of silica were added using a Stöber-like synthesis method.[17] The core of the spheres is left blank; a micro emulsion based synthesis route for dyed spheres is not available. The first added layer of silica contains the dye. Further layers of blank silica serve to shield the dye from the outside.

The particles were nucleated in a micro emulsion following the method of Osseo-Asare and Arriagada.[15,16] Silica is formed inside micelles by hydrolysis and condensation of tetraethoxysilane (TES). The emulsion is prepared by mixing 500 ml of cyclohexane, 3.0 ml 25% ammonia and 26.6 ml surfactant (Igepal, polyoxyethylene (5) nonylphenyl ether) and stirring for half an hour at 300 rpm. The mixture must remain at 20°C otherwise the micro emulsion is not stable. An amount of 2.1 ml TES is slowly added below the surface of the emulsion and the emulsion is stirred vigorously for 15 minutes. The TES dissolves in the cyclohexane and after entering the micelles it reacts with the water. The reaction is catalyzed by the ammonia. After one week, the reaction is completed. The cyclohexane is evaporated and the spheres are resuspended in 500 ml ethanol.

Using a procedure described by Van Blaaderen *et al.*,[6] the nuclei were covered with a layer of silica in which the fluorescent dye, rhodamine isothiocyanate (RITC), is incorporated. The RITC dye was selected for its superior photostability and quantum efficiency compared to *e.g.* fluorescein isothiocyanate (FITC)[6]; quantum yields of 60–75% have been reported for RITC bound to proteins.[18] The silica is grown by adding extra TES and water. The dye is attached to the silica by a coupling agent, 3-aminopropyltriethoxysilane (APS). The dye is connected to the coupling agent by an addition reaction of the amine group of the APS with the isothiocyanate group of the RITC.[7] The ethoxysilane groups of the APS react with silica in a similar way as the TES.

An amount of 11 mg RITC dye is dissolved in 10 ml ethanol and stirred with an excess of APS for 12 hours. Of this solution, 0.79 ml is used in the first growth step. The silica particles from the micro emulsion are suspended in a mixture of 25% ammonia and distilled ethanol, in a 1000 : 80 volume ratio. A lower concentration of ammonia leads to undesired nucleation of new small particles; a higher concentration gives rise to coagulation, *i.e.* the formation of 'dumbbells'. The concentration TES should stay below 10 ml/l, therefore TES is added step by step, with at least 4 hours in between the steps. Per mol TES, 2 mol water should be added to compensate for the water consumed in the reaction. Finally, the spheres are centrifuged and resuspended in ethanol to remove the Igepal and the ammonia.

4.3 Results

Transmission electron microscopy pictures of the spheres after each step in the synthesis were taken to determine the sphere size. The micro emulsion yields spheres with a radius of 28 nm and a size variation of 2.5%. After adding the silica layer which contains the dye, the particles measured 58 nm in radius. Several batches of spheres with different final radii were made to ensure that we could match the stop band wavelength of the photonic crystals to the emission spectrum of the dye. The spheres are designated μESiJ1- followed by their radius, listed in table 4.1. Most of the fluorescence experiments have been performed using the spheres μESiJ1-101. A micrograph of the spheres is shown in Fig. 4.1, along with a sketch of the shell structure. The various silica shells have comparable densities, so the shells are invisible on the electron micrograph. The variation in the final size is only 1.5%. We also determined the outer radius of the spheres by static light scattering and dynamic light scattering. These radii, 121 nm and 122 nm respectively, are in excellent mutual agreement. The corresponding radius from electron microscopy is lower, 101 nm, but we have frequently encountered relatively low radii with this technique. In the following we will therefore consider the radius to be 121 nm with an accuracy of ± 1 nm.

An important aspect from the photonic perspective is the refractive index of

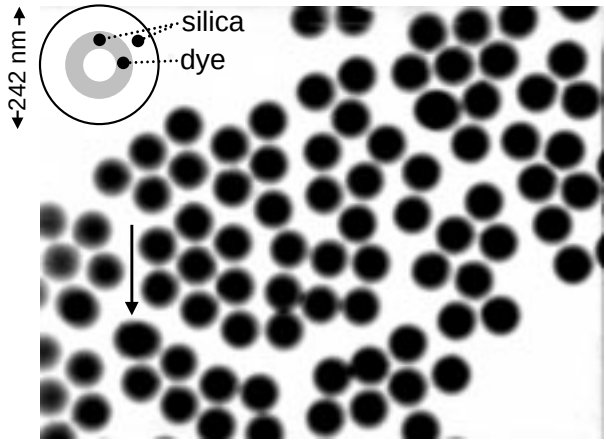

Figure 4.1 *Electron micrograph of the μESiJ1-101 silica spheres, together with a sketch of the shell structure, to scale. The micrograph also shows a small number of coagulated spheres ("dumbbells"), one of them is indicated by an arrow.*

the silica spheres. The refractive index of a batch of 60 nm radius silica spheres μESiJ4, similar to the μESiJ1 spheres except that they are not dye-doped, has been determined to be 1.466 ± 0.004 at 589 nm from transmission measurements in various ethanol-benzylalcohol mixtures.[20] The refractive index of various larger, dye-doped particles has been found to be 1.450 ± 0.001, by titrating dimethylformamide to a dispersion in glycerol until the transmission at 589 nm was maximized.[21] In the following we will consider the index of refraction of our μESiJ1 silica particles to be 1.45.

Each sphere contains about 200 rhodamine isothiocyanate dye molecules. The concentration of dye molecules in the colored silica layer is less than 0.5 mmol/l. This concentration corresponds to a distance between molecules of 15 nm, greatly in excess of the Förster transfer distance of 4 to 6 nm so there is no non-radiative transfer. Considering the molar decadic absorption coefficient of the dye, $\sim 4 \times 10^4$ l/(mol cm),[19] we calculate the inelastic length in a dense packing of spheres to be longer than 3 mm, so there is little absorption in our 0.3 mm thick samples. The dye molecules are covalently attached to the silica in the spheres and covered by a 45 nm thick layer of silica. This prevents washing out of dye by the suspending liquid: even after one year, the fluorescence from the suspending liquid corresponded to a dye concentration of less than 0.1 μmol/l. It is concluded that unwanted chemical interactions of the dye with the liquid and sphere surfaces are minimized.

4.4 Growth of the crystals

From the colloids, we prepared colloidal crystals by sedimentation. First, the colloids were deionized by successively centrifuging, decantating, redispersing, and diluting with freshly deionized water, followed by dialysis using ion exchange resin (BioRad AG501-X8, Hercules CA). The particles were then suspended in the de-

Table 4.1 *Size of the synthesized silica spheres, obtained from transmission electron microscopy (TEM), static light scattering (SLS), or dynamic light scattering (DLS)*

System	Radius (nm) TEM	SLS	DLS	Size variation(%) TEM
μESiJ1-74	74	88	92	1.5
μESiJ1-93	93	105	110	1.5
μESiJ1-101	101	121	122	1.5
μESiJ1-113	113	134	135	

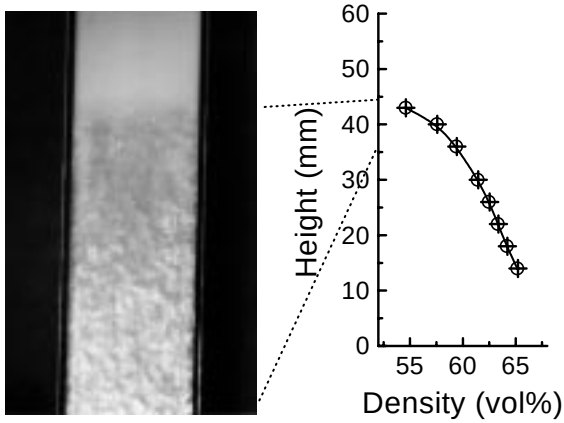

Figure 4.2 *Photograph of a photonic colloidal sample (#642bis) of sedimented silica spheres* µ*ESiJ1-101 (radii* 121 *nm; size polydispersity* 1.5%*) in water, contained in a* 3 *mm wide flat glass capillary, with the front face illuminated. The graph on the right shows the increase in density from top to bottom in the crystalline part of the colloidal sample. The density has been inferred from reflection (+) and transmission (◦) measurements. The curve is a guide to the eye.*

sired liquid (water, methanol, ethanol or dimethylformamide). The initial densities of the suspensions were estimated assuming that a centrifuged residue has a density of ~ 50 vol%. We prepared aqueous suspensions with various ionic strengths by adding NaCl. The suspensions were sealed in glass capillaries. For this purpose we employed flat capillaries with a 0.3 or 0.4 mm inside path length and 0.3 mm thick walls (Vitro Dynamics, Rockaway NJ). For x-ray scattering experiments on dilute suspensions we also used 2 mm diameter round Mark glass capillaries with 0.01 mm thin walls (Hilgenberg, Berlin).[22] By sedimentation under gravity, the colloidal suspensions form highly ordered fcc crystals, as revealed by our synchrotron small-angle x-ray diffraction studies.

A photograph of a flat capillary filled with a suspension of spheres is shown in Fig. 4.2. Next to the photo we have plotted the sample's density profile, inferred from reflection and transmission measurements. The density of spheres increases from top to bottom. In the upper part of the sediment, the spheres form a colloidal liquid. Light is randomly multiply scattered in this part of the sample, so the sample looks opaque white here. Lower in the sample the density of spheres is sufficiently high for the spheres to crystallize into regular arrays of various sizes which show colored Bragg reflections.

The crystallization proceeds from the bottom of the capillary upwards as the

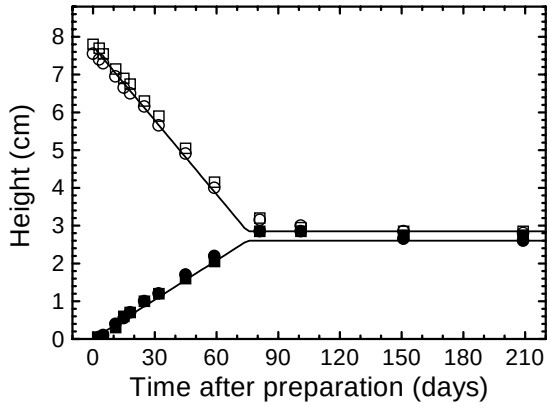

Figure 4.3 *Evolution of the height of the sediment in two capillaries (sample #627, circles, and sample #628, squares, respectively) filled with a* 13 *vol% aqueous suspension of* µ*ESiJ1-101 silica spheres. Open symbols correspond to the interface between clear liquid and the colloidal suspension, solid symbols to the top of the crystalline part of the sediment. The straight lines are guides to the eye. The ionic strength of the suspending liquid is* 0.25 *mM.*

initially homogeneous suspension settles and the density at the bottom increases.[23] We have carefully kept track of the interface between the clear liquid on top and the opaque colloidal suspension underneath, and of the interface between the suspension in the middle and the colloidal crystals below. The advancement of the interfaces during sedimentation is shown in Fig. 4.3. Initially, the heights vary linearly with time. The suspension settles, forming a crystalline sediment at the bottom of the capillary. The crystal formation starts immediately, indicating that the spheres crystallize at the suspension-crystal interface and not in the suspension itself. The sedimentation and crystal growth go on until there is about 2 mm of opaque white suspension left. The heights then remain constant, apart from a slight compactification of the crystalline part during the next one or two months. The shrinkage depends on the amount of added salt. The shrinkage varies from $\sim 0\%$ for a salt concentration of 1.0 mM to 20% for a salt concentration of 0.25 mM. Presumably the glass capillaries slowly release extra ions which screen the electrostatic repulsion between the spheres.

The crystal growth is governed by the ratio of the sedimentation velocity to the diffusion velocity, known as the Péclet number.[13] If the diffusion is faster than the sedimentation then the spheres have time to find a lattice position before the next spheres arrive. The initial velocity of the suspensions is determined by gravity, bal-

anced by friction in the liquid, *i.e.* by the difference in mass density $\Delta\rho$ between particles and suspending liquid and by the viscosity η of the liquid. The settling velocity for a single sphere of radius R in a large volume of liquid, the Stokes velocity,[13] is

$$v_0 = \frac{2}{9}\frac{\Delta\rho g}{\eta}R^2, \tag{4.1}$$

where $g = 9.8$ m/s^2 is the gravitational constant and we have taken $\Delta\rho = 1.0$ g/cm^2. In more dense suspensions the sedimentation is slower because the spheres hinder each other. It has been found previously that the reduction in velocity can be adequately represented by the formula[13,24]

$$v = v_0(1 - \frac{\varphi}{p})^{kp}, \tag{4.2}$$

where φ is the volume fraction of spheres in the liquid; the parameter k determines the lowest order correction to the velocity, $v = v_0(1 - k\varphi + \ldots)$, and p corresponds to the density where sedimentation stops.[24] According to theoretical considerations regarding the dilute limit, k should be set equal to 6.55. We have set $p = 54\%$ corresponding to hard spheres.[25] We have determined the velocity of the transparent-opaque interface for colloidal suspensions of μESiJ1 spheres with various sizes and two different volume fractions. We observe that the velocity varies quadratically with sphere size as predicted by Eq. 4.1. The density dependence agrees well with Eq. 4.2. For the suspensions of spheres of 134 nm radius with ionic strength of 1 mM, we observed a velocity in the dilute limit v_0 of 2.6 ± 0.4 mm/day, reasonably close to the estimate based on Eq. 4.1 of 3.4 mm/day considering the modest ionic strength. The satisfactory agreement indicates that the spheres sediment individually, forming crystals at the bottom, rather than nucleating in the suspension which would result in a larger sedimentation velocity due to the comparatively large size of crystallites. From the Stokes velocity v_0 and the diffusion constant $D_0 = kT/(6\pi\eta R)$ we can estimate the Péclet number $v_0 R/D_0$. The Péclet number is on the order of 10^{-3} for our colloids, which suggests that the sediment is close to thermodynamic equilibrium. Indeed the initial volume fraction of the initial suspension is of little importance for the quality of the crystals which form. High densities yield equally beautiful crystals as low densities, evidenced by stop band widths measured in reflection (only the brightness of reflection tends to be slightly weaker). The main factor affecting the crystal quality is the size polydispersity of the spheres, and tranquillity during sedimentation. We have moved the samples to measure the sediment heights, and even these slight disturbances leave visible marks: at the corresponding heights new crystallites have started to grow. The pattern of the marks correlates exactly with the time intervals between height measurements.

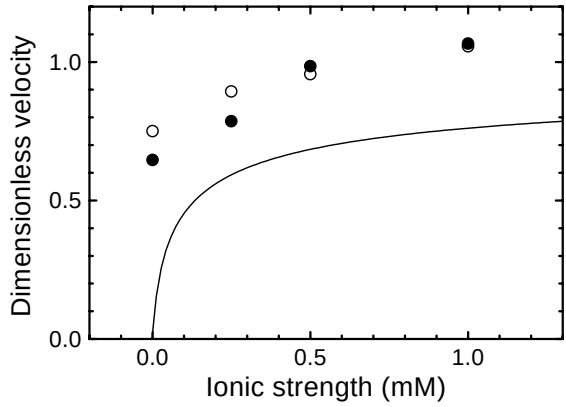

Figure 4.4 *Settling velocity for* 8 *(○) and* 13 *(•) vol% suspensions in water with various salt concentrations. The velocity has been scaled to the velocity v calculated for spheres with no double layer,* i.e. *the Stokes velocity Eq. 4.1 corrected for the density using Eq. 4.2. The estimated error in the measured velocities is* 0.03*. The settling velocities are derived from height curves of 64 samples among #605-#676. For comparison, the solid curve shows the inverse of the relative increase in volume fraction that would result if we added one Debye screening length* κ^{-1} *to the sphere radius,* i.e. $(1+\kappa R)^{-3}$*, for a sphere radius R of* 100 *nm.*

4.5 Density tuning

The density of spheres in the sediment is an important factor in the preparation of photonic crystals since it determines the position of the stop gaps in the photonic band structure. The volume fraction of the crystals can be tuned via the ionic strength of the suspending liquid. Adding salt to the suspension screens the Coulomb interaction and compresses the double layer. Spheres with an extended double layer will start to interact at larger separation, which results in crystals with lower volume fractions. The ionic strength of the liquid also plays an important part in the velocity of settling spheres. Due to the interaction the spheres will more easily hinder each other during sedimentation. As a consequence, one would expect that suspensions sediment slower at low ionic strength. To illustrate this influence of the ionic strength, we have plotted settling velocities in suspensions with various amounts of added salt in Fig. 4.4. The velocity in Fig. 4.4 is reduced at low ionic strength as we had anticipated. The decrease can amount to as much as 40%.

As the suspensions settle, the spheres form crystals at the bottom of the capillaries. The crystal growth velocity is determined by the influx of spheres from the suspension. Thus the settling and growth velocities are proportional at fixed initial

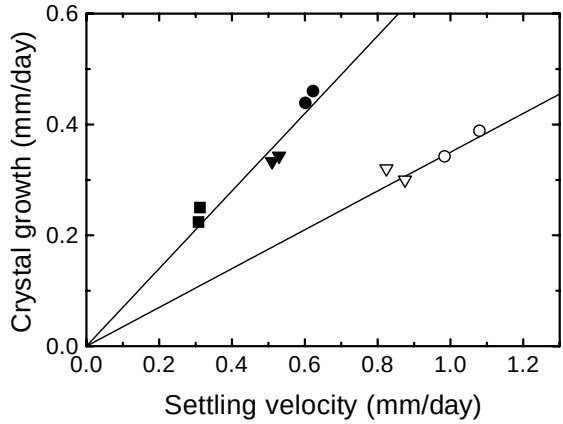

Figure 4.5 *Crystal growth velocity versus settling velocity of the suspension above the sediment for* 8 *and* 13 *vol% suspensions (open and closed symbols) of spheres of various sizes in water with* 0.25 *mM added salt. Circles, triangles, and squares pertain to spheres with radii of* 105, 121, *and* 134 *nm respectively.*

volume fraction, as can be seen in Fig. 4.5. From the settling and growth velocities and the suspension's initial density, we can readily estimate the average volume fraction of the crystalline part of the sediment. The resulting volume fractions are plotted in Fig. 4.6. The densities clearly increase with ionic strength, in a similar fashion as the settling velocities in Fig. 4.4.

To show this similarity more clearly, we have transformed the settling velocities to volume fractions using Eq. 4.2 and the Stokes velocity. We interpret the resulting 'effective' volume fraction as the volume fraction occupied by the spheres together with their double layers. In Fig. 4.6 we have plotted the ratio of the known initial density of spheres in the suspension to the effective density of spheres. Comparing this density ratio to the density of the crystals in the same figure, we see that the data are in excellent mutual agreement. Apparently the influence of added salt on the suspension's effective volume fraction is similar to the influence on the volume fraction of the crystals.

The density of the crystals can also be obtained from optical measurements and knowledge of the photonic band structure. We have determined stop gap frequencies from optical measurements of the (111) Bragg reflections. With our range of sphere sizes and ionic strengths we cover the wavelength range from 475 to 810 nm, which includes nearly the whole visible part of the spectrum. Volume fractions were obtained from the stop gap wavelength and the SLS sphere radii in table 4.1. In Fig. 4.7 we have plotted the volume fraction of the uppermost crystals in sam-

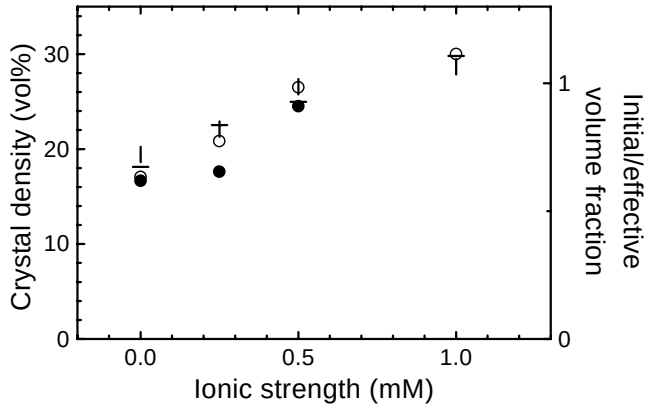

Figure 4.6 *Average density of the crystalline part of the sediment (circles, left axis) and the ratio of initial and effective volume fractions of the settling suspension (bars, right axis), for various amounts of added salt and initial suspension densities of* 8 *vol% (*∘*,–) and* 13 *vol% (*•*, |). The density of the crystals is obtained from the slopes in Fig. 4.5 and the initial density of the suspension; the effective volume fraction is based on Fig. 4.4.*

ples of various ionic strengths. The density at the bottom of the sample is generally ~ 10 vol% higher than at the top. The density in the figure is lower for low ionic strengths, *i.e.* when the charge of the spheres is screened less, in a similar fashion as the densities obtained from sedimentation, see Fig. 4.6.[26]

To compare the density changes with the screening lengths, we have plotted in Fig. 4.7 three curves corresponding to the volume fraction that would result if we add one Debye screening length to the sphere radius, *i.e.* $\varphi_0(1+1/\kappa R)^{-3}$, where φ_0 is the volume fraction with no double layer. The inverse screening length κ introduces the dependence on ionic strength I. For water at room temperature, $\kappa = 3.32\ \mathrm{nm}^{-1}\sqrt{I}$ if the ionic strength is expressed in mol/l.[13] The curves in Fig. 4.7 show a similar trend as the densities, both as a function of ionic strength and as a function of sphere size. The volume fraction at a specific ionic strength is higher for large spheres because the Debye screening length is smaller relative to the sphere size. When little salt is added, the density is higher than predicted by the curves, presumably due to extra ions released by the glass capillaries.

The results in Fig. 4.7 demonstrate that the volume fraction of the crystals can indeed be tuned by adjusting the ionic strength of the suspending liquid. The wavelength of the stop gap can be modified using the size of the spheres. By means of the ionic strength and the sphere size, we can overlap the stop gap and the dye's emis-

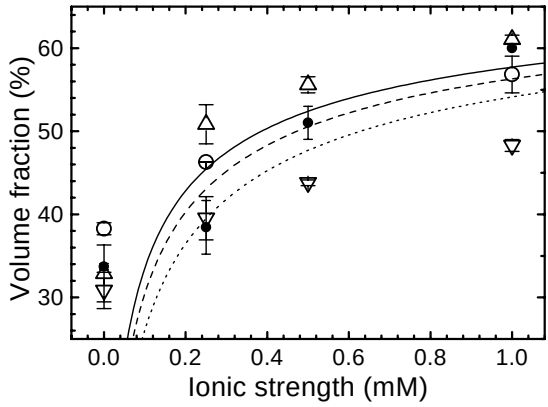

Figure 4.7 *Density of the topmost crystals determined from optical measurements of the (111) Bragg reflections on various samples (▽, ○, △: μESiJ1-93, 101, 113). The curves correspond to the volume fraction that would result if we added one Debye screening length κ^{-1} to the sphere radius R, starting from a fixed volume fraction with no double layer φ_0 (solid curve: $R = 134$, dashed curve: $R = 121$ nm; dotted curve: $R = 105$ nm). Densities from sedimentation (•, see Fig. 4.6) are shown for comparison. These densities have been multiplied by* 2 *to bring them in the same range.*[26]

sion spectrum, so we are well-equipped for experiments on fluorescence in photonic crystals.

References

1. E. Dickinson and R. Parker, 'Polydispersity and the fluid-crystalline phase transition', *J. Physique Lett.* **46**, L229-L232 (1985).
2. S. I. Henderson, T. C. Mortensen, S. M. Underwood, and W. van Megen, 'Effect of particle size distribution on crystallization and the glass transition of hard sphere colloids', *Physica A* **223**, 102-116 (1996).
3. D. A. Kofke and P. G. Bolhuis, 'Freezing of polydisperse hard spheres', *Phys. Rev. E* **59**, 618-622 (1999).
4. B. Y. Tong, P. K. John, Y.-t Zhu, Y. S. Liu, S K. Wong, and W. R. Ware, 'Fluorescence lifetime measurements in monodispersed suspensions of polystyrene spheres', *J. Opt. Soc. Am. B* **10**, 356-359 (1993).
5. R. P. Haugland, and K. D. Larison (Eds.), *Handbook of Fluorescent Probes and Research Chemicals* (Molecular Probes Inc., 1996).

6. N. A. M. Verhaegh and A. van Blaaderen, 'Dispersions of Rhodamine-labeled silica spheres: synthesis, characterization, and fluorescence confocal scanning laser microscopy', *Langmuir* **10**, 1427-1438 (1994).
7. A. van Blaaderen and A. Vrij, 'Synthesis and characterization of colloidal dispersions of fluorescent, monodisperse silica spheres', *Langmuir* **8**, 2921-2931 (1992).
8. T. Okubo, 'Giant colloidal single crystals of polystyrene and silica spheres in deionized suspension', *Langmuir* **10**, 1695-1702 (1994).
9. T. Palberg, W. Mönch, J. Schwarz, and P. Leiderer, 'Grain size control in polycrystalline colloidal solids', *J. Chem. Phys.* **102**, 5082-5087 (1995).
10. K. F. Kelton, in *Solid State Physics*edited by H. Ehrenreich and D. Turnbull (Academic, New York, 1991) p. 75;
M. J. P. Brugmans and W. L. Vos, 'Competition between vitrification and crystallization of methanol at high pressure', *J. Chem. Phys.* **103**, 2661-2669 (1995).
11. T. Okubo, 'Melting temperature of colloidal crystals of polystyrene spheres', *J. Chem. Phys.* **95**, 3690-3697 (1991).
12. P. N. Pusey, in *Liquids, freezing and glass transition*, edited by J. P. Hansen, D. Levesque, and J. Zinn-Justin (North-Holland, Amsterdam, 1991), pp. 763-942.
13. R. J. Hunter, *Foundations of colloid science* (Clarendon, Oxford, 1992).
14. A. P. Gast and W. B. Russel, 'Simple ordering in complex fluids', *Physics Today* **51**, 24-30 (1998).
15. F. J. Arriagada and K. Osseo-Asare, in *The colloid chemistry of silica*, edited by H. E. Bergna, (Am. Chem. Soc., Washington DC, 1994).
16. F. J. Arriagada and K. Osseo-Asare, 'Synthesis of nanosize silica in aerosol OT reverse microemulsions', *J. Colloid Interface Sci.* **170**, 8-17 (1995).
17. W. Stöber, A. Fink, and E. Bohn, 'Controlled growth of monodisperse silica spheres in the micron size range', *J. Colloid Interface Sci.* **26**, 62-69 (1968).
18. R. F. Chen, 'Fluorescent protein-dye conjugates', *Arch. Biochem. Biophys.* **133**, 263-276 (1969).
19. U. Brackmann, *Lambdachrome laser dyes* (Lambda Physik, Göttingen, 1994).
20. F. Poelwijk, 'Correlatiespectroscopie aan colloïdale suspensies', Verslag Eigen Werk 3 (Universiteit van Amsterdam, 1998).
21. A. Imhof, M. Megens, J J. Engelberts, D. T. N. de Lang, R. Sprik, and W. L. Vos, 'Spectroscopy of fluorescein (FITC) dyed colloidal silica spheres', *J. Phys. Chem. B* **103**, 1408-1415 (1999).
22. The samples are numbered #601 to #676, in order of decreasing sphere size. Each of the four sphere sizes is represented by four pairs of samples enumerated in order of increasing amount of added salt, for two or more volume fractions.
23. K. E. Davis, W. B. Russel, and W. J. Glantschnig, 'Settling suspensions of col-

loidal silica: observations and x-ray measurements', *J. Chem. Soc. Faraday Trans.* **87**, 414-424 (1991).
24. N. Ekdawi and R.J. Hunter, 'Sedimentation of disperse and coagulated suspensions at high particle concentrations', *Colloids and Surfaces* **15**, 147-159 (1985).
25. Note that the velocity is not very sensitive to the exact value of p for the volume fractions of our suspensions. The parameter p enters only in the second order term of the expansion in density of Eq. 4.2.
26. The densities from sedimentation and reflection differ by about a factor of 2. On the one hand, the densities obtained from reflection measurements are possibly too high; from the data in Fig. 4.7 we find $\varphi_0 \sim 70\%$. This is rather dense, considering that the volume fraction of melting for hard spheres is only 54%.[12] On the other hand, the densities from sedimentation are possibly somewhat low. The difference between sedimentation and reflection is probably due to a systematic error in the sphere radii (for the reflection measurements) or in the initial volume fractions of the suspensions (for sedimentation), which shows up as a common factor in the reflection or sedimentation densities.

5
Light sources inside photonic crystals

5.1 Introduction

A study of light sources inside photonic crystals is pertinent in view of the primary aim of photonic crystals, *i.e.* modifying the radiative properties of such sources. Among the radiative properties of light sources inside photonic crystals, the emission spectrum is most readily accessible experimentally. Emission spectra of internal sources have been measured, and clear stop gaps in emission spectra have been observed.[1–6] Apparently the photonic band structure strongly influences the emission spectrum. Important open questions remain, however. It appears that the observed stop gaps differ in several respects from the stop gaps encountered in conventional transmission spectra, *e.g.* the attenuation and the width of emission spectra are smaller than in transmission spectra. We will explain these observations with a simple model, outlined in Fig. 5.1. The essential ingredient is that the stop gaps do not cover all directions in the crystals, *i.e.* that light can propagate in directions outside the stop gaps. As a result, the spectrum from internal light sources includes light that is emitted in directions outside the stop gaps and subsequently scattered by defects close to the surface (Fig. 5.1a). In the presence of a photonic band gap, the scattered light is strongly attenuated because the stop gaps extend over 4π solid angle, trapping light in all directions (Fig. 5.1c). Thus the spectrum of sources inside photonic crystals reveals unambiguously whether a photonic band gap has been achieved.

5.2 Experiments

To experimentally realize light sources inside photonic crystals we used the dye-doped silica spheres μESiJ1-101 described in the previous chapter. The silica spheres (refractive index $n = 1.45$) are suspended in water ($n = 1.33$). The resulting colloidal suspensions are contained in long flat glass capillaries of 3 mm

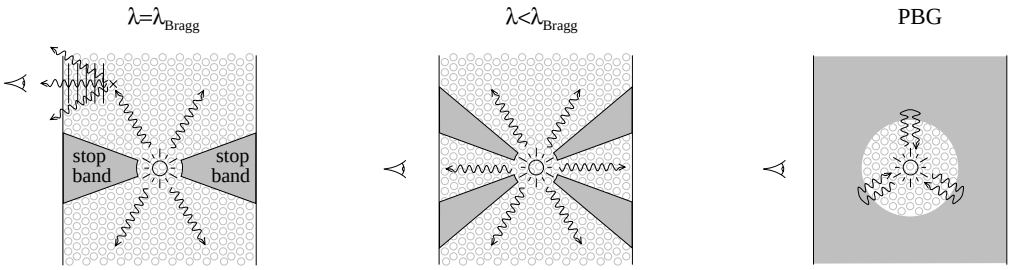

Figure 5.1 *Schematic drawing of the trajectory of light emitted by a point source inside a photonic crystal, (a) when the light is just Bragg reflected from the crystal planes indicated, (b) for Bragg reflection at shorter wavelength, when the reflection is inclined to the lattice planes, and (c) in a crystal with a photonic band gap. The cross in the leftmost panel indicates a defect.*

width and 0.3 mm internal path length. The samples form large highly ordered fcc crystals with the (111) planes parallel to the walls of the capillaries, as revealed by our synchrotron small-angle x-ray diffraction studies. The spacing of the crystal planes varies with height in the sample due to gravity. The spacing ranges from 206 to 221 nm, which corresponds to a density range of 53–65 vol%. Higher up in the samples, the less dense colloidal liquid phase coexists. The freezing density is close to the freezing density of hard spheres of 54 vol%, consistent with the screened Coulomb interactions that occur in these systems. In our samples, 0.5 mM NaCl was added to screen the charge on the spheres.

Fluorescence spectra were obtained by exciting the dye with an argon laser operating at a wavelength of 488 nm; the spectra were collected with a Carl-Leiss prism spectrometer, equipped with a photomultiplier. The spectrometer has a resolving power of 1 nm for the 0.1 mm slit settings used. It was calibrated using the spectral lines of a neon lamp. The samples were excited through the back surface, *i.e.* the side of the sample away from the detector. The detector is looking at the front surface. The capillaries were mounted on a rotation stage to orient the crystals with respect to the position of the detector. Optical transmission spectra were measured with a collimated halogen lamp. Spectra were taken directly or bye use of a cylindrical index matching bath filled with dimethylformamide, to suppress refraction at the surface of the sample capillary.

5.3 Results and Discussion

We have obtained fluorescence spectra of dye in many different photonic crystals. A typical example is shown in Fig. 5.2 and compared with the spectrum of dye in a colloidal liquid. The crystal changes the fluorescence spectrum of the dye considerably: the spectrum acquires a pronounced stop gap. The stop gap is caused by the (111) crystal planes. The crystal planes act as Bragg mirrors for the fluorescence, preventing part of the light from leaving the crystal. We observed that the central wavelength of the stop gap depends on the density of spheres in the crystal. By changing the vertical position in a sample, we can vary the density and hence tune the stop gap wavelength. As an example, we have carefully tuned the stop gap on the dye emission spectrum in Fig. 5.2.

To obtain the transmission spectrum of the light emitted inside the crystal, we have taken the ratio of the fluorescence spectrum to the reference fluorescence spectrum of dye in a colloidal liquid in Fig. 5.2. In what follows, we will call the resulting relative fluorescence spectrum the "transfer function". The transfer function has been normalized to 100% at long wavelengths; see Fig. 5.3. For comparison, we have also plotted a transmission spectrum of plane waves entering the crystal from outside. One can see that the stop gap in the transfer function has the same central wavelength of 580 nm as the stop gap in the conventional transmission spectrum. The stop gap in the transfer function, however, is narrower and the maximum attenuation of the transfer function is much less than that of the transmission of ex-

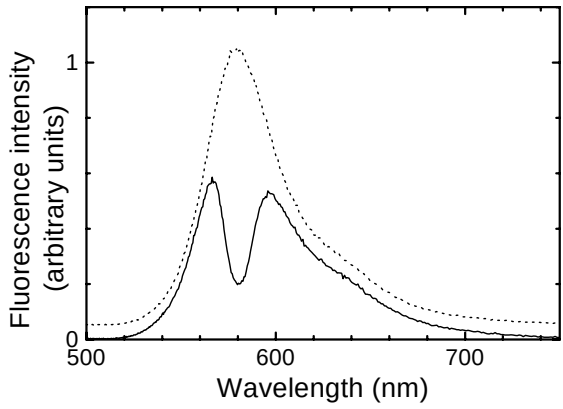

Figure 5.2 *Fluorescence spectrum of dye in a photonic colloidal crystal (solid curve) and in a colloidal liquid of spheres (dotted curve, offset by* 0.05*). Bragg reflection causes a stop gap in the spectrum of the crystal.*

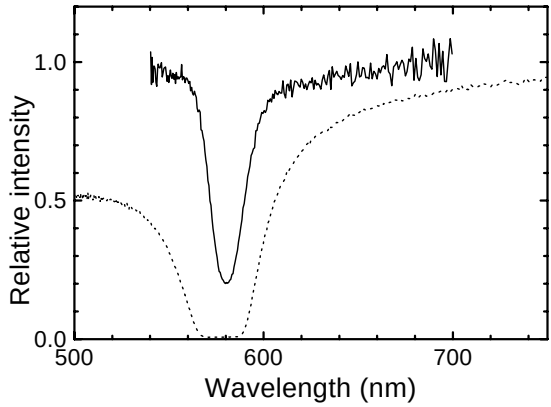

Figure 5.3 *Transfer function of a light source inside a crystal (solid curve, relative fluorescence intensity) and of a light source outside the crystal, far away (dotted curve, transmission of a plane wave). Both spectra were taken normal to the (111) crystal planes.*

ternal plane waves. We will now discuss the main features of the stop gaps in the transfer function.

We expect that the central wavelength of the stop gap is related to the lattice spacing of the crystal, the effective refractive index of the crystal, and the crystal's orientation.[7] Transfer functions for various emission directions are presented in Fig. 5.4. Stop gaps are observed for all emission directions; away from the normal, the central wavelength of the stop gap goes to shorter wavelengths, qualitatively resembling Bragg reflection. The central wavelength of the stop gap as a function of angle is shown is Fig. 5.5, for stop gaps in the transfer function as well as for stop gaps in transmission spectra. The two stop gaps follow the same curve. The shift of the central wavelength is very well explained using Bragg's law $2d\sin\theta = \lambda/n_{\text{eff}}$ generalized to include an effective refractive index n_{eff}, if allowance is made for refraction at the sample interface using Snel's law. In diffraction experiments using external sources we have previously found that the effective refractive index of a photonic crystal is well described with the Maxwell-Garnett approximation.[7,8] We note that Bragg's law with an effective Maxwell-Garnett refractive index yields results which closely correspond with dynamical diffraction theory.[9] For comparison, it is shown that the experimental data in Fig. 5.5 are clearly in between Bragg's law with refraction of either water or silica. Without index matching bath, we found that refraction at the air-capillary interface introduces large systematic errors. In a previous experiment, Yamasaki and Tsutsui presented stop gaps in the transfer

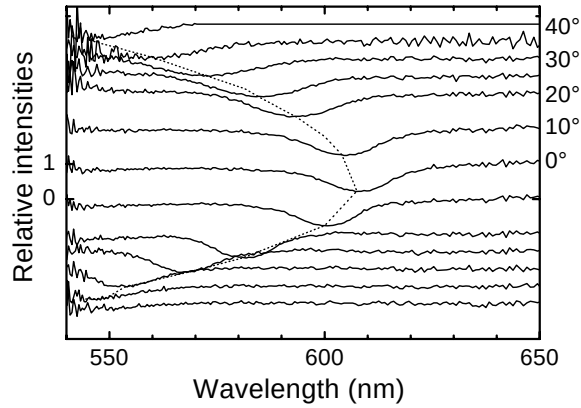

Figure 5.4 *Transfer function for sample rotations of* 0°–40° *in two directions. The spectra have been divided by a reference spectrum and normalized at long wavelength. For positive rotations the curves have been offset upward, for negative rotations downward. The stop gap shifts to shorter wavelengths if the crystal is rotated, in accordance with Bragg's law.*

function that differ both from stop gaps in transmission spectra, and from theoretical predictions.[3] It is unknown what the reasons for this surprising deviation are. The data in Fig. 5.4 illustrate that for emission wavelengths that are equal to the Bragg wavelength at normal incidence, light can still propagate in oblique directions (see Fig. 5.1a). For shorter emission wavelengths, the light is Bragg reflected at a certain angle, but can propagate in other directions, such as the normal one (see Fig. 5.1b). The resulting variations in fluorescence intensity are familiar from x-ray fluorescence, where they are referred to as Kossel lines. In x-ray fluorescence, the term Kossel line is reserved for light which originates inside a crystal. The variations in fluorescence that we have measured here correspond to true Kossel lines; the patterns of lines that occur in elastically scattered light are, strictly speaking, Seemann diagrams.[9]

The width of stop gaps in transmission is due mainly to photonic crystal effects, but also to disorder that occurs in any crystal.[10] The latter includes strain, finite crystal size,[9] crystal misorientations, and possibly even the lattice modes of the colloidal crystal.[11] For a real photonic crystal, the observed width is thus equal to or larger than the intrinsic photonic width. An intrinsic width between 11.1 and 11.7 nm is predicted by dynamical diffraction and band structure theories.[12,9] In Fig. 5.3, the stop gap in the transfer function is about 20 nm wide. The width of the stop gap in the transmission, however, is much larger. Apparently the course of

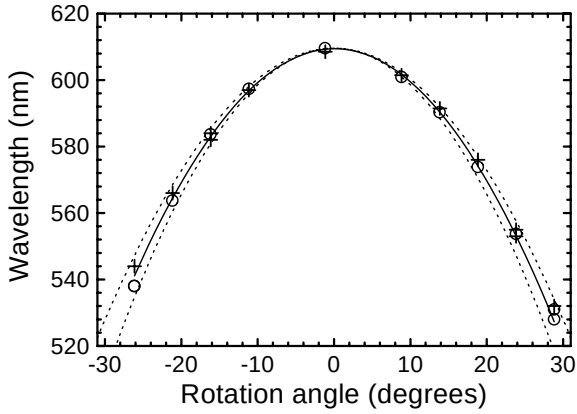

Figure 5.5 *Central wavelength of the stop gap in the transfer function (∘) and in transmission spectra (+) as a function of rotation of the sample. The wavelengths are based on spectra taken using an index matching bath. The solid curve corresponds to Bragg's law with correction for refraction at the sample interface, using an effective refractive index of* 1.39*. The dotted curves are based on the refractive index of silica (upper curve) and water (lower curve).*

plane waves through the sample is qualitatively different from that of light coming from inside.

In transmission experiments, the attenuation at the center of a stop gap is appreciable, even for small or imperfect crystals.[13,14] This is also the case in Fig. 5.3. It is striking that for the same crystal the transfer function shows much less attenuation. To elucidate the origin of this difference, we have varied the position of the light source inside the sample as follows (*cf.* inset of Fig. 5.6); The light which excites the dye is sent through the sample at a glancing angle of 30° with the surface. Thus the beam is close to the front surface and at one edge and close to the back surface at the other edge of the sample. By imaging a specific part of the sample on the detector, we select the depth of the emitting sources. The beam waist at the sample measures only 20 μm full width at half maximum, and the width of the imaged area is 50 μm, both much less than the 300 μm sample thickness. The resulting transfer functions are shown in Fig. 5.6. The outermost curves correspond to regions that are 400 μm apart on the sample. Remarkably, the attenuation of the fluorescence stop gap does not depend on the depth of the sources. We can exclude the possibility that the depth dependence is washed out by a diffuse excitation beam: Fig. 5.3 shows that there is a large transmission of light at the excitation wavelength. Indeed we observed a well-defined blue beam behind the sample. From the ob-

servation that the stop gap is already present for sources close to the surface, we conclude that the stop gap takes only few crystal planes to build up. It is striking that the attenuation in the stop gap does not increase with further increasing depth of the source. Apparently the attenuation in the stop gap in the transfer function is mostly determined close to the surface but not by the bulk of the crystal.

We verified that the fluorescence originates in the bulk of the sample by photochemically bleaching the dye close to the surface with an intense laser beam tuned to a Bragg reflection. Due to reflection from the lattice planes, the laser beam penetrates only a short distance into the sample, and it predominantly bleaches the dye close to the surface. The bleaching did not deepen the stop gap, so we can exclude that the residual light comes from fluorescent dye close to the surface. The bleaching experiment also demonstrates that the residual light in the stop gap is not due to surface modes of the photonic crystal. We will explain below that the contribution of fluorescence generated in the surface layer to the residual light in the stop gap is indeed expected to be small.

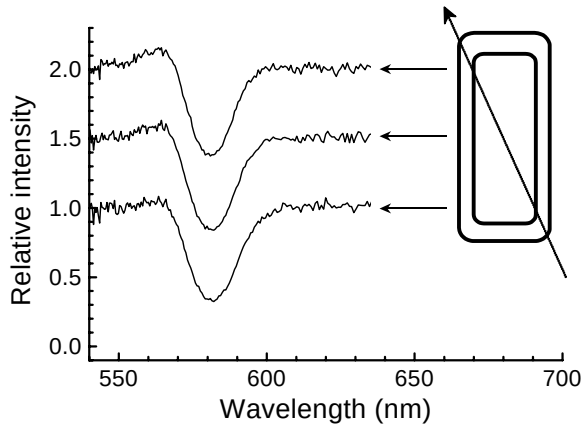

Figure 5.6 *Transfer functions (relative fluorescence intensities) for various distances from light source to sample surface, in a similar crystal as in Fig. 5.3. The depth of the light source varies with the depth of the light beam which excites the fluorescence (see schematic drawing). The upper curves have been offset by* 0.5 *and* 1.0 *respectively. Each curve corresponds to the position in the sample as indicated.*

5.4 Propagation of light inside crystals

From a comparison between the transfer function and the transmission spectrum (Fig. 5.3), it is clear that a considerable amount of fluorescence light with wavelengths in a stop gap reaches the sample surface and then leaves the crystal in the direction of a stop gap. The explanation for this phenomenon is that defects near the surface of the crystal scatter in all directions, including the direction of the stop gap. The phenomenon can be understood as follows: Light emitted in the direction of a stop gap is attenuated, but the light can propagate perfectly well in other directions (Fig. 5.1a, Fig. 5.4). The light will be scattered by a small concentration of defects that always occur in any crystal.[10] Radiation scattered by defects deep inside the crystal will experience an attenuation similar to that in a plane wave experiment. If light is scattered by defects close to the surface of the crystal, this radiation will appear unattenuated outside, even in the direction of a stop gap, because the light traverses only a thin layer of photonic crystal. Thus, light appears in the direction of a stop gap. The intensity is determined solely by the defects that are close to the surface, defects that are deeper inside the sample do not contribute. The internal sources emit light in a large solid angle of nearly 2π to the front surface, hence an appreciable contribution is expected compared with the light that directly propagates into the 0.016π solid angle of the detector. In contrast, in a plane wave transmission spectrum the contribution of diffuse scattering is hardly noticeable. The reason is that the beam that propagates to the detector is well collimated, whereas the randomly scattered light is spread over 4π solid angle. This elucidates why the stop gap in fluorescence is shallower than the deep stop gap in plane wave transmission spectra (*cf.* Fig. 5.3).

To give our explanation a quantitative basis, we now estimate the attenuation in the stop gap of the transfer function, which is determined by fluorescent light emanating from a surface layer. We distinguish two main contributions to this fluorescence intensity: (1) fluorescence generated in the surface layer itself by scattered blue light from the excitation beam, and (2) scattering in the surface layer of red fluorescence light generated deeper inside the sample, see Fig. 5.1a. Both contributions depend on the thickness of the surface layer and on the diffuse scattering of the blue or red light. The thickness of the surface layer was determined by comparing the fluorescence intensity of such a layer – excited by a blue beam at the Bragg condition – to the fluorescence intensity produced by an incident beam that illuminates the whole sample thickness. The excitation beam was Bragg reflected at the back surface of the sample and the resulting fluorescence was detected outside the stop gap. Under Bragg excitation, we find a fluorescence intensity 6 times lower than found when illuminating the whole 300 μm sample thickness away from Bragg reflection. Apparently the surface layer is about $300\ \mu\text{m}/6 = 50\ \mu\text{m}$ thick.

Based on this layer thickness, one would expect a transmission in the stop gap of $\exp(-6) = 0.3\%$. This estimate agrees very well with the measured transmission in the stop gap in Fig. 5.3. The amount of diffuse scattering in the sample can be estimated from the transmission. For the blue excitation beam the transmission is $\sim 60\%$ (see Fig. 5.3), so at most 40% of the incident light is scattered. Half of the scattered light reaches the front surface. We can now estimate the contribution (1) above: scattered blue light which excites the surface layer contributes $(40\%/2)/6 = 3\%$ to the transfer function. Similar reasoning leads to an estimate of the contribution (2) of fluorescence light scattered in the surface layer, however the fluorescence is scattered more strongly because it is close to a stop gap.[11] In a separate experiment, we have observed that scattering close to a stop gap can be a factor 3 to 4 stronger than far away from the stop gap. The contribution (2) is accordingly larger, *i.e.* $\sim 10\%$. The resulting estimate for the relative intensity in stop gap of the transfer function is then $\sim 3\% + 10\%$. This should be compared with the observed stop gaps in Fig. 5.3 of about 20%. The estimated stop gap depth agrees well with observed attenuations in stop gaps, confirming the mechanism that we propose.

With the mechanism described above we can also explain the difference between the widths of the stop gaps in fluorescence and transmission. The fluorescence stop gap is caused by relatively few crystal planes that are well aligned close to the cell wall, therefore the measured stop gap width agrees well with the purely photonic width. A simple model calculation reveals that approximately 50 lattice planes (~ 20 μm thickness) suffice to yield the width of 12 nm without finite size Scherrer broadening.[9] The width of the fluorescence stop gap comes close to the width of the peak in reflection spectra,[15] because both are caused by the outermost crystal planes. The stop gap in transmission on the other hand, samples the complete thickness of the sample (more than a thousand lattice planes), including planes far from the capillary wall which may be less well aligned. Thus the diffuse scattering mechanism accounts not only for all of our experimental observations, it also explains previous uninterpreted data.[1–6]

5.5 Conclusions

We have studied propagation of light generated inside high quality photonic crystals. Close to stop gaps, the propagation is determined by defects near the surface. The effect is confirmed by a quantitative analysis of the observed attenuations. Our result has an important bearing on the long awaited photonic band gap: In that case, a source inside a crystal cannot emit in any direction, hence the source of diffuse light is shut off. In a material with a photonic band gap, this diffuse contribution

to the transfer function vanishes over the full spectral width of the gap. It appears that a small number of defects that is unavoidable even in high quality crystals is an excellent probe for photonic band gap crystals. We conclude that the transport of light in photonic crystals consists of an intricate combination of propagation (away from stop gaps), and diffuse scattering (at the stop gaps) typical of random samples. For the latter, a large body of work already exists, which should facilitate detailed theoretical interpretation.[16]

References

1. V. N. Bogomolov, S. V. Gaponenko, A. M. Kapitonov, E. P. Petrov, N. V. Gaponenko, A. V. Prokofiev, A. N. Ponyavina, N. I. Silvanovich, and S. M. Samoilovich, 'Photonic band gap phenomenon and optical properties of artificial opals', *Phys. Rev. E* **55**, 7619-7625 (1997).
2. E. P. Petrov, V N. Bogomolov, I. I. Kalosha, and S. V. Gaponenko, 'Spontaneous emission of organic molecules embedded in a photonic crystal', *Phys. Rev. Lett.* **81**, 77-80 (1998).
3. T. Yamasakiand T. Tsutsui, 'Spontaneous emission from fluorescent molecules embedded in photonic crystals consisting of polystyrene spheres', *Appl. Phys. Lett.* **72**, 1957-1959 (1998).
4. K. Yoshino, S B. Lee, S. Tatsuhara, Y. Kawagishi, M. Ozaki, and A A. Zakhidov, 'Observation of inhibited spontaneous emission and stimulated emission of rhodamine 6G in polymer replica of synthetic opal', *Appl. Phys. Lett.* **63**, 3506-3508 (1998).
5. A. Blanco, C. López, R. Mayoral, H. Miguez, F. Meseguer, A. Mifsud, and J. Herrero, 'CdS photoluminescence inhibition by a photonic structure', *Appl. Phys. Lett.* **73**, 1781-1783 (1998).
6. H. Miguez, A. Blanco, F. Meseguer, C. López, H. M. Yates, M. E. Pemble, V. Fornés, and A. Mifsud, 'Bragg diffraction from inidum phosphide infilled fcc silica colloidal crystals', *Phys. Rev. B* **59**, 1563-1566 (1999).
7. W. L. Vos, R. Sprik, A. van Blaaderen, A. Imhof, A. Lagendijk, and G. H. Wegdam, 'Strong effects of photonic band structures on the diffraction of colloidal crystals', *Phys. Rev. B* **53**, 16231-16235 (1996); 'Erratum', *ibid.* **55**, 1903 (1997).
8. J. C. Maxwell-Garnett, 'Colors in metal glasses and in metallic films', *Phil. Trans. Royal Soc. A* **203**, 385-420 (1904); 'Colors in metal glasses, in metallic films, and in metallic solutions', *ibid. A* **205**, 237-288 (1906).
9. R. W. James, *The Optical Principles of the Diffraction of X-Rays* (Bell & Hyman, London, 1962).

10. N. W. Ashcroft and N. D. Mermin *Solid state physics* (Holt, Rinehart, and Winston, New York, 1976), p. 616.
11. P. A. Rundquist, P. Photinos, S. Jagannathan, ans S. A. Asher, 'Dynamical Bragg diffraction from crystalline colloidal arrays', *J. Chem. Phys.* **91**, 4932-4941 (1989).
12. K. M. Ho, C. T. Chan, and C. M. Soukoulis, 'Existence of a photonic gap in periodic dielectric structures', *Phys. Rev. Lett.* **65**, 3 (1)52-3155)1990.
13. Ì. Ì. Tarhan and G. H. Watson, 'Photonic band structure of fcc colloidal crystals', *Phys. Rev. Lett.* **76**, 315-318 (1996).
14. D. Labilloy, H. Benisty, C. Weisbuch, T.F. Krauss, R.M. De La Rue, V. Bardinal, R. Houdré, U. Oesterle, D. Cassagne, and C. Jouanin, 'Quantitative measurement of transmission, reflection, and diffraction of two-dimensional photonic band gap structures at near-infrared wavelengths', *Phys. Rev. Lett.* **79**, 4147-4150 (1997).
15. W. L. Vos, J. E. G. J. Wijnhoven, and M. Megens, *Conference on lasers and Electro Optics Europe*, September 1998 (IEEE/LEOS, Piscataway NJ, 1998) p. 361.
16. A. Ishimaru, *Wave propagation and scattering in random media* (Academic Press, New York, 1978).

6
Fluorescence lifetimes and linewidths of dye in photonic crystals

6.1 Introduction

One of the most important consequences of photonic band structures is that spontaneous emission of excited atoms or molecules can be inhibited.[1] Surprisingly, experimental studies of excited atoms or molecules in photonic crystals are scarce,[2,3] and important aspects of spontaneous emission have not been addressed, *i.e.* the spectral width of stop gaps or band gaps as compared to the emission linewidth and the mechanism that is responsible for this linewidth. The relevance of line broadening becomes clear if one considers the emission linewidth of atoms or molecules in a photonic band gap crystal in relation to the width of the gap. The linewidths of important systems such as efficiently radiating dyes or luminescing semiconductors are generally very large, *i.e.* comparable to the width of a gap,[4] which justifies the question of whether a photonic gap will ever cause any observable effect on the radiative lifetime at all. On the other hand, even weakly photonic crystals change the emission spectrum of embedded atoms or molecules considerably: the spectrum acquires a pronounced stop gap. The appearance of a stop gap in the emission spectrum suggests that the photonic band structure might also affect the radiative lifetime. To determine the influence of the photonic band structure on radiative lifetimes, we have experimentally investigated the excited state lifetime and its wavelength dependence for molecules in photonic crystals and in a non-crystalline reference sample.

6.2 Experiment

To experimentally realize spontaneously emitting sources inside photonic crystals, we used the dye-doped silica spheres described in chapter 4. Fluorescence lifetimes

of the dye in the crystals were obtained using a time-correlated single photon counting technique.[5] The dye is excited in the UV at a wavelength of around 320 nm by the second harmonic of a cavity-dumped dye laser that uses Kiton Red as the active medium. The dye laser is synchroneously pumped by a mode-locked Nd^{3+}:YAG laser. The UV excitation beam of < 1 ps pulses is focused onto the back of the sample, *i.e.* onto the side of the sample away from the detector. The power was always lower than 1 μW. The diameter of the beam is less than 0.5 mm at the sample position. A lens images the fluorescence on the entrance slit of a Carl-Leiss prism monochromator. The spectrometer slits were set at 1 mm, which results in a resolving power of ~ 15 nm. A Hamamatsu R3809U Micro Channel Plate detector (MCP) detects the fluorescence. At a cavity dump rate of 40 kHz, the count rate on the MCP was at most a few kcounts/s. The MCP signal is amplified and fed to a constant fraction discriminator and time to amplitude converter (TAC). A photodiode monitors the incident beam for triggering the TAC. The time difference between the MCP signal and the excitation pulse is recorded by a multi-channel analyzer. With this setup we achieve a time resolution of around 55 ps (FWHM of scattered red light from the dye laser).

The resulting time-resolved fluorescence data are plotted as histograms. We have adjusted the widths of the histogram bins to maintain a good signal to noise ratio at long times, exploiting the fact that decay curves are monotonously decreasing functions of time. This monotonous decrease suggests to use bins so wide that the random error in the bin heights is comparable to the difference between heights of consecutive bins. For the Poisson distributed noise of a single photon counting experiment, and a single-exponential decay curve with characteristic time τ, the criterion leads to a straightforward recipe for the histogram bin width Δ at time t, specifically $(\Delta/\tau)^3 = 2/[N\exp(-t/\tau)]$, where N is the total number of counts. We find it expedient to plot exponential data in this way since such a presentation emphasizes the information in the data since it averages out the noise; it is straightforward to apply, and it has a clear basis.

6.3 Results

Figure 6.1 shows two typical time-resolved fluorescence traces, one of dye in a colloidal crystal and one of dye in a colloidal liquid, measured at a wavelength of 577 nm, corresponding to the crystal's stop gap. The measured fluorescence intensities extend over three full decades. The fluorescence decay is very close to single exponential, which indicates that unwanted nonradiative effects are effectively reduced by the low dye concentration and the protective cover layer. From the fluorescence decay curves we have obtained lifetimes by calculating the aver-

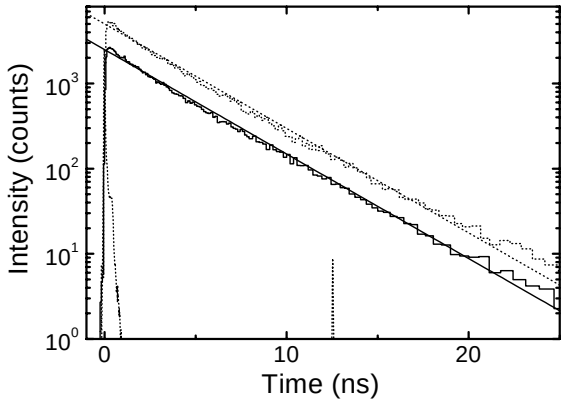

Figure 6.1 *Time-resolved fluorescence of dye inside a photonic colloidal crystal of* 65 *vol% (—) and in a colloidal liquid (···, offset by a factor of* 2*), at* 577 *nm wavelength. The mean lifetimes of* 3.54 ± 0.02 *ns are indicated by straight lines. The narrow spike is the instrument response.*

age time at which a photon is detected. The lifetimes for the curves in Fig. 6.1 are both 3.5 ns, *i.e.* there is no large difference in lifetime for a crystal and a colloidal liquid. Fig. 6.2 shows fluorescence lifetimes as a function of wavelength in the dye spectrum, for two photonic crystals with different densities, and for a colloidal liquid. The emission spectrum of one of the crystals is included in the same figure for reference. We will discuss fluorescence lifetimes in the crystals first, later on we will come back to the colloidal liquid. The densities of the crystals that we have used were 65 and 53 vol%. Due to the density difference the center wavelength of the stop gaps of the crystals differ: for the low density crystal the stop gap is at 617 ± 9 nm, whereas for the high density crystal it is at 582 ± 2 nm. Since the stop gap wavelengths of the two crystals differ, the densities of optical modes of the two crystals should also display different wavelength dependencies. This difference should become visible in the measured lifetimes. However, the measured lifetimes in these crystals do not show a significant wavelength dependence. The variations in lifetime are on the order of only 0.05 ns, or 2%. This observation shows that the influence of the photonic band structure on lifetime in these crystals is surprisingly small, considering the large changes in the spectra. Below we will resolve this seeming paradox.

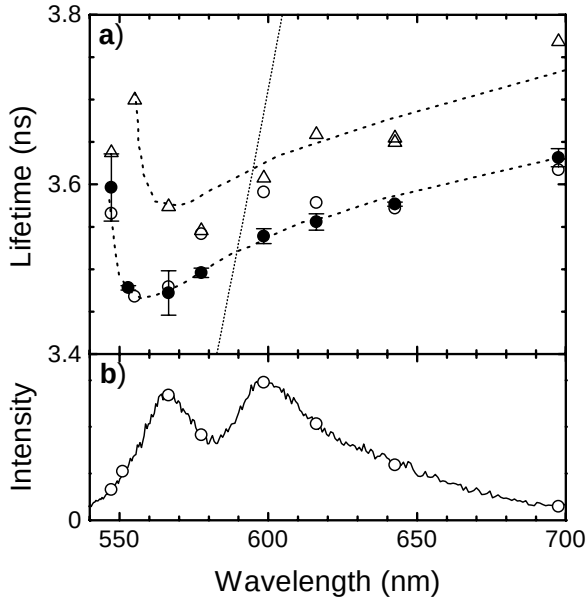

Figure 6.2 *(a) Excited state lifetime of dye inside photonic crystals with densities of* 65 *vol% (○) and* 53 *vol% (●), and in a colloidal liquid (△), at various wavelengths in the dye spectrum. The solid circles are an average of two measurements, indicated by error bars. The dotted curves are guides to the eye. The emission spectrum of the more dense (*65 *vol%) sample is shown in (b) for comparison. The open circles indicate wavelengths at which lifetime measurements were performed.*

6.4 Discussion

We can interpret the variation in lifetimes by comparing this variation to the width of the stop gaps of the crystals. A simple model connects the lifetimes to the width of the stop gaps, and it explains why the photonic crystals under study have only a small influence on lifetimes. In the direction of a stop gap, light cannot be emitted since the zero point fluctuations are expelled from the photonic crystal by repeated reflection from the lattice planes. Since our crystals do not have a photonic band gap, light at a specific wavelength is reflected only for certain directions, in the other directions the emission persists. We expect that the relative change in radiative lifetime of the fluorescent molecules is of the order of the solid angle Ω subtended by the Bragg reflections, compared to the full 4π solid angle which is available in the absence of a crystal. For atoms in a Fabry-Pérot interferometer the results of this approach are in excellent agreement with the experiments of Heinzen

et al..[6] The lifetime change for a stop gap at a specific frequency is

$$\frac{\Delta\tau}{\tau} = \frac{\Omega}{4\pi} = 4 \times 2 \times \frac{2\pi(\cos\theta_- - \cos\theta_+)}{4\pi}. \tag{6.1}$$

Here, θ_- and θ_+ are the inner and outer half apex angles of the Kossel cone. The factor of 4 is included because there are four pairs of $\{111\}$ planes, the factor of 2 accounts for the two sides of the planes. The change in lifetime depends on the emission frequencies of the fluorescent molecules via the angles θ_+ and θ_-. To estimate θ_+ and θ_- we have calculated the stop gap width using an extended version of conventional dynamical diffraction theory.[7] We have extended the theory to incorporate reflection at angles close to backscattering, and we have refrained from the customary approximation that the Kossel line occurs close to the conventional Bragg reflection. We consider here only polarization perpendicular to the scattering plane; this polarization gives the largest stop gaps. We will express the results in terms of the photonic strength parameter Ψ.[8] It appears that the solid angle contained in a stop gap is largest when the full Kossel cone has just come into view close to normal incidence on a set of planes, *i.e.* when $\theta_- = 0$. This situation occurs when the frequency of the light is at the top of the stop gap for normal incidence. The Kossel cone then extends to θ_+, which is determined by

$$\tan\theta_+ = \sqrt{2\Psi\frac{1+\Psi}{1-\Psi}} \approx \sqrt{2\Psi}. \tag{6.2}$$

The resulting change in lifetime is

$$\frac{\Delta\tau}{\tau} = 4 \times \left(1 - \frac{1}{\sqrt{1+2\Psi(1+\Psi)/(1-\Psi)}}\right) \approx 4\Psi, \tag{6.3}$$

where the factor of 4 is due to the four pairs of $\{111\}$ planes. The relative change in lifetime is directly related to the relative width of the stop gap in the spectrum. The relative spectral width $\Delta\omega/\omega$ of the stop gap for transmission normal to the crystal planes is

$$\frac{\Delta\omega}{\omega} = \sqrt{1+\Psi} - \sqrt{1-\Psi} \approx \Psi. \tag{6.4}$$

We can obtain this width from *e.g.* the fluorescence spectrum in the previous chapter. However one should realize that the width of the stop gap in the fluorescence spectrum is not exclusively caused by the photonic band structure. The stop gap may be broadened by structural defects.[7,9] Indeed the stop gap in fluorescence spectra is usually wider than the peak in reflection spectra. The widths of observed reflection peaks agree well with theoretical calculations.[9] For our estimate of the lifetime change (Eq. 6.1) we have used a stop gap width of 2%, which corresponds to a

change in radiative lifetime of only 0.3 ns. The estimated radiative lifetime change provides an upper bound for changes in fluorescence lifetimes. This upper bound is consistent with the measured variations in τ of the crystals in Fig. 6.2. Apparently a large change in fluorescence spectrum can coincide with an only minor change in fluorescence lifetime, which resolves the paradox mentioned in the introduction.

The observed small change in lifetime contrasts with earlier results. Martorell and Lawandy[2] found a change in lifetime by a factor 1.8 for their crystals of polystyrene spheres in water with rhodamine dye dissolved in the liquid. It has been suggested that their large change in lifetime is not caused by photonic band structure but by other factors such as chemical interactions and adsorption of the dye on the sphere surfaces.[10] To avoid such effects, we have carefully synthesized spheres in which the dye is incorporated and shielded inside. Petrov *et al.*[3] have measured fluorescence of dye in a polymer-filled opal. The decay curves were fitted with a distribution of lifetimes, in which the short lifetimes were about half as long as the long lifetimes. The nonexponential decay was attributed to a modified density of optical modes while chemical or nonradiative effects were not considered. The fluorescence lifetimes were not spectrally resolved to demonstrate the variation in density of optical modes with wavelength. Surprisingly, life time changes were noted for wavelengths at the low frequency side of the stop gap, where $\theta_+ = 0$ and Eq. 6.1 predicts no lifetime change. In both of the previous studies, the widths of the stop gaps of the samples are the same as the width of the stop gaps of our crystals, hence the change of the radiative lifetimes should in all cases be similar to the data in Figs. 6.1 and 6.2.

We will now discuss the lifetimes that we measured in a colloidal liquid. We find that in the colloidal liquid, the fluorescence lifetimes are generally slightly longer than in the photonic crystals. This increase in lifetime is probably a result of random multiple scattering rather than the photonic band structure. Random multiple scattering can considerably increase the path length from dye to detector. If the light propagates diffusively through the sample, then the length of the traversed path s is proportional to the square of the displacement d. In three dimensions $s/l = 3(d/l)^2$, where l is the mean free path. The mean free path l in the sample can be estimated from the Mie scattering cross section σ of the spheres and the density n, $l = (n\sigma)^{-1} = 10 \pm 2$ μm. For displacements d of the order of the sample thickness, 0.3 mm, the resulting path length s is 30 mm. Such a path length corresponds to a delay of 0.09 ns, of the order of the observed difference in lifetimes between the crystals and the colloidal liquid.

Apart from the small systematic difference in lifetimes between the photonic crystals and the colloidal liquid, it appears that all the measured lifetimes in Fig. 6.2 show a common trend in their wavelength dependence. The excited state lifetime τ that we have measured corresponds to a transition rate $1/\tau$ which is a sum of both ra-

diative and nonradiative transition rates, $1/\tau = 1/\tau_{\rm rad} + n_{\rm nonrad}$. The radiative decay rate can be calculated with Fermi's Golden Rule using the density of optical modes. It is through this density of modes that a strongly photonic crystal may influence the excited state lifetime. Even without photonic crystal the density of modes has a pronounced frequency dependence. In vacuum, the density of modes per unit volume $\rho_{\rm vac} = \omega^2/(\pi^2 c^3)$.[11] The transition dipole matrix element in Fermi's Golden Rule contributes yet another factor ω to the transition rate,[11] hence we have plotted a cubic function in Fig. 6.2 for comparison. The frequency dependence of the radiative transition rate explains why the lifetime is shorter at short wavelengths, but the line is clearly much too steep compared to the data. The leveling of the slope may be due to nonradiative decay. Nonradiative decay is expected to become faster towards lower frequencies,[12] hence the slope of the lifetimes τ in Fig. 6.2 is not as steep as the cubic curve. The curve is still sloping upward because the variation in density of states $\rho_{\rm vac}$ dominates the nonradiative decay, since quantum efficiencies of dyes are high.[13]

Finally we want to point out that the phenomenon of line broadening is pertinent to the determination of the density of modes via fluorescence lifetime measurements. There are two kinds of line broadening, each with a different effect on lifetimes. The two contributions to the total width of the spectrum are called homogeneous linewidth and inhomogeneous linewidth.[11,14] The homogeneous linewidth is the width of the spectrum of individual atoms or molecules. This width can be measured by techniques like spectral hole burning or photon echo.[14] The homogeneous linewidth can be much larger than the natural linewidth due to interactions with the environment, *i.e.* dephasing. The inhomogeneous linewidth corresponds to the variation in center frequencies of the atoms or molecules. Due to this variation, the total spectral width of an ensemble of molecules is larger than the linewidth of an individual molecule. Measured fluorescence lifetimes are inherently an average over a wavelength region corresponding to the spectrum of individual molecules, *i.e.* over the homogeneous linewidths.[14] Thus, to avoid averaging out any changes in lifetime due to photonic band structure, it is desirable to have a homogeneous linewidth smaller than the width of peaks and valleys in the density of modes. However one would also like to have a wide fluorescence spectrum so the photonic band structure can be probed at various frequencies. These two requirements may seem contradictory at first, but both conditions are satisfied at once if one uses a system with an inhomogeneously broadened emission spectrum, *i.e.* if one uses an ensemble of molecules with different center frequencies. Each molecule will probe the density of optical modes within its own narrow homogeneous linewidth; the ensemble of molecules will reveal the density of optical modes over the whole wide inhomogeneously broadened emission spectrum. Organic fluorescent dyes are especially suited as probes of the optical density because

of their large inhomogeneous broadening. The homogeneous linewidth of the dye can be reduced by lowering the temperature.[14] Reducing the linewidth is profitable since it increases the wavelength resolution when measuring the density of optical modes. Lowering the temperature also reduces the nonradiative decay rate advantageously.[12]

References

1. E. Yablonovitch, 'Inhibited spontaneous emission in solid-state physics and electronics', *Phys. Rev. Lett.* **58**, 2059-2062 (1987).
2. J. Martorell and N. M. Lawandy, 'Observation of inhibited spontaneous emission in a periodic dielectric structure', *Phys. Rev. Lett.* **65**, 1877-1880 (1990).
3. E. P. Petrov, V. N. Bogomolov, I. I. Kalosha, and S V. Gaponenko, 'Spontaneous emission of organic molecules embedded in a photonic crystal', *Phys. Rev. Lett.* **81**, 77-80 (1998);
   'Modification of the spontaneous emission of dye molecules in photonic crystals', *Acta Phys. Pol. A* **94**, 761 (1998).
4. A. Blanco, C. López, R. Mayoral, H. Miguez, F. Meseguer, A. Mifsud, and J. Herrero, 'CdS photoluminescence inhibition by a photonic structure', *Appl. Phys. Lett.* **73**, 1781-1783 (1998).
5. D. Bebelaar, 'Time response of various types of photomultipliers and its wavelength dependence in time-correlated single-photon counting with an ultimate resolution of 47 ps FWHM', *Rev. Sci. Instrum.* **57**, 1116-1125 (1986).
6. D. J. Heinzen, J. J. Childs, J. E. Thomas, and M. S. Feld, 'Enhanced and Inhibited Visible Spontaneous Emission by Atoms in a Confocal Resonator', *Phys. Rev. Lett.* **58**, 1320-1323 (1987).
7. R. W. James, *The optical principles of the diffraction of X-rays* (Ox Bow Press, Woodbridge, 1962).
8. W. L. Vos, R. Sprik, A. van Blaaderen, A. Imhof, A. Lagendijk, and G. H. Wegdam, 'Strong effects of photonic band structures on the diffraction of colloidal crystals', *Phys. Rev. B* **53**, 16231-16235 (1996); ''Erratum", *ibid.* **55**, 1903 (1997).
9. W. L. Vos, J. E. G. J. Wijnhoven, and M. Megens, *Conference on lasers and Electro Optics Europe*, September 1998 (IEEE/LEOS, Piscataway NJ, 1998) p. 361.
10. P. K. John, Y.-t. Zhu, Y. S. Liu, S. K. Wong, and W. R. Ware, 'Fluorescence-lifetime measurements in monodispersed suspensions of polystyrene particles', *J. Opt. Soc. Am. B* **10**, 356-359 (1993); N. M. Lawandy, 'Fluorescence-lifetime measurements in monodispersed suspensions of polystyrene particles:

comment', *ibid.* **10**, 2144-2146 (1993); M. Tomita, K. Ohosumi, and H. Ikari, 'Enhancement of molecular interactions in strongly scattering dielectric composite optical media', *Phys. Rev. B* **50**, 10369-10372 (1994).
11. R. Loudon, *The quantum theory of light* (Clarendon Press, Oxford, 1983).
12. *Organic molecular photophysics*, edited by J. B. Birks (Wiley, London, 1973).
13. F. J. Duarte and L. W. Hillman, *Dye laser principles* (Academic Press, San Diego, 1990).
14. M. D. Levenson and S. S. Kano, *Introduction to Nonlinear Laser Spectroscopy* (Academic Press, San Diego, 1991).

7

X-ray diffraction of photonic colloidal single crystals

7.1 Introduction

It is crucial to know the structure of self-organizing photonic colloidal crystals, since their optical properties are intimately connected to the crystal structure. The important class of charge stabilized colloids[1] is particularly promising for photonic purposes, because the lattice parameters can be tuned with the ionic strength.[2] The photonic properties are optimal for particle densities φ in the range 20–50 vol%, because the Bragg resonances of the lattice are then matched with the internal Mie resonances of the particles.[3] The crystal structure of dense charge stabilized colloids with $\varphi > 0.1$ is expected to be fcc.[1] Interestingly however, experiments at $\varphi > 0.3$ have revealed glass formation instead of crystallization.[4] Application of shear prevents vitrification but results in random stacks of hexagonal close-packed planes (rhcp)[5] or possibly hexagonal close packing (hcp)[6] instead of fcc. From a photonic perspective, an fcc structure is more desirable.[7]

The desired strong interaction between photonic crystals and light hampers structure determination by light scattering or other optical methods.[8] Therefore, we use small angle x-ray scattering (SAXS)[9] with a synchrotron source, which has the advantages of a high wavelength resolution, a tightly focused beam, and a high photon flux, in comparison to *e.g.* neutron scattering. With such a source, diffraction patterns can be recorded directly on a two-dimensional detector camera. This has the advantage over other small-angle instruments that the scattering pattern is not smeared and that no scanning is necessary.[10] With this technique we have performed the first in-depth systematic study of the structure of a colloidal single crystal.

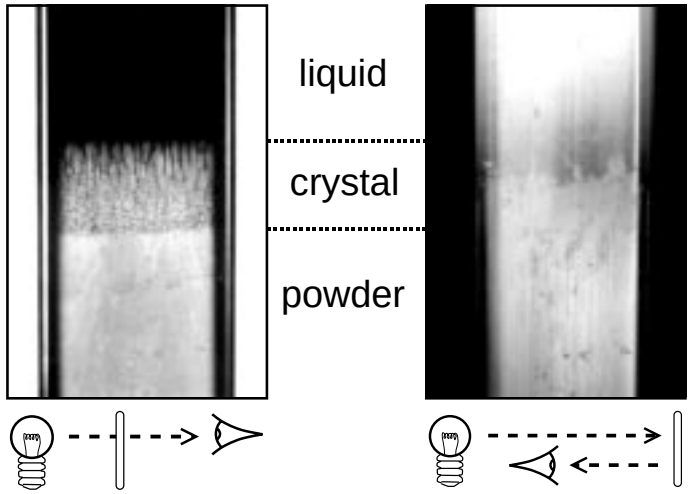

Figure 7.1 *Photographs of a photonic colloidal sample (#231) of sedimented polystyrene spheres (radii* 100.9 *nm, size polydispersity* 2.3 *nm) in methanol, contained in a* 4 *mm wide capillary. The pictures were taken with white light, in transmission (left), and in reflection (right), as indicated by the cartoons. For a comparison of the images, some light was also reflected in the left picture.*

7.2 Colloidal crystals

We have grown charge stabilized single crystals with volume fractions up to 60 vol% and dimensions up to 0.5 mm (see Fig. 7.1), which is large enough to isolate a single photonic crystal for experimental study. The samples were made of polystyrene spheres (Duke Scientific) in water or methanol, that were sealed in 0.3 or 0.4 mm thick flat glass capillaries (Vitro Dynamics). Crystals with densities below 50 vol% were made by deionizing the suspensions with ion exchange resin (BioRad AG501-X8) before introducing the suspension in the capillaries. The best results were obtained with crystals that nucleated and grew over periods on the order of months. Adding extra ion exchange resin to the capillaries increases the nucleation and growth rates, which results in more and smaller crystals. Dense crystals ($\varphi > 50$ vol%) were grown by sedimentation of charge screened colloids at accelerations of $\sim 400\ g$. This corresponds to a ratio of the sedimentation velocity to diffusion velocity (known as the Péclet number) of about 0.02, which suggests that the sediment is in thermodynamic equilibrium. The crystal-liquid interface appears at densities near 50 vol%, close to the hard sphere crystallization density. After about 4 hrs, relatively large grains develop at the crystal-liquid interface, that anneal to sizes on the order of 0.5 mm. Longer centrifugation times result in

compression of the crystals ($\varphi > 60$ vol%), but also causes them to break up into a polycrystalline assembly.[11]

Photographs of such a photonic colloidal sample of polystyrene spheres are shown in Fig. 7.1. The density of colloids increases from top to bottom. In the upper part of the sample, the particles form a colloidal liquid in which incident light is randomly multiple scattered, hence it appears opaque in transmission and white in reflection. In contrast, photonic crystals transmit incident light unless Bragg reflections occur, which are a precursor of photonic band gaps.[12,13] In this particular sample, green light is Bragg reflected (right panel) and the red part of the optical spectrum is transmitted (left panel). The green Bragg reflections are caused by close packed crystal planes parallel to the capillary wall (fcc 111 planes). Just below the liquid, crystals are visible that are large enough for a single crystal diffraction study. They are separated by dark grain boundaries, and several of them are not oriented with the close-packed planes parallel to the glass, hence their Bragg reflection is not visible. Further below, the sample is polycrystalline.

7.3 Experiments

The SAXS experiments were performed on beamline 4 of the ESRF,[14] at wavelengths λ of 0.147 25 nm and 0.098 80 nm. The incident beam was tightly collimated and very monochromatic. The bandwidth $\Delta\lambda/\lambda$ of 1.5×10^{-4} corresponds to a longitudinal coherence length[15] of $(\lambda/\Delta\lambda)\lambda \sim 0.7$ μm. The beam divergence $\Delta\theta$ of only 30 μrad corresponds to a transverse coherence length[15] of $\lambda/\Delta\theta \sim 6$ μm. The beam was focused to a narrow spot of about 0.2×0.5 mm, with a maximum beam flux of 10^{13} photons/s. The scattered radiation was detected with a two-dimensional gas filled detector at the maximum distance of 10 m from the sample. The smallest scattering vector $s = 2\sin(\theta)/\lambda$, with θ the diffraction angle, is 0.002 nm^{-1}. The resolving power of the instrument Δs is about 7×10^{-4} nm^{-1}. At the maximum sample-detector distance, the largest observable wave vector exceeds 8×10^{7} m^{-1}.

The raw diffraction patterns were corrected for the detector efficiency distribution which has been determined using the isotropic fluorescence radiation from a Sr-doped glass.[16] Absolute scattering intensities have been obtained by using a calibrated Lupolen polymer sample as a reference. We have obtained the differential scattering cross section per unit volume I_v by dividing the number of counts in a detector pixel by the number of incident photons, the solid angle subtended by the detector pixel, the transmission of the sample, and its thickness. Background intensities caused by scattering from the capillary, window of the detector vacuum chamber, and beam stop were determined by separate measurements on empty cap-

illaries and subtracted. To correct for the contributions from scattering by inhomogeneities inside the particles (fluctuation-induced scattering) we also subtracted a small constant.

The capillaries were mounted with their long axis vertical on two translation stages that scanned the spatial position with respect to the horizontal x-ray beam, and a rotation stage that scanned about the long axis of the samples (ω-axis).[17] The crystal diffraction patterns for Fig. 7.2 were collected in 105 seconds. The typical integration time for form factor measurements was 600 seconds, which yields about 10^8 counts on the detector.

7.4 Diffraction

Figure 7.2 presents x-ray scattering patterns of a single crystal consisting of $r = 120.8$ nm spheres with a lattice parameter $a = 370$ nm and a volume fraction $\varphi = 56$ vol%. Many Bragg peaks are seen, which indicates that the spheres are ordered in a crystalline array. When the sample is translated, we observe doubling or tripling of each peak or even concentric rings at the radii of the peaks, which signifies that the incident beam then irradiates two, three or many crystals respectively. Therefore, Fig. 7.2 shows indeed the scattering patterns of a single colloidal crystal. Many Bragg diffraction peaks are observed simultaneously, in contrast to x-ray diffraction of atomic single crystals.[17] The reason is that the wavelength λ is much smaller than the typical lattice spacings d, hence the radius $1/\lambda$ of the Ewald scattering sphere is much larger than the lengths $1/d$ of the reciprocal lattice vectors. Consequently, the Ewald sphere becomes a scattering plane that simultaneously intersects many reciprocal lattice vectors.[5,17] The Bragg peaks in Fig. 7.2A have approximately a sixfold symmetry. This is expected because dense colloids usually order in hexagonal close packed planes that lie parallel to cell windows.[1] The stacking sequence of these planes determines whether the structure is fcc, hcp, rhcp, or a more complex sequence.[17] Due to the hexagonal symmetry, the reciprocal space consists of a hexagonal arrangement of Bragg rods, labeled with Miller indices h, k, and an index l indicating the distance along the rods,[17] see Fig. 7.3. In normal incidence (Fig. 7.2A), $l = 0$ and we are looking down the c-axis. The inner six Bragg peaks in Fig. 7.2A are the $hk = 11$ class reflections. These peaks cannot be the $hk = 10$ class, because this would result in an unphysical density beyond close packing of $\varphi = 88$ vol%. The absence of $hk = 10$ indicates that the crystal is fcc, based on considerations of intensity distributions on the Bragg rods.[17] In Fig. 7.2A, most bright and dark spots occur under conditions expected for fcc, namely $h - k = 3n$, and $h - k = 3n \pm 1$, respectively.

In order to sweep the third dimension of reciprocal space, the scattered inten-

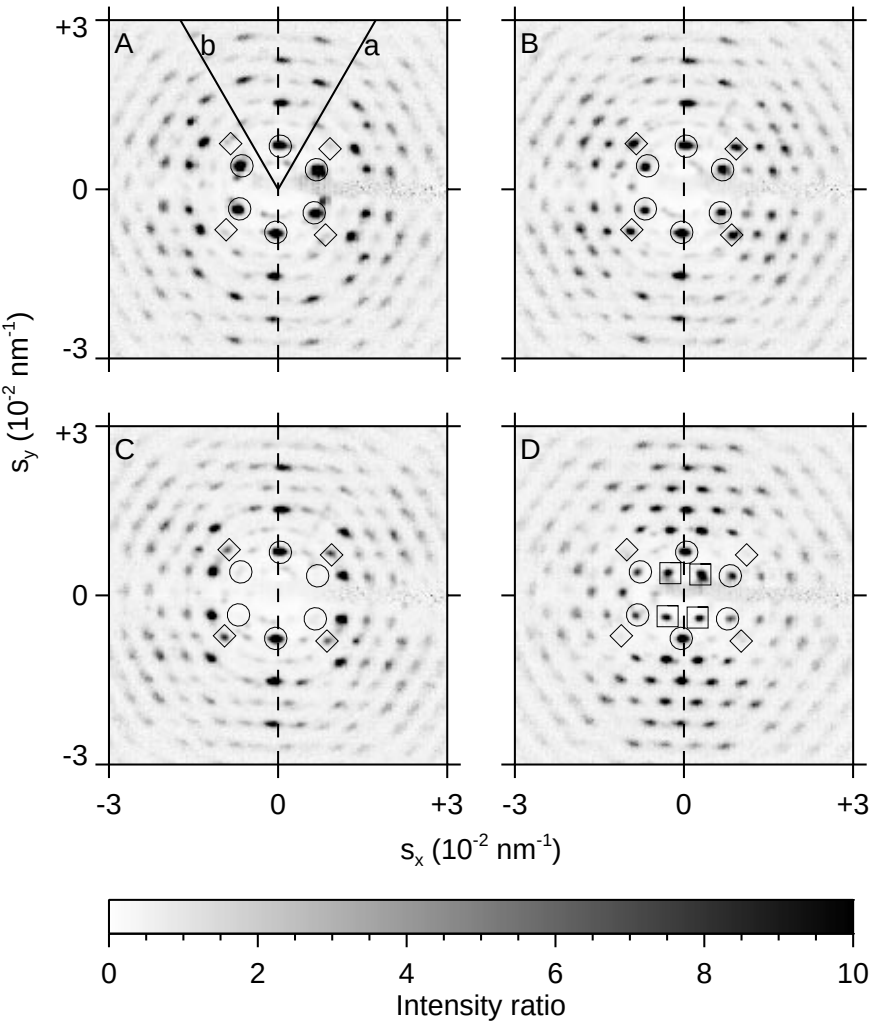

Figure 7.2 *Structure factors at several angles of incidence* ω *of a colloidal single crystal of* 120.8 *nm radius polystyrene spheres (size polydispersity* 1.6 *nm) in water with a volume fraction* $\varphi = 56$ *vol% (sample #300), measured at* 0.09880 *nm wavelength. The data were obtained at angles* ω *of* 0° **(A)**, 6° **(B)**, 14° **(C)**, *and* 34° **(D)**. *The drawn lines are the* a^* *and* b^* *axes in reciprocal space. The rotation axis is* $s_x = 0$ *(dashed lines), hence the spots on this axis are unchanged. The circles indicate the six* $hk = 11$ *class Bragg rods, which peak at* $l = 0$ *(panel A), and* $l = 1$ *(panel D). The diamonds indicate the* $hk = 3\overline{1}$ *Bragg rods, which peak at* $l = 1/3$ *(panel B). The squares in panel (D) indicate the peaks on the* $hk = 10$ *Bragg rods, that appear at* $\omega = 34^\circ$. *These four reflections correspond to the close packed reflections of fcc. The patterns were collected in* 105 *seconds. They have been corrected for the single particle form factor, that was measured separately.*

sity was measured as a function of the angle of incidence ω, see Fig. 7.2A-D. Intersections of the Ewald scattering plane with reciprocal lattice vectors are seen as Bragg spots on the detector, that appear and disappear upon rotation,[18] as illustrated in Fig. 7.3. As a visual aid, we have indicated the positions of several classes of Bragg rods in Fig. 7.2A-D. It is clearly seen that with increasing angle, the $hk = 11$ spots (circles) become weaker (B), completely disappear (C), and reappear at $\omega = 34^\circ$ (panel D). The $hk = 3\overline{1}$ spots (diamonds) on the other hand, start with zero intensity in panel A, have a maximum at 6° (panel B), become weaker (panel C), and have completely disappeared in panel D. The maxima for the 11 class correspond to $l = 0$, and $l = 1$ respectively, which confirms that the crystal consists of interlocked stacks of hexagonal planes.[5,17] The maximum intensities for $hk = 3\overline{1}$ appear at $l = 1/3$, which confirms that the crystal structure is untwinned fcc, and not any other stacking of hexagonal planes such as hcp or rhcp.[17] Moreover, at $\omega = 34^\circ$ (Fig. 7.2D), four spots have appeared close to the beam stop, closer than the $hk = 11$ class reflections (squares). They are the $hk = 10$ class with $l = 1/3$, that correspond to the cubic 111 reflections of the close packed planes – these reflections are absent in hexagonal structures. The 111 reflections perpendicular to the capillary wall are the ones that are visually observed in Fig. 7.1, which demonstrates that x-ray diffraction resolves length scales on the order of optical wavelengths.

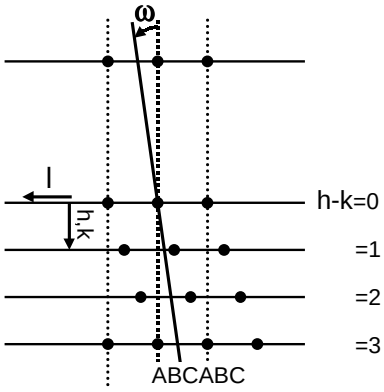

Figure 7.3 *Schematic section through the Bragg rods of an fcc crystal, showing the Ewald plane (thick line) sweeping through reciprocal space.*

The analysis above can be performed systematically for all the *hk* reflections. In Fig. 7.4, we have plotted the scattered intensity along some of the Bragg rods in reciprocal space, bringing together intensities from all the diffraction patterns at various angles of incidence ω. Two varieties of Bragg rods can be distinguished: those with $h-k = 3n$ and those with $h-k = 3n \pm 1$. For the former, one expects peaks at integral l for all hexagonal stacking sequences. Indeed the $2\overline{1}$, 30 and $\overline{3}1$ reflections in Fig. 7.4 (left) show peaks at $l = -1, 0, 1$. The $hk = \overline{3}1$ class of reflections shows that the sequence of peaks persists out to very high Miller indices. The other Bragg rods, with $h-k = 3n \pm 1$, directly reveal the crystal structure. For hcp, peaks should appear at $l = m$ or $m + 1/2$, while for fcc, the peaks are at $l = m + 1/3$ or $m + 2/3$, depending on the stacking sequence (ABCABC or ACBACB) and the Bragg rod ($h-k = 3n+1$ or $3n-1$). For rhcp, broad peaks would appear at $l = m + 1/2$. The $hk = 21$ and 20

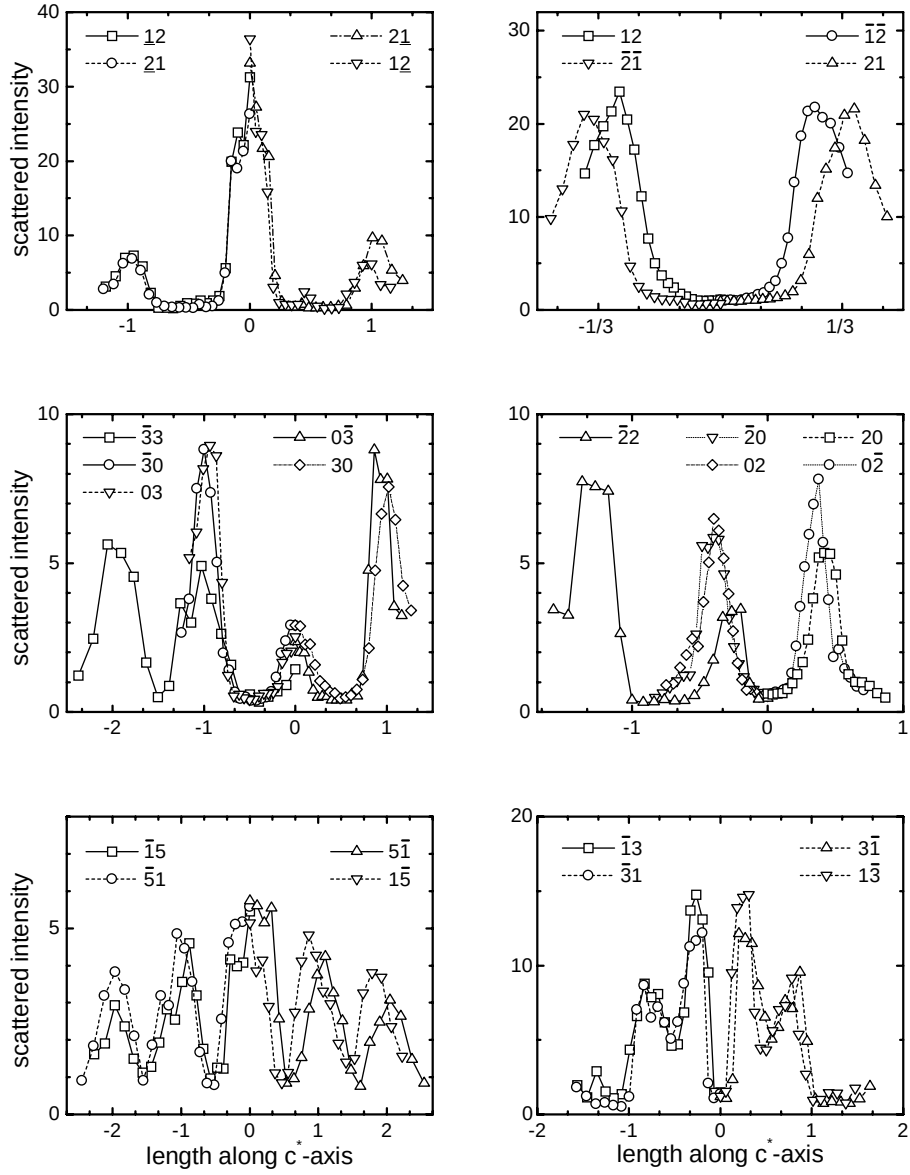

Figure 7.4 *Scattered intensity along Bragg rods in reciprocal space (c^* axis), for several classes of hk reflections. On the left: reflections with $h-k=3n$, resulting in peaks at integral l; on the right: reflections with $h-k=3n\pm1$, leading to l integer $\pm1/3$. The intensities have been corrected by the measured sphere form factor.*

families of Bragg rods in Fig. 7.4 clearly show peaks at $l = \pm 1/3$, which demonstrates that the crystal structure is fcc, not hcp or rhcp. Similar results were obtained for the 10 rods. Notice that the scattered intensity disappears completely at $l = 0$ on the 21 and 20 rods, in contrast with previous observations.[5,6] The absence of $l = 0$ peaks on these $h - k = 3n \pm 1$ rods rules out hcp; for the hcp structure, one would expect a peak at $l = 0$, in addition to three times stronger peaks at $l = \pm 1/2$. The $h - k = 3n \pm 1$ rods also give a clue as to whether the exposed part of the sample is a single fcc crystal or if it consists of twins with mirrored stacking sequences. In Fig. 7.4 we see that the $\overline{2}2$ rod has peaks at $l = -1/3$ and $-4/3$, but not at $l = -2/3$. This indicates that the fcc crystal structure is not twinned. However, the peaks at $l = \pm 1/3$ on the 20 rods imply that we irradiate a crystal with the opposite stacking sequence. For the higher order Bragg rods of this crystal, we have detected more complicated intensity distributions, possibly signaling slight distortions from an ideal fcc lattice. For instance, the $\overline{3}1$ rods show peaks at both $l = 1/3$ and $2/3$, which suggests that we have exposed multiple twinned fcc crystals, albeit probably only a few, because the peaks are not equally intense. Large numbers of twinning planes would result in equal amounts of ABCABC and ACBACB crystals, and hence equal peaks in Fig. 7.4.[5] Some of the high order rods have a tendency for peaks at $l = m + 1/2$, suggestive of stacking faults that are far apart. Some of the intricacies of the current crystal are immediately apparent in Fig. 7.2, when one realizes that the intersection of an Ewald plane through a periodic lattice is itself periodic. Obviously this is not strictly true in Fig. 7.2. Reassuringly, in later experiments we have observed completely periodic diffraction patterns of 111, 110 and even 100 sections through reciprocal space. The observation of a square diffraction pattern from the cubic 100 planes is very convincing evidence for the fcc structure.

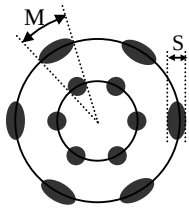

Figure 7.5 *Widths of the diffraction peaks due to crystal mosaic structure (M) and Scherrer broadening (S).*

The widths of the peaks in Figs. 7.2 and 7.4 are directly related to the perfection of the crystal and the quality of the instrument. The crystal perfection and instrument quality find expression in different widths, as illustrated in Fig. 7.5. In Fig. 7.2, we see that the peak width along circles increases with order of the peaks, whereas the widths perpendicular to these circles do not depend on the indices *hkl*. The increase in width along the circles is a result of mosaic structure, *i.e.* slight variations in lattice orientation throughout the crystal. Mosaic structure causes a spreading of the reciprocal lattice points on spheres of constant *s* in reciprocal space, as illustrated in Fig. 7.5. The variation in angle in Fig. 7.2 is only 0.75°. The width perpendicular to the circles does not increase with *s*, which indicates that there is no strain in the crystal. This perpen-

dicular width is due to the resolving power Δs of the instrument. The widths along the Bragg rods in Fig. 7.4 increase with the order of the rod, again due to the mosaic structure: the Bragg rods in Fig. 7.4 are tangential to the spheres of constant s. In principle the width along the rods could be much smaller than the resolving power Δs in the diffraction pattern, however the resolution is limited by the transverse coherence length of the x-ray beam. The transverse coherence length expresses over what distance a crystallite can still provide a diffraction pattern. This coherence length effectively limits the crystallite size to about 6 μm, leading to Scherrer broadening of the reciprocal lattice points.

The Bragg peaks shown in Fig. 7.2 can be azimuthally averaged to obtain a pattern as a function of the diffraction angle, similar to patterns of polycrystalline samples. It turns out (see chapter 9) that the Bragg diffraction angles are very well explained with fcc lattice spacings. This confirms our observation of fcc diffraction patterns in polycrystalline samples of charge stabilized spheres. We observed single crystal and polycrystalline fcc patterns at densities over the range $20-60$ vol% and at various ionic strengths, *i.e.* at various distances from the melting transition. This is evidence that fcc is indeed the stable phase of dense charge stabilized colloids,[1] in contrast to rhcp or glass, in agreement with theoretical expectations.[19] The observation of the fcc structure has important consequences for photonics[7]: since there are more close-packed directions in fcc crystals than in hcp or rhcp structures (8 rather than 2), the fcc structure has a larger influence on the density of radiating optical states,[20] which results in a larger quantum optical modification of the spontaneous emission rate.[21]

An important feature in the diffraction patterns is the large number of diffraction peaks up to large scattering vectors (Fig. 7.2). This indicates that the Debye-Waller factor is small, which means that the root-mean-square excursions u of the colloidal spheres from their ideal crystal positions are small.[17] For the patterns in Fig. 7.2, we find a u of only 3.5% of the nearest neighbour distance. Bragg peaks correspond to lattice vectors in reciprocal space that play a central role in band structure calculations of the propagation of light through photonic crystals.[13] A high degree of order is crucial for photonic crystals. The observation of a large number of reciprocal lattice vectors means that the optical band structures are well defined up to high optical frequencies.[13]

7.5 Real space structure

The basic goal of a diffraction study is to obtain a real space image of the positions of particles in a crystal. Whereas direct imaging is hampered by the well-known phase problem in diffraction,[17] one can already obtain much insight from Fourier

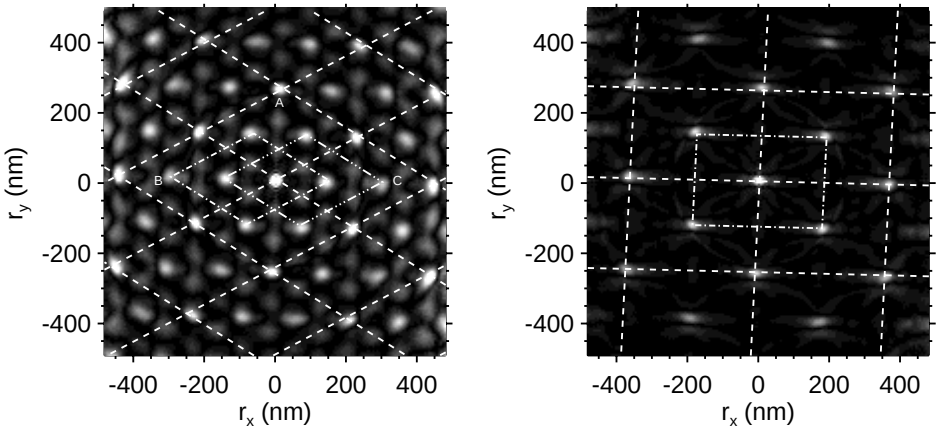

Figure 7.6 *Real space density autocorrelation functions (Patterson maps).* **(a)** *Cubic 111 planes ($\omega = 0$ in Fig. 2A). The hexagonal unit cell with edge lengths equal to the nearest neighbour distance of ~ 260 nm is indicated with dashed lines. The dashed-dotted cell indicated with "B" and the dashed-triple dotted cell indicated with "C" are hexagonal units in planes just above or just below the central "A" plane.* **(b)** *Cubic 110 planes ($\omega = 34^\circ$ in Fig. 2B). The dashed grid indicates the projected square faces of the cubic unit cell, with edges equal to 260 nm and to $\sqrt{2} \times 260$ nm. The dotted rectangle indicates the correlations due to planes above and below the one indicated with dashed lines.*

transforms of the diffraction patterns. In Fig. 7.6a,b, we have plotted the Fourier transforms of Fig. 7.2A and D, respectively. This yields projections of the autocorrelation function of the density in real space, which is a map of the vectors that connect particle positions, known as the Patterson map.[17] These maps are especially useful to elucidate complex structures of non-overlapping particles, typical of colloidal systems. Figure 7.6a shows the Patterson function projected on a plane perpendicular to the cubic 111 axis. The dashed lines indicate the hexagonal close packed plane ('A' in Fig. 7.6a). The clear spots on the corners of each cell indicate the distance to nearest neighbours, and next nearest neighbours in the hexagonal planes. The spots should not be confused with the real space density obtained in a hologram or a microscope image. It is well-known that the fcc structure can be represented as a three layer repeat sequence ABCABC... of close packed layers,[17] thus there are two other planes that are located below and above an 'A' plane. In Fig. 7.6a, these give rise to additional peaks, that are indicated with 'B' and 'C'. Additional correlations at positions in between the ideal lattice points are possibly caused by defects in the crystal mentioned earlier. Figure 7.6b shows the Patter-

son function projected perpendicular to a cubic 110 axis. We have indicated the rectangular pattern with edge ratio $1 : \sqrt{2}$ times the nearest neighbour distance of ~ 260 nm. The cubic 110 direction is vertical (as in Fig. 7.6a), and the cubic 100 direction is now horizontal. The midpoints in the rectangles are caused by particles in planes below and above a particular 110 plane that are displaced by one nearest neighbour distance. The orientation of the unit cell is such that one cubic 110 axis is pointing upward, which means that rows of particles in the close packed planes are parallel to the sedimentation direction. Such an orientation is usually observed in sheared samples,[5] but does not always occur in our samples (cf. Fig. 7.1). The range in real space of the Patterson functions is currently limited to about 500 nm by the shape of the incident beam and the detector response function. The extension to the micron range is anticipated.

7.6 Conclusions

We observe large numbers of Bragg diffraction peaks of photonic colloidal *single* crystals over an unprecedented range of scattering vectors. The colloidal particles order in face centered cubic (fcc) structures at all densities and with a high degree of localization about their lattice sites. The growth and observation of highly ordered fcc crystals strongly support the notion that self-organizing soft condensed matter is a suitable building block for photonic matter. It is thus exciting that there are novel developments to control the growth of colloidal crystals.[22] Moreover, crystals with structures of interest to photonic applications have recently been found in binary mixtures.[23] Our results demonstrate that synchrotron small-angle x-ray scattering with two-dimensional detection (Fig. 7.2) is a powerful technique to investigate systems with length scales on the order of optical wavelengths, especially when they are strongly photonic,[8] in other words strongly multiple scattering.

References

1. P. N. Pusey, in *Liquids, freezing and glass transition*, edited by J. P. Hansen, D. Levesque, and J. Zinn-Justin (North-Holland, Amsterdam, 1991), pp. 763-942. W. C. K. Poon, P. N. Pusey, and H. N. W. Lekkerkerker, 'Colloids in suspense', *Phys. World* **9**, 27-34 (1996).
2. R. J. Hunter, *Foundations of colloid science* (Clarendon, Oxford, 1992).
3. S. John, 'Localization of light', *Phys. Today* **44 (no.5)**, 32-40 (1991).
4. E. B. Sirota, H. D. Ou-Yang, S. K. Sinha, P. M. Chaikin, J. D. Axe, and Y. Fujii, 'Complete phase diagram of a charged colloidal system: a synchrotron x-ray

scattering study', *Phys. Rev. Lett.* **62**, 1524-1527 (1989).

5. B. J. Ackerson, J. B. Hayter, N. A. Clark, and L. Cotter, 'Neutron scattering from charge stabilized suspensions undergoing shear', *J. Chem. Phys.* **84**, 2344-2349 (1986);
   H.
   Versmold and P. Lindner, 'Reinterpretation of small-angle neutron-scattering studies on ordered colloid dispersions', *Langmuir* **10**, 3043-3045 (1994);
   C. Dux, H. Versmold, V. Reus, T. Zemb, and P. Lindner, 'Neutron diffraction from shear ordered colloidal dispersions', *J. Chem. Phys.* **104**, 6369-6374 (1996).
6. S. M. Clarke, A. R. Rennie, and R. H. Ottewill, 'Stacking of hexagonal layers of colloidal particles: study by small-angle neutron diffraction', *Langmuir* **13**, 1964-1969 (1997).
7. K. Busch and S. John, 'Photonic band gap formation in certain self-organizing systems', *Phys. Rev. E* **58**, 3896-3908 (1998).
8. W. L. Vos, R. Sprik, A. van Blaaderen, A. Imhof, A. Lagendijk, and G. H. Wegdam, 'Strong effects of photonic band structures on the diffraction of colloidal crystals', *Phys. Rev. B* **53**, 16231-16235 (1996); ''Erratum", *ibid.* **55**, 1903 (1997). In *Photonic Band Gap Materials*, edited by C. M. Soukoulis (Kluwer, Dordrecht, 1996) p. 107.
9. L. A. Feigin and D. I. Svergun, *Structure analysis by small-angle x-ray and neutron scattering* (Plenum, New York, 1987).
10. S. Dosho, N. Ise, K. Ito, S. Iwai,H. Kitano, H. Matsuoka, H. Nakamura, H. Okumura, T. Ono, I. S. Sogami, Y. Ueno, H. Yoshida, and T. Yoshiyama, 'Recent study of polymer latex dispersions', *Langmuir* **9**, 394-411 (1993);
    O. Diat, P. Bösecke, C. Ferrero, A. K. Freund, J. Lambard, and R. Heintzmann, 'Ultra-small-angle x-ray scattering with a Bonse-Hart camera on the high brilliance beamline at the ESRF', *Nucl. Instrum. Meth. A* **356**, 566-572 (1995).
11. W. B. Russel, P. M. Chaikin, J. Zhu, W. V. Meyer, and R. Rogers, 'Dendritic growth of hard sphere crystals', *Langmuir* **13**, 3871-3881 (1997).
12. E. Yablonovitch, 'Inhibited spontaneous emission in solid-state physics and electronics', *Phys. Rev. Lett.* **58**, 2059-2062 (1987);
    S. John, 'Strong localization of photons in certain disordered dielectric superlattices', *ibid.* **58**, 2486-2489 (1987).
13. *Development and applications of materials exhibiting photonic band gaps*, edited by C. M. Bowden, J. P. Dowling, and H. O. Everitt. ", *J. Opt. Soc. Am. B* **10**, special issue (1993).
14. P. Bösecke, O. Diat, and B. Rasmussen, 'High-brilliance beamline at the European Synchrotron Radiation Facility', *Rev. Sci. Instrum.* **66**, 1636-1638 (1995).

15. L. Mandel and E. Wolf, *Optical coherence and quantum optics* (Cambridge, Cambridge, 1995).
16. J. P. Moy, A. P. Hammersley, S. O. Svensson, A. Thompson, K. Brown, L. Claustre, A. Gonzales, and S. McSweeney, 'A novel technique for accurate intensity calibration of area x-ray detectors at almost arbitrary energy', *J. Synchrotron Radiat.* **3**, 1-5 (1996).
17. A. Guinier, *X-ray diffraction in crystals, imperfect crystals, and amorphous bodies* (Dover, New York, 1994).
18. The patterns observed as a function of angle of incidence are best viewed on the movie animation, which is available on URL 'http://pubs.acs.org/cgi-bin/suppinfo.sh?langd5/13/6004'.
19. M. O. Robbins, K. Kremer, and G. S. Grest, 'Phase diagram and dynamics of Yukawa systems', *J. Chem. Phys.* **88**, 3286-3312 (1988).
20. R. Sprik, B. A. van Tiggelen, and A. Lagendijk, 'Optical emission in periodic dielectrics', *Europhys. Lett.* **35**, 265-270 (1996).
21. E. Yablonovitch and T. J. Gmitter, 'Photonic band structure: The face-centered-cubic case', *Phys. Rev. Lett.* **63**, 1950-1953 (1989).
22. M. M. Burns, J.-M. Fournier, and J. A. Golovchenko, 'Optical matter: Crystallization and binding in intense optical fields', *Science* **249**, 749-754 (1990);
J. X. Zhu, M. Li, R. Rogers, W. Meyer, R. H. Ottewill, STS-73 space shuttle crew, W. B. Russel, and P. M. Chaikin, 'Crystallization of hard-sphere colloids in microgravity', *Nature* **387**, 883-885 (1997);
A. van Blaaderen, R. Ruel, and P. Wiltzius, 'Template-directed colloidal crystallization', *Nature* **385**, 321-323 (1997).
23. P. Bartlett, R. H. Ottewill, and P. N. Pusey, 'Superlattice formation in binary mixtures of hard-sphere colloids', *Phys. Rev. Lett.* **68**, 3801-3804 (1992).

8
X-ray scattering of colloidal spheres

8.1 Introduction

Knowledge of the size and internal structure of the particles in a colloidal crystal is of critical importance for photonic applications; for example, the density profile inside the spheres is directly related to the refractive index, which determines the photonic band structure. A thorough understanding of scattering from individual particles is essential for the interpretation of diffraction patterns from groups of particles, *e.g.* colloidal crystals.[1] Surprisingly, the internal structure of colloidal particles is seldom investigated.

Here we present a synchrotron small-angle x-ray scattering study of colloidal particles that are widely used, namely polystyrene latex and two types of silica spheres. Although the use of x-ray scattering for characterizing colloids has been known already since the early 1950s,[2–5] it does not seem to have found widespread application,[6] in spite of the fact that the technique has several major advantages: it probes a wide range of length scales, it allows us to probe inside the particles, the method is *in situ*, and it does not suffer from multiple scattering.

The potentials of small-angle x-ray scattering have been demonstrated by Ballauff *et al.*[7] and in the use of ultra-small angle scattering by *e.g.* Dosho *et al.*[8] Recently, x-ray scattering is rejoicing in a growing interest, stimulated by results such as those presented here. Surprisingly, synchrotron sources have hardly been used until a few years ago, in spite of pioneering work by Sirota *et al.*[9] and Chang *et al.*[10] Modern synchrotron sources[11,12] are ideally suited for small-angle scattering. These sources have a high brilliance, so the acquisition time can be short (fractions of a second); they deliver a highly monochromatic beam which is tightly collimated and has a narrow focus, so the angular resolution is high. In combination with the high dynamic range of the detector, this makes synchrotron small-angle x-ray scattering an ideal tool for the study of colloidal systems.

8.2 Experiments

We have studied several different kinds of colloidal particles of various radii. Silica spheres were grown by Stöber synthesis[13] or by polymerization in a microemulsion,[14,16] and were kindly provided by A. van Blaaderen[15,16] and A. Imhof.[17,18] Polystyrene colloids were obtained from Duke Scientific or kindly provided by J. Verhoeven.[19] Table 8.3 at the end of this chapter summarizes the names and origins of the various colloidal systems. The particles were suspended in various solvents (water, methanol, ethanol, or dimethylformamide) by successively diluting and centrifuging. The final volume fraction of the diluted suspensions was usually 0.1% or less to prevent effects from particle interactions.

The colloidal suspensions were sealed in glass capillaries. For this purpose we employed 2 mm diameter round capillaries with 0.01 mm thin walls (Hilgenberg) and flat capillaries with a 0.3 or 0.4 mm inside path length and 0.3 mm thick walls (Vitro Dynamics). Because colloidal crystals usually have their close-packed planes parallel to the walls of the capillary, it is advantageous to use flat capillaries. Therefore we have also tried to measure diffraction patterns from dilute suspensions in the flat, thick-walled capillaries, but this resulted in a much higher background.[20] Most of the results that we present derive from diffraction patterns taken with thin-walled capillaries.

8.3 Particle radii

Figure 8.1 shows the experimentally determined scattering cross section as a function of scattering vector s for dilute suspensions of the different kinds of particles studied: polystyrene, Stöber grown silica, and microemulsion-grown silica spheres. The cross sections vary over more than 5 orders of magnitude. For weakly scattered radiation like x-rays, the amplitude of the scattered radiation is the coherent sum of contributions from different parts of a particle (Rayleigh-Gans scattering[21]). The intensity of the scattered radiation has its maximum in the forward direction ($s = 0$) where all contributions are in phase. Away from the forward direction the cross section gradually decreases because contributions from different parts of the sphere start to interfere destructively. The interference gives rise to fringes in the cross section as a function of s, that are clearly illustrated in Fig. 8.1. The radius r of the spheres can be determined with high accuracy, and *in situ*, from the positions of the fringes. The presence of a large number of fringes indicates that the spheres are nearly monodisperse, because even a moderate ($\sim 10\%$) size polydispersity (standard deviation of the radius divided by the mean) almost completely washes out the fringes.

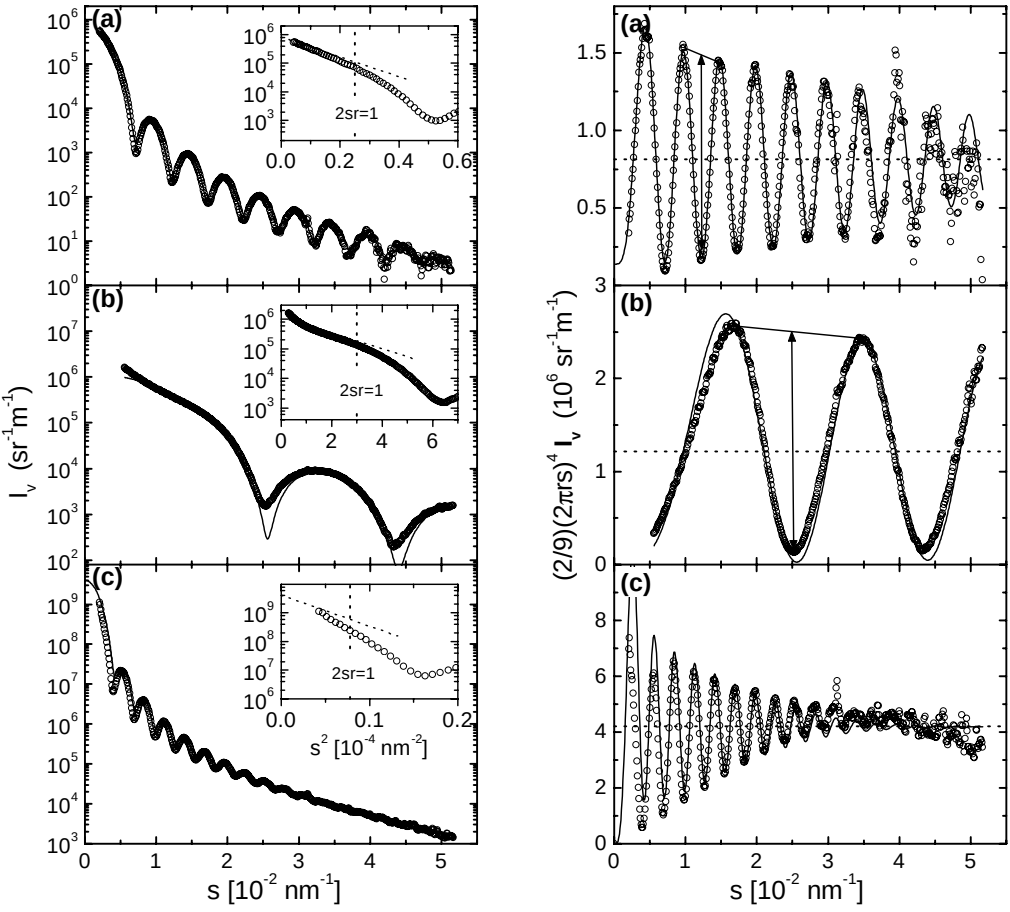

Figure 8.1 *Scattering cross section I_v as a function of scattering vector $s = 2\sin(\theta)/\lambda$ for dilute suspensions of spheres, plotted semilogarithmically (left panels) or on a linear scale and multiplied by s^4 (Porod plot, right panels): (a) polystyrene in methanol (polystyrene-1); (b) microemulsion-grown silica in dimethylformamide (microemulsion-2); (c) Stöber grown silica in water (silica-2). The solid lines are model curves for spheres of homogeneous internal density, taking into account size polydispersity and detector blurring. The presence of a large number of fringes indicates that the sizes of the spheres are highly monodisperse. The polydispersity can be determined from the fringe amplitude (arrow) as a function of s. If the scattering cross section is multiplied by $(2/9)(2\pi sr)^4$ instead of s^4, then the average height of the fringes ($\cdots$) yields the cross section in the forward direction ($s = 0$). This cross section can also be obtained from the Guinier plots (inset). The dotted lines with a slope of $(2\pi r)^2/5$ in the Guinier plots have been drawn using the radii deduced from the fringe period.*

To gain a further understanding of the particle shape, we consider the exact expression for the differential scattering cross section of a single homogeneous sphere of radius r with a sharp edge[5,11,22]

$$I(s) = I_e N_e^2 \Phi^2(2\pi sr). \tag{8.1}$$

Here I_e is the cross section for a single electron (a constant), r is the radius of the sphere, $N_e = (4/3)\pi r^3 \Delta n_e$ is the number of excess electrons in the sphere with respect to the surroundings, and Δn_e is the difference in electron density. The angular dependence of the cross section is determined by the spherical Bessel function $j_1(x)$

$$\Phi(x) = 3j_1(x) = 3\frac{\sin(x) - x\cos(x)}{x^3}. \tag{8.2}$$

Beyond the first fringe ($x > \pi$), the square of the Bessel function decreases as $[1 + \cos(2x)]/x^4$. The fourth power of s causes the variation of I over 5 orders of magnitude in Fig. 8.1. The radius and polydispersity can be conveniently obtained by presenting the data in a Porod plot (Fig. 8.1), *i.e.* multiplied by s^4 and on a linear scale. For perfect spheres the resulting curves should go like $\cos(4\pi rs)$ at large rs. The experimental curves indeed look like a sine, but the oscillations gradually decrease with increasing s, as a consequence of the polydispersity of the spheres. The positions of the minima and maxima in the Porod plot are determined by the average sphere radius and hardly affected by a small polydispersity. Hence, the radius of the spheres can be very accurately determined by plotting the positions of the minima and maxima. The resulting plot for the polystyrene spheres is shown in Fig. 8.2. The slope of the line corresponds to half the inverse radius. We have obtained a radius of the spheres in suspension of $r = 100.9 \pm 0.5$ nm, close to the radius specified by the manufacturer, $r = 99$ nm. The statistical errors in the radii thus determined are on the order of only 0.5 %, which clearly illustrates the potential of the method.

We have obtained radii for many colloidal systems of nearly monodisperse spheres. The nature of the various systems, along with radii determined by x-ray scattering and other methods, and the polydispersities are summarized in table 8.1. For some colloids we have measured the radius in several solvents. The radii were identical within experimental uncertainty,[23] which indicates that the spheres do not swell in the liquids that we have used. The radii determined by x-ray scattering for the polystyrene systems are in excellent agreement with the radii specified by Duke Scientific. The radii obtained by static light scattering also closely correspond, as expected because light scattering and x-ray scattering are basically the same techniques.[21] We take the excellent agreement as a validation of the x-ray technique. The radii determined by transmission electron microscopy are systematically on the

order of 10% lower than the other results, probably because the particles are dried so they shrink, and the electrons sometimes degrade the material. There is a considerable variation in these radii. One would expect that radii can be determined with high accuracy using electron microscopy, because it is possible to determine quite small polydispersities (down to a few percent) with this technique. The variation suggests that different colloidal systems shrink by different amounts. Radii determined by dynamic light scattering, based on measuring Doppler shifts due to Brownian motion of the particles, tend to be higher than the radii determined by the other methods. This has been observed previously[10]; possibly the spheres drag some extra liquid along with them, for instance due to interactions with counterions which are in solution. Furthermore, there is a considerable variation in the data, on the order of 10%. It has been shown previously that dynamic light scattering is rather sensitive to the presence of surfactants, salts, and the volume fraction of the colloid,[24] which may explain the variation in the radii. However, if one makes ev-

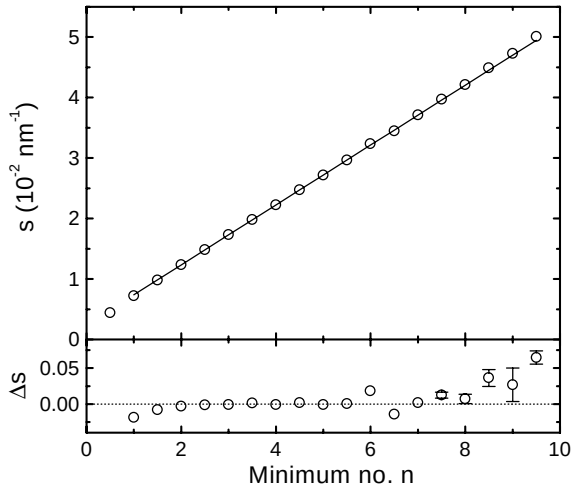

Figure 8.2 *Positions of the minima and maxima in the Porod plot (Fig. 8.1a) versus the order of the minimum (n) or maximum ($n+1/2$). The slope of the fit (—) yields the radius, $r = 100.9 \pm 0.5$ nm, in excellent agreement with the value specified by the manufacturer,* 99 *nm. The lower panel shows the small difference between the datapoints and the fit in the upper panel. Note that the simple straight line is not expected to accurately predict the position of the first maximum (leftmost data point).*

ery effort it is possible to determine very accurate radii using dynamic light scattering.[25] This is clearly demonstrated by the excellent agreement between x-ray radii and the results of Duke Scientific, which were obtained by dynamic light scattering.

8.4 Size polydispersity

For monodisperse spheres, the curves in Fig. 8.1 should go like $1+\cos(4\pi rs)$ at large rs, but the amplitude of the observed modulations decreases with increasing s as a consequence of the polydispersity of the spheres. The form factors of spheres with different radii are identical, but the horizontal scale is different. The scattered intensities of individual spheres add, but with the fringes shifted, so the fringes average out. The fringes at high s are shifted more (in the absolute sense), so they average out more easily. Thus the decrease of the fringe amplitude is a measure of the polydispersity.[26]

If the polydispersity is small, the distribution of radii closely resembles a Gaussian.[27] For a Gaussian distribution, the average cross section can be calculated analytically if we assume that the electron density is the same for all spheres. It appears that the oscillating terms in Φ^2 decrease with a factor $\exp[-2(2\pi rs\delta)^2]$, where δ is the polydispersity, *i.e.* the standard deviation of the radius divided by the mean. This is a very useful result, because it provides a straightforward method to determine the polydispersity from the amplitudes of the fringes in a Porod plot, as we will demonstrate below. The method that we present here is both quantitative and convenient, as it eliminates the need for elaborate fitting procedures.

In Fig. 8.3 we have plotted the amplitude of the fringes in Fig. 8.1a as a function of $(rs)^2$. Such a semilogarithmic plot should give a straight line, except at low s, near the first maximum in the Porod plot.[28] Indeed the fringe amplitudes in Fig. 8.3 agree with a straight line. From the slope of the line we find a polydispersity $\delta = \Delta r/r = 2.3 \pm 0.3\%$, excellent agreement with the polydispersity specified by Duke Scientific, $\delta = 2.1\%$. It shows that x-ray scattering is well suited to accurately determine small polydispersities (below 5%). We stress that our characterization of the particle size distribution is an *in situ* technique, as opposed to techniques that are normally used, such as transmission electron microscopy.[29]

There are several experimental effects which may also affect the amplitude of the fringes in Fig. 8.1, namely the polychromaticity of the x-rays, the finite focus spot size, the beam divergence and the finite detector resolution. Only polychromaticity has the same influence as a polydispersity of the spheres. Fortunately, the relative spectral width of the source is approximately 1.5×10^{-4}, which is completely negligible compared to polydispersities of colloidal dispersions ($> 10^{-2}$). For comparison, in small-angle neutron scattering the relative spectral width is of-

Thin walled capillaries; wavelength $\lambda = 0.147\ 25$ nm

System	r_{TEM}	r_{SAXS}	r_{SLS}	r_{DLS}	δ_{TEM}	δ_{SAXS}
polystyrene-1		100.9(5)[b]		99[f]	2.1[f]	2.3(3)
silica-1	114	138(3)[c d]	148(7)	161		2
silica-2	156	178.5(7)[c d]	178(5)	216	3.6	3.05(5)
silica-2		184.0(4)[e]				2.9(1)
silica-4	89.4	94.9(1.6)[d]	107.2(3)		6	5.5(2)
silica-5	179	199.0(1.8)[d]	200(3)	188(5)	5.5	4.4(3)
silica-6	187	211.4(5)[e]	211(1)	213(3)	4.0	2.4(2)
microemulsion-1		82.0(4)[c]	79.5			1.3(1)
microemulsion-2	25.7	28.0(5)[c]			1.5	
microemulsion-3		26.3(5)[c]				

Thick walled capillaries; wavelength $\lambda = 0.098\ 80$ nm

System	r_{TEM}	r_{SAXS}	r_{SLS}	r_{DLS}	δ_{TEM}	δ_{SAXS}
polystyrene-2		102.0(3)[b e]		101.5[f]	2.1[f]	
polystyrene-3		111.8(3)[e]		111 [f]	2.0[f]	
polystyrene-4		120.8(5)[e]		120.5[f]	1.6[f]	
polystyrene-5	198.5[g]	200.6(5)		211.5		
silica-1[a]	114	144(2)[e]	148(7)	161		
silica-2	156	185.5(1.3)[e]	178(5)	216	3.6	
silica-3	208	248.4(1.1)	241(7)	260		
microemulsion-2	25.7	27.8(4)[c]			1.5	
microemulsion-3		26.7(5)[c]				

[a] These spheres consist of a core of 101 ± 2 nm and a 37 ± 2 nm thick shell of lower density.
[b] In methanol; [c] In dimethylformamide; [d] In water; [e] In ethanol.
[f] Specified by Duke Scientific; [g] SEM instead of TEM.

Table 8.1 *Radii r (in nanometers) and polydispersities δ (in percent) for a number of colloidal systems, obtained by transmission electron microscopy (TEM), small-angle x-ray scattering (SAXS), static light scattering (SLS), or dynamic light scattering (DLS).*

ten of the order of 0.1; hence this completely dominates the polydispersity of the spheres. The other effects, *i.e.* the focus size at the sample, the beam divergence, and the finite detector resolution, all affect the fringes in the following way: the measured diffraction pattern is equal to the ideal pattern, convoluted with the profile of the direct beam. This convolution corresponds to small shifts of the diffraction pattern; because all fringes shift by equal amounts, they are all affected equally. It appears that due to these effects the fringe amplitude decreases by a factor which is independent of s. Thus it is possible to separate the influence of polydispersity and the instrument response, because the dependences on s of the effects are different. The abscissa of the line in Fig. 8.3 is a measure of the r.m.s. width Δ of the beam profile. We find $\Delta = 0.72 \pm 0.10$ mm. This is in reasonable agreement with the experimentally determined width of the direct beam on the detector, which is $\Delta = 0.60$ mm (horizontally) and 0.38 mm (vertically).

The polydispersities for several dilute colloidal systems of nearly monodisperse spheres have been determined using small-angle x-ray scattering, see table 8.1. The ratio of polydispersities determined by electron microscopy and by x-ray scattering is plotted in Fig. 8.4. For comparison, we have also included the polydispersity from dynamic light scattering discussed above. The polydispersities from electron microscopy are consistently larger than the corresponding polydispersities from x-ray scattering.[30] The discrepancy gradually becomes larger with decreasing

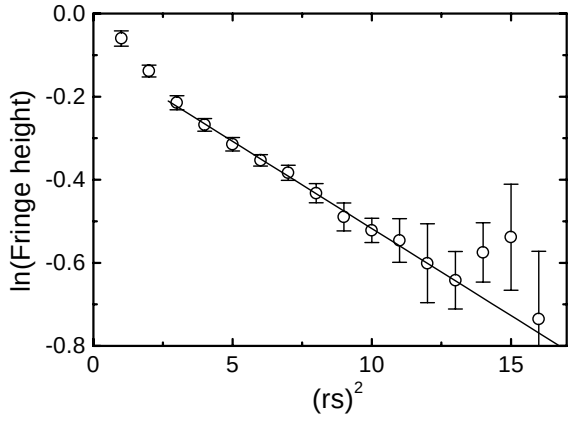

Figure 8.3 *Amplitude of the fringes in Fig. 8.1a, normalized to the average height, as a function of* $(rs)^2$. *The fringe amplitude decreases as* $\exp[-2(2\pi rs\delta)^2]$, *which is a straight line in this plot. The slope of the fit (—) yields the polydispersity,* $\delta = 2.3 \pm 0.3\%$, *in excellent agreement with the polydispersity specified by the manufacturer,* $\delta = 2.1\%$.

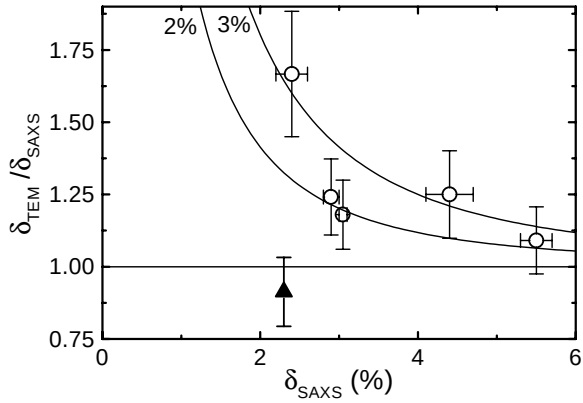

Figure 8.4 *Ratios of the polydispersities determined by transmission electron microscopy (○) or dynamic light scattering (▲) to the polydispersities determined by x-ray scattering, as a function of the latter. The polydispersities determined via scattering (▲) are in excellent agreement. The polydispersities from electron microscopy are consistently higher,*[30] *which is probably due to the random error in the determination of the radius of each individual sphere. The two curves indicate the expected overestimation of the polydispersity in the case of a* 2% *or* 3% *random error in the determination of the radii by electron microscopy.*

polydispersity. This can be explained from the method to determine polydispersities by electron microscopy. These polydispersities are determined by measuring the diameters of a large number of particles on a grid and calculating the variance. The polydispersity is then computed as the root of the variance (*i.e.* the standard deviation) divided by the mean diameter. However, the variance of the measured diameters is not equal to the variance of the distribution of diameters but also includes an additional contribution due to the random error in the determination of the diameters of the individual spheres. Because the magnification of the microscope is usually adjusted according to the size of the particles, one would expect the absolute error to be proportional to the particle size. The resulting observed polydispersity is then $\delta_{obs} = \sqrt{\delta_{true}^2 + \delta_{err}^2}$, where δ_{true} is the true polydispersity of the particles and δ_{err} is the uncertainty in a measurement divided by the particle size. We have calculated this δ_{obs} assuming that the x-ray polydispersity is correct and for a relative random error δ_{err} in the observed radii of 2 and 3%. The resulting polydispersity ratios are plotted in Fig. 8.4. The agreement with the experimentally observed ratio is striking. Hence we conclude that the small polydispersities determined by electron microscopy are probably too high; *i.e.*, they are rather an upper bound for the true polydispersity of the particles.

8.5 Particle-medium interface

Measuring the scattering cross section out to large scattering vector s, *i.e.* more than just one fringe, in principle yields information at small length scales. Some details have a pronounced effect on the diffraction pattern, even if the deviation from a perfect sphere of homogeneous density is small, for instance the presence of a smooth edge instead of a sharp one. So far we have assumed that the particles have a sharp edge, *i.e.* that the electron density abruptly changes at the interface to the medium. A smooth interface reveals itself immediately in the scattering cross section, as can be readily shown using the convolution theorem. The electron density of a particle with a smooth interface region can be constructed mathematically as the convolution of the electron density of a particle with a sharp edge and a smooth function which describes the blurring at the edge. The corresponding scattering cross section is the cross section of the particle with a sharp edge multiplied by the squared Fourier transform of the blurring function. If we take a Gaussian with a small width for the blurring function, then the cross section is multiplied by a broad Gaussian, so it starts to decrease faster than s^{-4} at high s. In a Porod plot like Fig. 8.1, spheres with a sharp edge would show a function which oscillates around a constant value, while the function would gradually decrease at high s if the edge were smooth. Note that the decrease affects the cross section as a whole, not just the oscillating terms as with polydispersity, so the effects of a smooth edge and polydispersity can be separated.

Since the Porod cross section in Fig. 8.1 oscillates around a constant value, we conclude that the edges of these spheres are rather sharp. Considering the average Porod cross section of the polystyrene spheres to be constant to within a fraction $\varepsilon = 10\%$ over the whole range of s in the figure, we estimate the width σ of the interface-blurring Gaussian in reciprocal space from $[\exp(-s^2/2\sigma^2)]^2 = 1-\varepsilon$. Taking $s = 5\times10^{-2}$ nm^{-1}, the upper bound for the thickness of the edge is $1/(2\pi\sigma) = 1.0$ nm, so the density indeed changes abruptly at the edge of the polystyrene spheres. Similar values are obtained for Stöber-synthesized silica. For silica surfaces, the edge layer has been reported[31] to have a thickness of $1-2$ nm, in agreement with our result. The method just described could be a valuable means of studying the phase separation of a mixture of two liquids at the surface of colloidal particles. The preferential adsorption of one of the fluids on the surface near the critical point of wetting is of fundamental importance.[32]

8.6 Electron Density

The forward scattering cross section $I(s \to 0)$ is related to the difference in electron density of the medium and of the particles, Δn_e, and the size and number of spheres in the scattering volume.[11] We can estimate the volume fraction φ of spheres in the liquid from the cross section per unit volume I_v using

$$\varphi = \frac{3}{\Delta n_e^2 4\pi r^3} \frac{1}{r_e^2} I_v. \tag{8.3}$$

The electron densities can be estimated from the number of atomic masses per proton M/Z and the mass density ρ. The densities for relevant materials are listed in table 8.2. The radius is determined with high accuracy from the positions of the minima and maxima in the Porod plot, see Fig. 8.2. However, it is difficult to measure the forward scattering cross section because of the presence of the unscattered beam.

To estimate the forward cross section, the experimental cross section is extrapolated to $s = 0$ using a Guinier plot, as shown in the insets of Fig. 8.1. The slope of $(2\pi r)^2/5$ in the Guinier approximation is determined by the radii estimated from the fringes, *cf.* table 8.1. The inset of Fig. 8.1a reveals an excellent agreement between the data and the Guinier approximation. The excellent agreement also demonstrates that there are no saturation effects of the detector. Saturation effects usually occur near the beam stop and would reveal a decrease at small s and a deviation from the straight line. For the microemulsion-grown silica (Fig. 8.1b) the Guinier slope is also in good agreement with the data, except for a small deviation at small s. This is possibly due to a small number of coagulated spheres ("dumbbells") that occur in microemulsion-grown dispersions[16] and that were detected by TEM. These composite particles are larger; hence, they give rise to scattering at low s. Furthermore the cross section of these particles is larger, proportional to the volume of the particle, which explains why a small number of them is detectable. In Fig. 8.1c, the Guinier slope is in moderate agreement with the data. We have no explanation for the not so good agreement in Fig. 8.1c in comparison with Figures 8.1a and 8.1b.

The forward scattering cross section can also be derived from the Porod plot, as a check. The average height of the fringes in a Porod plot should correspond to the scattering cross section extrapolated to $s = 0$ in the semilogarithmic plots of Fig. 8.1. The data on polystyrene spheres in this figure give a forward scattering cross section of 8.2×10^5 sr^{-1}m^{-1}, in good agreement with the Guinier estimate of $7.5 \pm 0.4 \times 10^5$ sr^{-1}m^{-1}. However, the calibration of the absolute intensities was probably incorrect during the first run, and this affects the measured cross sections. In a later run we have repeated our measurements on the polystyrene colloids in ethanol, paying due attention to the determination of absolute intensities. We have

Table 8.2 *Electron densities n_e of relevant colloidal materials and suspending liquids, estimated from the atomic mass per proton M/Z and the mass density* ρ.

Material	Structure	M/Z	ρ (g/cm^3)	n_e (e$^-$/nm^3)
Methanol	CH_3OH	1.78	0.81	272
Ethanol	C_2H_5OH	1.77	0.79	267
Dimethylformamide	C_3H_7NO	1.83	0.95	311
Polystyrene latex	C_8H_8	1.86	1.00-1.05	322-338
Water	H_2O	1.80	1.00	333
Silica (colloidal)	SiO_2	2.00	1.9-2.0[13,17,34]	570-600

prepared suspensions with volume fractions of 0.1%. From the forward scattering cross section we derived a difference in electron density of polystyrene and ethanol of 66, 89, and 67 nm^{-3} respectively, in excellent agreement with the expected value of 66 ± 8 nm^{-3}, *cf.* table 8.2. This shows that absolute intensities can be measured accurately.

The scattering cross section of polystyrene-water systems is very low, because the electron density of the most common solvent, water, is very closely matched to that of polystyrene. The weak scattering of this ubiquitous colloidal system may well be a reason why there have been so few reports on small-angle x-ray scattering and colloids. For the polystyrene-3 spheres in water we have determined the forward scattering cross section to be less than 1.5×10^3 sr^{-1}m^{-1} at a volume fraction φ of 0.1%, which corresponds to a difference in electron density of the polystyrene spheres and water of less than 2%. The associated mass density of the colloidal polystyrene is 1.03 ± 0.02 g cm^{-3}, in good agreement with the density quoted by Duke Scientific, 1.05 g cm^{-3}.

Knowing the cross section in the forward direction, the radius, and the polydispersity, it is possible to calculate the complete scattering cross section as a function of s. These theoretical cross sections are shown as solid curves in Fig. 8.1. The width of the detector profile is taken into account. The agreement with the experimentally observed cross sections is very good, especially for the polystyrene system, where it extends over more than 5 orders of magnitude. Only for the microemulsion-grown silica there are some small discrepancies, possibly caused by the presence of "dumbbells". We conclude that the cross sections of both polystyrene and Stöber silica systems are completely consistent with those of homogeneous, nearly monodisperse spheres with a sharp edge. Such a comparison of experimental and theoretical cross sections is quite a severe test, as will be demonstrated in the next section.

8.7 Internal structure

An attractive capability of x-ray scattering is the ability to examine the density profile in the spheres, *e.g.* to see whether the spheres consist of shells of different density. In such situations one traditionally resorts to contrast matching with a suitable suspension liquid,[1,7] which is indispensable for detecting small density differences. Here, we show that it is in some cases possible to detect inhomogeneities even without matching. This is probably due to a considerable density difference.

As an illustration, the Porod cross section of a dilute suspension of silica-1 spheres is shown in Fig. 8.5. These spheres have had no special treatment, but the cross section is totally different from the cross sections of the other spheres, *cf.* Fig. 8.1. Similar silica systems (for instance silica-2) give scattering patterns in accordance with that of homogeneous spheres, so there is something peculiar only with the silica-1 system. As a check, we measured diffraction patterns for the same silica-1 spheres in different liquids and at several different volume fractions, but the cross sections appeared identical.

Silica spheres are often synthesized in steps, growing additional layers of sil-

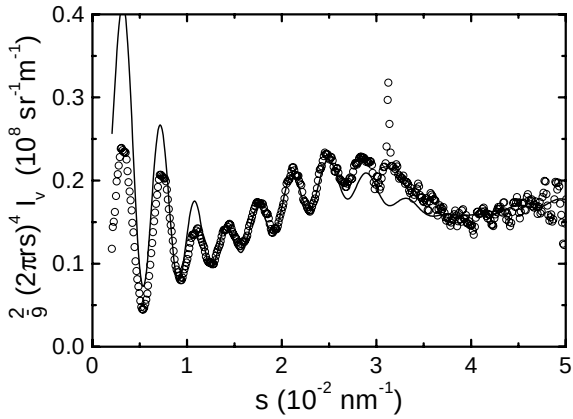

Figure 8.5 *Porod plot of the scattering cross section I_v as a function of scattering vector s for a dilute suspension of silica-1 spheres in water. The minimum in the fringe amplitude around* 1.5×10^{-2} *nm*$^{-1}$ *and the large wavelength modulation are likely caused by a core-shell structure. The solid line is a model of spheres with a homogeneous core (radius* 101 *nm) and a thin, less dense outer shell (thickness* 37 *nm). The model captures the essential features of the observed scattering cross section.*

ica on smaller particles until the desired diameter is reached. A density difference between the core and the additional layers would show up as an extra oscillation, as in Fig. 8.5. The scattering cross section of a core-and-shell sphere can be easily calculated using the result for a homogeneous sphere (Eqs. 8.1 and 8.2): the excess electron density of the core-with-a-shell sphere can be made up of two homogeneous spheres with different radii and densities,

$$I_{\text{core-shell}} = I_e N_e^2 \left[(1-\nu)\Phi(x) + \nu(1+b)^3 \Phi((1+b)x) \right]^2, \qquad (8.4)$$

where $x = 2\pi rs$ with r the radius of the core, d is the thickness of the shell, $b = d/r$ is the thickness of the shell as a fraction of the core radius, N_e is the number of excess electrons in the core, and ν is the electron density difference between the shell and the liquid as a fraction of the core excess electron density difference.

We have plotted the cross section for such a core-and-shell sphere in Fig. 8.5, taking into account polydispersities for the core radius and shell thickness, their correlation, and the blurring due to the finite resolving power of the instrument. The calculated curve represents the observed scattering cross section reasonably well, although there are some discrepancies at small and large s. These may be caused by additional shells or density gradients in the spheres.

The calculated scattering cross section corresponds to spheres with a core radius r of 101 ± 2 nm and a shell thickness d of 37 ± 2 nm, in good agreement with radii measured by static light scattering before and after the last synthesis step, 101 ± 7 and 148 ± 7 nm. From the relative electron density difference $\nu = 81 \pm 3\%$ and the electron densities of water and silica in table 8.2 we estimate that the shell has an $8 \pm 2\%$ lower mass density than the core. This is a sizeable difference in density, considering that the layers were grown using the same synthesis method. On the other hand, there is a comparable variation in the experimentally determined densities of colloidal silica.[13,17,33,34]

8.8 Conclusions

We have shown that the technique of synchrotron small-angle x-ray scattering is very well suited for the characterization of colloidal spheres. The size of colloidal spheres can be determined *in situ* and with high accuracy. We have determined the radii of many different kinds of colloidal spheres from the positions of the minima and maxima of the differential scattering cross section as a function of wavevector. The radii are in excellent agreement with those determined by static light scattering. Electron microscopy consistently yields radii that are smaller and dynamic light scattering yields radii that are larger than the radii determined by x-ray scattering.

We have presented a straightforward method to deduce the size polydispersity of nearly monodisperse (polydispersity $< 10\%$) spheres from a Porod plot of the differential scattering cross section, thus eliminating the need for elaborate fitting procedures. A comparison with polydispersities determined by electron microscopy shows that the new method makes it possible to accurately determine even very small polydispersities ($\sim 2\%$). Our data suggest that polydispersities determined by electron microscopy are an upper bound to real polydispersities.

We have shown that it is possible to study details of the spheres, for instance the sharpness of the outer edge of the spheres. The thickness of the edge of polystyrene spheres of 100 nm radius was estimated to be less than 1 nm. Similar thicknesses are observed for silica spheres, in agreement with observations on silica surfaces. Thus, picturing polystyrene and silica spheres as objects with an abrupt edge is justified.

A Guinier plot was used to determine the forward scattering cross section, which in turn yields the volume fraction or the excess electron density of the spheres. The excess electron densities of several systems including the closely matched system polystyrene and water were obtained, in good agreement with literature data.

Using our data, we have calculated the scattering cross section as a function of wavevector, assuming that the spheres are homogeneous and that they have a sharp edge. The agreement of the calculated curves with the experimentally observed cross sections is excellent, especially for the polystyrene system where it extends over 5 orders of magnitude.

As an example of a more complicated system, we have discussed a suspension of silica spheres which show a peculiar modulation in the cross section, caused by an inhomogeneous intraparticle density. The qualitative features of the cross section were captured by supposing that the spheres consist of a core surrounded by a shell of less dense material. This is a reasonable assumption because the spheres were synthesized by growing additional silica layers on smaller particles. The core radius is in agreement with the size determined before the last synthesis step using static light scattering. The core radius, the shell thickness, and the ratio of the density of core and shell could be obtained even without contrast matching with the suspension liquid, *i.e.*, *in situ*.

References

1. R. H. Ottewill, 'Small-angle neutron scattering from colloidal dispersions', *J. Appl. Crystallogr.* **24**, 436-443 (1991).
2. K. L. Yudowitch, 'Latex particle size from x-ray diffraction peaks', *J. Appl. Phys.* **22**, 214-216. (1951).

3. W. E. Danielson, L. Shenfil, and J. W. M. DuMond, 'Latex particle size determination using diffraction peaks obtained with the point focusing x-ray monochromator', *J. Appl. Phys.* **23**, 860-865 (1952).
4. B. R. Leonard, J. W. Anderegg, P. Kaesberg, and W. W. Beeman, 'The size of latex particles by x-ray scattering', *J. Appl. Phys.* **23**, 152 (1952).
5. A. Guinier and G. Fournet, *Small-angle scattering of x-rays* (Wiley, New York, 1955).
6. Traditionally, colloidal systems are studied with small-angle neutron scattering.[1] Science Abstracts 1995 yields only 9 references when searched for the keywords "SAXS" and "colloid", while for "SANS" and "colloid" there are over 50 references.
7. M. Ballauff, J. Bolze, N. Dingenouts, P. Hickl, and D. Potschke, 'Feature article: Small-angle x-ray scattering on latexes', *Macromol. Chem. Phys.* **197**, 3043-3066 (1996);
   P. Hickl and M. Ballauff, 'Interpretation of the structural parameters derived from the analysis of polymer colloids by small-angle x-ray and neutron scattering', *Physica A* **235**, 238-247 (1997);
   N. Dingenouts, J. Bolze, D. Potschke, and M. Ballauff, 'Analysis of polymer latexes by small-angle x-ray scattering', *Adv. Polym. Sci.* **144**, 1-47 (1999); and many references therein.
8. S. Dosho, N. Ise, K. Ito, S. Iwai,H. Kitano, H. Matsuoka, H. Nakamura, H. Okumura, T. Ono, I. S. Sogami, Y. Ueno, H. Yoshida, and T. Yoshiyama, 'Recent study of polymer latex dispersions', *Langmuir* **9**, 394-411 (1993);
   T. konishi and N. Ise, 'Single crystal of colloidal silica particles in a dilute aqueous dispersion as studied by a two-dimensional ultrasmall-angle x-ray scattering', *Phys. Rev. B* **57**, 2655-2658 (1998).
9. E. B. Sirota, H. D. Ou-Yang, S. K. Sinha, P. M. Chaikin, J. D. Axe, and Y. Fujii, 'Complete phase diagram of a charged colloidal system: a synchrotron x-ray scattering study', *Phys. Rev. Lett.* **62**, 1524-1527 (1989).
10. J. Chang, P. Lesieur, M. Delsanti, L. Belloni, C.; Bonnet-Gonnet, and B. Cabane, 'Structural and Thermodynamic Properties of Charged Silica Dispersions', *J. Phys. Chem.* **99**, 15993-16001 (1995).
11. L. A. Feigin and D. I. Svergun, *Structure analysis by small-angle x-ray and neutron scattering* (Plenum, New York, 1987).
12. P. Bösecke, O. Diat, and B. Rasmussen, 'High-brilliance beamline at the European Synchrotron Radiation Facility', *Rev. Sci. Instrum.* **66**, 1636-1638 (1995).
13. W. Stöber, A. Fink, and E. Bohn, 'Controlled growth of monodisperse silica spheres in the micron size range', *J. Colloid Interface Sci.* **26**, 62-69 (1968).
14. K. Osseo-Asare and F. J. Arriagada, 'Preparation of SiO_2 nanoparticles in a non-ionic reverse micellar system', *Colloid Surf.* **50**, 321-339 (1990).

15. A. van Blaaderen, J. van Geest, and A. Vrij, 'Monodisperse colloidal silica spheres from tetraalkoxysilanes: particle formation and growth mechanism', *J. Colloid Interface Sci.* **154**, 481-501 (1992).
16. A. van Blaaderen, *Silica from Synthesis to Application* Mulhouse, France, September 1-4, 1998; A. van Blaaderen, N. A. M. Verhaegh, A. Imhof, and N. Mason, (in preparation).
17. A. Imhof, A. van Blaaderen, and J. K. G. Dhont, 'Shear melting of colloidal crystals of charged microspheres studied with rheology and polarizing microscopy', *Langmuir* **10**, 3477-3484 (1994).
18. A. Imhof, A. van Blaaderen, G. Maret, J. Mellema, and J. K. G. Dhont, 'A comparison between the long-time self-diffusion and low shear viscosity of concentrated dispersions of charged colloidal silica spheres', *J. Chem. Phys.* **100**, 2170-2181 (1994).
19. H. J. Verhey, B. Gebben, J. W. Hofstraat, and J. W. Verhoeven, 'Detection of nanoscale events in dispersed polymer particles containing a charge-transfer fluorescence probe', *J. Polym. Sci. A* **33**, 399-405 (1995).
20. The high background prevented an accurate determination of the polydispersity of the samples in the thick-walled capillaries. The background is especially bothersome at large s. As a result, the obtained scattering patterns are different from those obtained with thin-walled capillaries and do not decrease as s^{-4}, but more slowly.
21. H. C. van der Hulst, *Light Scattering by Small Particles* (Dover, New York, 1957).
22. A. Guinier, *X-ray diffraction in crystals, imperfect crystals, and amorphous bodies* (Dover Publications, New York, 1994).
23. One exception is the silica system SC200, which appears to be 3% larger in ethanol than in water or dimethylformamide. The radius of the SC200 system in ethanol was reproduced in two different runs. We have no explanation for this difference.
24. S. D. Duke, R. E. Brown, and E. B. Layendecker, 'Calibration of spherical particles by light scattering using photon correlation spectroscopy', *Part. Sci. Technol.* **7**, 223-228 (1989).
25. P. N. Pusey and W. van Megen, 'Detection of small polydispersities by photon correlation spectroscopy', *J. Chem. Phys.* **80**, 3513-3520 (1984).
26. This polydispersity includes a contribution due to a possible ellipticity of the particles, because the form factor for an ellipsoid is identical to that of a sphere with an effective radius which varies between the smallest and largest radii of the ellipsoid depending on its orientation.[21]
27. W. F. Espenscheid, M. Kerker, and E. Matijević, 'Logarithmic distribution functions for colloidal particles', *J. Phys. Chem.* **68**, 3093-3097 (1964).

28. The first fringe is expected to be a little bit higher, because the first fringe in a Porod plot of the form factor of a perfect sphere is also higher than the other fringes.
29. R. J. Hunter, *Foundations of colloid science* (Clarendon, Oxford, 1992).
30. The error bars of the polydispersity ratios is based on a relative error in the polydispersities determined by electron microscopy of 10%. The theoretical relative error in this polydispersity is $1/\sqrt{2k-2}$, where k is the number of particle diameters measured; for $k = 50$ the relative uncertainty is $\sim 10\%$. The situation improves only slowly with particle number.
31. G. Vigil, Z. Xu, S. Steinberg, and J. Israelachvili, 'Interactions of silica surfaces', *J. Colloid Interface Sci.* **165**, 367-385 (1994).
32. S. Dietrich, 'New physical phases induced by confinement', *J. Phys.: Condens. Matter* **10**, 11469-11471 (1998) and references therein. A. Hanke and S. Dietrich, 'Critical adsorption on curved objects', *Phys. Rev. E* **59**, 5081-5100 (1999).
33. A. K. van Helden, J. W. Jansen, and A. Vrij, 'Preparation and characterization of spherical monodisperse silica dispersions in nonaqueous solvents', *J. Colloid Interface Sci.* **81**, 354-368 (1981).
34. K. E. Davis, W. B. Russel, and W. J. Glantschnig, 'Settling suspensions of colloidal silica: observations and x-ray measurements', *J. Chem. Soc. Faraday Trans.* **87**, 411-424 (1991).

Table 8.3 Key to the sample designations used in the text.

System	Original name	Source	Ref.
polystyrene-1	PS5020A	Duke Scientific	
polystyrene-2	PS5020A[a]	Duke Scientific	
polystyrene-3	PS5022A	Duke Scientific	
polystyrene-4	PS5024A	Duke Scientific	
polystyrene-5	A11	J. Verhoeven	[19]
silica-1	SC150	C. van Kats	
silica-2	SC200	C. van Kats	
silica-3	SC006	C. van Kats	
silica-4	SBE1/A6	A. van Blaaderen	[15]
silica-5	FSA7	A. Imhof	[17]
silica-6	SAF8	A. Imhof	[18]
microemulsion-1	μESA9.3	A. van Blaaderen	[16]
microemulsion-2	μEc1	C. van Kats	
microemulsion-3	μEc3	C. van Kats	

[a] This dispersion is a different batch than the other PS5020A.

9
Excursions of particles in a colloidal crystal

9.1 Introduction

Understanding how patterns in many-body systems arise from their constituents' interactions remains one of the outstanding problems in physics.[1] The interactions in these systems determine both the structure and the dynamics of the constituent particles. The positions and dynamics can be measured and compared with models for the interaction. The interaction between colloidal spheres has been studied in-depth by Grier *et al.*, who determined the interaction from the random motion of various polystyrene spheres using optical microscopy.[1,2] The observed pair interaction appears to agree reasonably well with the DLVO theory of screened electrostatic interaction.[2,3] However it is a subject of current debate whether or not the interaction among many spheres is simply a sum of pair interactions.[4,5] Furthermore it is important to understand the role of the suspension liquid, *i.e.* how the viscous damping and random forces affect the dynamics.[6]

In systems where many particles interact, like colloidal crystals, the interaction gives rise to sound modes, *i.e.* motions of the particles about their lattice sites. Lindsay and Chaikin,[9] and Hurd *et al.*[10] have studied the dispersion of sound modes sustained by the combined system of particles and suspension liquid in colloidal crystals. The excursions of particles from their lattice sites are directly related to the lattice dynamics. The excursions are important in relation to the melting transition: according to the Lindemann criterion, crystals melt at a specific ratio of the extent of the excursions to the inter particle spacing.[7,8]

The abovementioned studies of the dispersion of sound modes[9,10] were performed on dilute three-dimensional colloidal crystals. In contrast, the Brownian motion of colloidal particles has been observed mostly in two-dimensional layers of colloids near a wall.[1,5,11,12] The sample walls influence the dynamics considerably: measurements of the single particle dynamics in crystalline layers near a

glass wall have revealed a systematic increase of the excursions with increasing distance from the glass plate.[11,12] We have studied bulk three-dimensional colloidal crystals, thus minimizing the effects of the walls of the sample container.[11–13,6] We have systematically mapped out the extent of the excursions as a function of density, by recording small-angle x-ray diffraction patterns of dense colloids as the melting transition is approached. Previous studies focused mostly on dilute samples at a fixed density ~ 5 vol%.[11,12,14]

9.2 Structure factor

We have analysed x-ray diffraction patterns from two samples made of sedimented 100.8 nm radius monodisperse polystyrene spheres (Duke Scientific PS5020A) in methanol. The suspensions were deionized by means of dialysis with ion exchange resin (BioRad AG501-X8) before being introduced in the capillaries. Extra ion exchange resin was added to one of them (sample #236). The density in the capillaries decreases with height. We have determined the height of the crystal-liquid interface by visual inspection of the optical Bragg reflection. The density profile is obtained

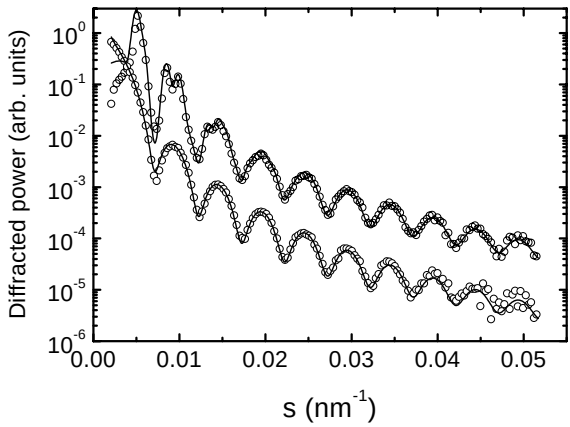

Figure 9.1 *X-ray diffraction patterns from* 100.8 *nm diameter polystyrene colloidal spheres in methanol, at low density (*$<$ 1 *vol%, lower curve, form factor) and crystallized (*45 *vol%, upper curve, sample #232);* ∘*: experiment; —: model. The form factor (lower curve) accounts for the shape of the particles. The diffraction pattern from the crystal (upper curve) also contains information on the crystal structure. Dividing this pattern by the form factor yields the structure factor (Fig. 9.2), in which the influence of the particle shape has been eliminated.*

from the diffraction patterns. Two diffraction patterns from the sample with no extra resin are shown in Fig. 9.1, one from a dilute suspension with a particle density of < 1 vol% and one from a polycrystalline region in the sample with a density of 45 vol%. The diffracted intensities *vs.* scattering vector $s = 2\sin(\theta)/\lambda$ were obtained at an x-ray wavelength λ of 0.147 25 nm. The diffraction patterns have been azimuthally averaged and the background has been subtracted.

To determine the structure factor we measure diffraction patterns from dilute suspensions as well as colloidal crystals. The diffraction pattern from the dilute sample (form factor) shows many interference fringes. From the spacing of the fringes we have accurately determined the size of the colloidal spheres. The presence of a large number of fringes indicates that the spheres all have the same size (polydispersity 2.1%). Because the colloidal spheres are so monodisperse, they readily form crystals at high volume fractions. The crystals produce similar fringes as the dilute suspension, because the shape of the colloidal particles affect both diffraction patterns in a similar way. However the regular spatial arrangement of the spheres in the crystals gives rise to extra features in the diffraction pattern. The effect of particle shape and spatial arrangement can be separated by simply dividing the diffraction pattern of the crystal by that of the dilute suspension. The resulting curve, known as the structure factor, is shown in Fig. 9.2. It consists of the Bragg peaks associated with the crystal lattice. The intensities of the Bragg peaks are related to the r.m.s. displacements u of the colloidal particles from their lattice positions.[15]

9.3 Crystal structure

Many crystal diffraction peaks are observed, as can be seen in Fig. 9.2. The abundance of peaks facilitates determination of the crystal structure and confirms the strong ordering of the colloids. To identify the crystal structure, we compare the diffraction pattern with several likely models.[16] The uppermost vertical ticks under the Bragg peaks of the lower pattern in Fig. 9.2 indicate the expected positions of the lattice spacings of an fcc powder with a lattice parameter a of 322 nm, giving a volume fraction φ of 51 ± 1 vol%. It is seen that the tick positions explain very well the observed Bragg peaks out to $s = 2.5 \times 10^{-2}$ nm^{-1}. Several ticks appear under peaks that are somewhat broader, which can be explained by the resolving power of the instrument Δs of 4.6×10^{-4} nm^{-1}, that causes closely spaced peaks to overlap. The small feature near 0.7×10^{-2} nm^{-1} probably does not originate from the crystals, because it does not shift when all other diffraction lines do. Moreover, it occurs at a position where the form factor has a deep minimum, hence the structure factor is expected to be less reliable here. We have not attempted to index

the features beyond 2.5×10^{-2} nm^{-1}, because they are mostly influenced by the background. For comparison, we also plot in Fig. 9.2 the expected lattice spacings for random stacks of close packed planes with the same volume fraction as the fcc model mentioned above, because this structure has been observed in dense sheared suspensions of charge stabilized samples.[17] The middle set of ticks are the spacings for random stacks with the close packed planes parallel to the cell walls, in other words with the *c*-axis parallel to the x-ray beam. It is clear from Fig. 9.2 that this does not explain the observed peaks. Even changing the unit cell parameter does not improve the correspondence, hence this model is excluded. The lower ticks in Fig. 9.2 are for a powder of randomly stacked close packed planes. This model predicts many diffraction lines, yet several of the observed ones are not explained, *e.g.* the shoulder at 0.6×10^{-2} nm^{-1} (fcc 200) or the peak at 1.2×10^{-2} nm^{-1} (fcc 400). Moreover, many peaks of the randomly stacked model are expected to be broad, on account of the intrinsic disorder of the structure, hence the powder diffraction pattern is expected to have less structure then the one observed. On the basis of the

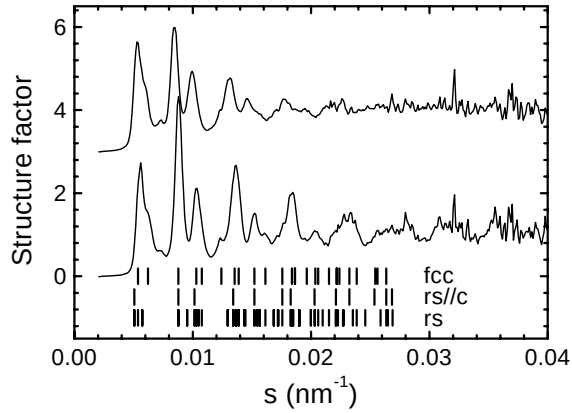

Figure 9.2 *Structure factors of a polycrystalline assembly of polystyrene spheres in methanol (sample #232). The lower curve was measured at the bottom (height* 4 *mm) whereas the upper curve was measured at the top of the sample (height* 14 *mm). The upper curve is obtained from the data in Fig. 9.1. The upper set of ticks indicate the peak positions for a powder of fcc crystals with a cubic lattice parameter a of* 322 *nm. The middle set of ticks are for a random stacking of close-packed planes parallel to the cell walls with a hexagonal lattice parameter of* 228 *nm. The lower set of ticks are for a powder of random stacking of close-packed planes (r.s.) with* $a = 228$ *nm.*

observation of fcc 200 and 400, we can also exclude the hexagonal close packed (hcp) structure. Thus we conclude that fcc is the structure of the colloidal crystals of polystyrene colloids studied here. Our x-ray diffraction results for silica spheres demonstrate that crystals of silica spheres are also fcc ordered.

The observation of all Bragg peaks of fcc in Fig. 9.2 suggests that the sample is a powder, *i.e.* all crystal orientations appear with nearly equal probability. The scattered intensity on the two-dimensional detector showed ringlike features, although incompleteness of the rings indicates a degree of preferred orientation. Indeed the crystals at the cell walls are aligned with the close packed planes (*e.g.* fcc (111)) parallel to the walls as is usual with colloidal crystals: the samples show a bright green (111) reflection. From this combination of SAXS and optical observations, we conclude that the crystal grains deeper inside the capillary, away from the cell walls are the ones that have a random orientation.

9.4 Debye-Waller factor

A quantitative understanding of the observed structure factors can be achieved if we take the heights and widths of the Bragg peaks into consideration. In our case the width of the peaks is dominated by the resolving power of the instrument. The peak heights are determined by the excursions u of the particles from their lattice sites, and by the multiplicities of the reflections, *i.e.* the number of reflections with the same scattering vector. Furthermore there are two geometrical factors: at high scattering vector s relatively few lattice vectors are close to the Ewald plane, and the size of the ring on the detector is larger.[18] These geometrical effects compensate the crowding of reflections at high s, apparent from the ticks in Fig. 9.2. As a result, the peaks in the calculated structure factor coalesce to form a uniform background at large s.

The excursions of the particles from their lattice sites reduce the height of the Bragg peak at scattering vector s by the Debye[19]-Waller[20] factor $\exp(-2M)$, with $M = (2\pi su)^2/6$, assuming that the spatial distribution is a Gaussian with r.m.s. width u, which is appropriate even for hard spheres.[21,22] In solid state physics, one customarily measures the Debye-Waller factor of a single Bragg peak as a function of temperature, and fits this to the Debye model.[18,8] Here the r.m.s. displacements u are obtained directly from the decrease in peak height with increasing scattering vector.[23,14] The intensity that disappears from the Bragg peaks reemerges as a diffuse background $1 - \exp(-2M)$ if the motions of the particles are uncorrelated. Correlations between the particle motions, *i.e.* sound waves, will give structure to the diffuse background, known as thermal diffuse scattering.[18] In dilute colloidal crystals, such a diffuse background has been observed with light scattering

by Rundquist *et al.*.[24] The thermal diffuse scattering will tend to accumulate near the Bragg peaks, the peaks acquire 'feet' of diffuse intensity. Systematic study of this diffuse intensity would reveal the phonon dispersion relation.[20,18] However in our case the Bragg peaks and the diffuse peaks are indistinguishable due to instrumental resolution, so we cannot detect particle correlations. To estimate the importance of phonons, Warren gives an expression for the first order contribution P_{TDS} to the area P_{hkl} of a measured Bragg peak when one naively subtracts a base line.[18] Assuming a linear dispersion relation for the phonons, he finds for fcc crystals the ratio $P_{\mathrm{TDS}}/P_{hkl} \approx Ma\Delta s$, where a is the cubic lattice parameter and $\Delta s \sim 1\ \mu\mathrm{m}^{-1}$ is the total width of the measured peak. From this formula, we infer that our r.m.s. displacements u underestimate the true r.m.s. displacements by about $a\Delta s/4 \sim 8\%$.

We have fitted the model described above to the experimentally determined structure factors, taking into account the extra intensity in reflections from the crystallites aligned with the cell walls. The resulting curve for the sample of Fig. 9.1 is shown in Fig. 9.3. The match with the experimental data is striking; it confirms

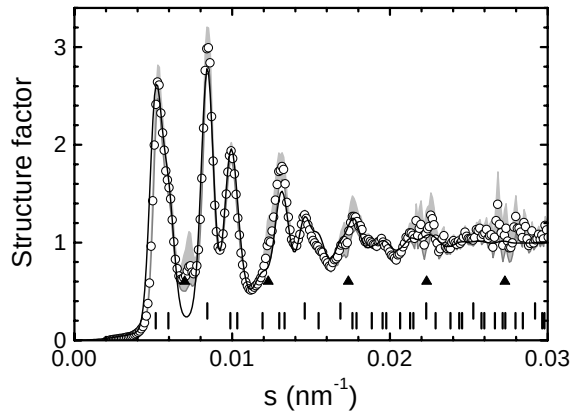

Figure 9.3 *Measured structure factor (∘, same as upper curve in Fig. 9.2) together with a model curve for fcc crystals with* 19.4 *nm r.m.s. displacements of the particles from their lattice sites (—). The shaded area indicates the experimental accuracy, estimated from Poisson counting statistics and the agreement between measured and calculated form factors. The marks at the bottom indicate the peak positions for fcc crystals with a cubic lattice spacing of* 335.5 *nm. The marks which are shifted up correspond to the* $2\bar{2}0$ *family of reciprocal lattice vectors. These lattice vectors intersect the Ewald plane if the* 111 *close-packed planes are parallel to the cell walls. The triangles indicate the minima of the form factor.*

that the crystal structure is indeed fcc. Apart from a straightforward rescaling of the horizontal axis with the lattice spacing and normalization of the vertical axis, the curve is described by only three parameters: the r.m.s. displacement u, the peak width, and the ratio of the intensity due to crystallites aligned with the cell walls and randomly aligned crystallites. For the structure factor in Fig. 9.3 we find a ratio of 2.7. The peaks from the aligned crystallites are relatively strong because the patterns were recorded with the x-ray beam perpendicular to the crystal face, so the Bragg condition is satisfied for all the aligned planes simultaneously. The width of the peaks, $\sigma = 3.8 \times 10^{-4}$ nm^{-1}, agrees well with the measured width of the attenuated direct beam on the detector, $\sigma = 4.0 \times 10^{-4}$ nm^{-1}. From the decrease in peak height with increasing scattering vector we find a r.m.s. displacement u of 19.4 ± 0.5 nm, based on a least-squares fit with weights as indicated by the shaded area in Fig. 9.3.

To put this r.m.s. displacement into perspective, it is desirable to compare it with the separation between neigboring spheres. Fortunately the lattice spacing can be determined with great precision by exploiting all the information contained in the structure factor peaks. From the structure factor in Fig. 9.3, we find a lattice parameter a of 335.5 ± 0.7 nm. In combination with the radius of the spheres $r =$ 100.8 nm determined from the form factor, we deduce the smallest separation in a perfect fcc structure to be 36 nm, suitably larger than the 26 nm full width at half maximum of the distribution of displacements, so the excursions fit in, as expected.

We have determined excursions and lattice spacings at various heights in our colloidal samples. From the lattice spacings and the sphere radius we have deduced the density profile. The results are shown in Fig. 9.4. The extent of the excursions increases almost in proportion to the lattice spacing. The r.m.s. displacements from the two samples form a single curve, although the density profiles in the samples differ considerably. The colloid in sample #236 is more compressible, and it has a lower melting density. According to the pressure equation,[25] an increased compressibility is indicative of a softer potential, *i.e.* a more extended double layer. Indeed the more compressible sample is the one which contains extra ion exchange resin. The reduced melting density also indicates that this sample has a more extended double layer. The presence of an extended double layer would imply that there is less room for excursions at the same density, but the r.m.s. displacements are very similar despite the difference in interaction potential.

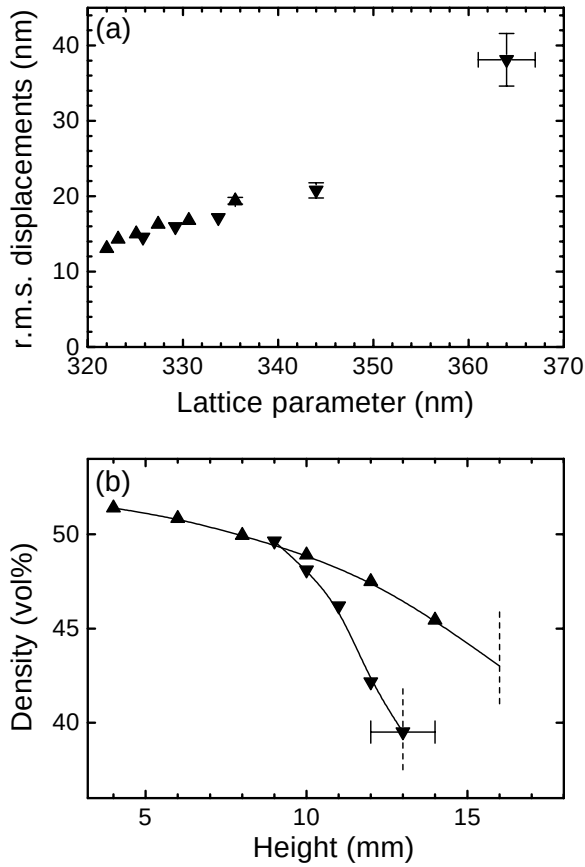

Figure 9.4 *(a) R.m.s. displacements u of the spheres from their equilibrium position, as a function of the cubic lattice parameter, at various heights in two similar samples of polystyrene spheres in methanol (▲: sample #232, ▼: sample #236). (b) The density profiles of these samples. The curves are guides to the eye. The top of the crystalline part of the samples is indicated by dashed lines.*

9.5 Particle excursions

The considerations of available space above are similar to those of Lindemann.[7] In an effort to understand the frequency of vibrations in solids from first principles, he assumed that a solid would melt whenever the amplitude of vibrations became sufficiently large for the hard cores of nearest neighbor atoms to collide. Nowadays, Lindemann's name is often associated with a slightly different criterion. According to this modified criterion, the ratio of the displacements to the nearest neighbor

distance at melting is independent of the system under consideration. This has become widely known as the Lindemann criterion of melting, although it is not the original criterion proposed by Lindemann in 1910.

In the spirit of this Lindemann criterion, we have plotted in Fig. 9.5 the ratio $L = u/d_{\mathrm{nn}}$ of the displacements u to the nearest neighbor distances d_{nn}. As expected, the normalized displacements L increase as we approach the density of melting. At a density of 40 vol%, close to the density of melting of the colloid, the Lindemann ratio L has increased to 0.150 ± 0.015. We have rescaled the horizontal axis of the plot in such a way that it ranges from the density of melting to the close packed density. This rescaling allows us to compare colloidal systems with very different interactions, from strongly charged dilute to dense hard-sphere like systems. The normalized displacements from the two samples form a single curve, although the ionic strengths of the samples differ. The dynamic light scattering results of Piazza and Degiorgio[26] on index matched, charged samples with a melting density of 7 vol% are in good agreement with our results. Also, one data point de-

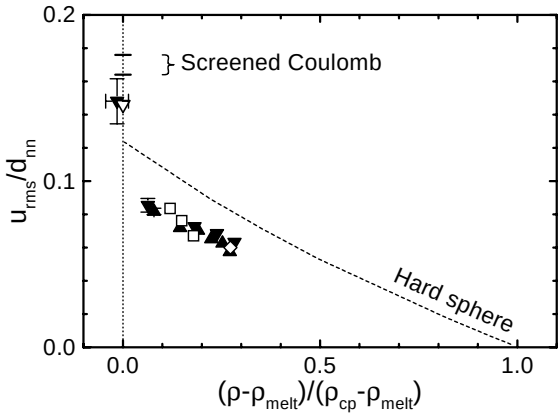

Figure 9.5 *R.m.s. displacements u of the spheres from their equilibrium position, scaled to the distance d between centers of neighboring spheres, as a function of density, obtained from the data in Fig. 9.4 (▼, ▲). The horizontal axis has been rescaled in such a way that it ranges from the density of melting (the density at the top of the crystalline part of the sediment, see Fig. 9.4b) to the close packed density (74 vol%). As a consequence, the dynamic light scattering results of Piazza and Degiorgio*[26] *(□) and Zhu* et al.[27] *(◇) scale exactly onto our data points. The static light scattering result of Bierbaum* et al.[14] *(▽) agrees well with our Lindemann ratio.*

rived from an experiment by Zhu *et al.*[27] on sterically stabilized particles agrees very well with our data. Apparently, when plotted in this fashion, the relation between the excursions and the particle density is insensitive to the interparticle interaction. Previously, it has been suggested that differences in ionic strength are responsible for observed variations in the normalized displacements.[11]

For hard spheres, calculated normalized displacements are available for a range of densities above the melting transition.[21] We have included these in Fig. 9.5 for comparison. The measured excursions are clearly smaller than the hard-sphere results, even if we take into account an 8% increase because of thermal diffuse scattering. Correcting the excursions for the 2.1% size polydispersity of our spheres would increase this discrepancy. Because of the good agreement between the experimental results on different colloidal systems, it seems unlikely that the type of interaction (*i.e.*, screened Coulomb or hard sphere) can remedy the discrepancy.[28] Perhaps, many-body interactions play a role[5] or the presence of a suspension liquid affects the dynamics.[6]

Our Lindemann ratio at the density of melting of 0.15 is clearly higher than the normalized displacements well in the solid phase. Bierbaum *et al.*[14] have obtained a Lindemann ratio in a very dilute (0.19 vol%) bcc crystal of 0.146, in very good agreement with our Lindemann ratio. The experimental data are slightly smaller than numerical predictions for spheres with a screened Coulomb interaction.[6,29] Numerical simulations for fcc crystals with various ionic strengths, properly extrapolated to infinite system size, predict Lindemann ratios in the range 0.164–0.176.[29] The experimental Lindemann ratios are clearly higher than the computer simulation result for hard spheres.[21] Remarkably, however, the observed excursions at higher densities are consistently lower than the hard-sphere normalized displacements.

9.6 Conclusions

We conclude that small-angle x-ray diffraction makes it possible to study systematically the approach to melting of colloidal crystals. This valuable scattering technique complements recently developed methods based on direct imaging of the particles with microscopy using visible light.[1,5,11,12] Microscopy generally works best for larger particles since they probe larger length scales. X-ray diffraction allows the investigation of optically opaque, high density colloids. Diffraction offers excellent statistics: the results are based on very large numbers of particles, $\sim 10^8$. The majority of these particles are far away from the sample cell wall, *i.e.* in the bulk of the crystal. Thus surface effects are eliminated. We find that the excursions in our crystals of charge-screened colloidal spheres are generally smaller

than the hard-sphere results. The difference might be caused by many-body interaction among the spheres,[5] or the presence of a suspension liquid could play a role.[6] It would be fruitful to perform lattice dynamics calculations for screened Coulomb pair interactions at various screenings and densities to compare with the results presented here.

Measurements on colloidal single crystals open up the prospect of studying the thermal diffuse scattering, revealing the spectrum of sound modes in these crystals. Recently x-ray diffraction also has been extended to dynamic measurements, analogous to dynamic light scattering, by exploiting the interference of coherent x-rays.[30–32] With this dynamic technique it is possible to determine not only the extent of the excursions, but also the associated diffusion coefficient.

From the photonic materials perspective, the study of particle excursions by x-ray diffraction is of considerable importance since it offers a measure of crystal quality. Control over crystal quality is crucial for applications of photonic crystals, and the degree of perfection of photonic crystals is expected to become ever more important as the refractive index contrast is increased. Indeed small-angle x-ray diffraction recently has been applied to confirm the lattice perfection of a periodic structure of air holes in a solid host material.[33]

References

1. C. A. Murray and D. G. Grier, 'The microscopic dynamics of freezing in supercooled colloidal fluids', *J. Chem. Phys.* **100**, 9088-9095 (1994);
   C. A. Murray, and D. G. Grier, 'Video microscopy of monodisperse colloidal systems', *Annu. Rev. Phys. Chem.* **47**, 421-462 (1996).
2. J. C. Crocker and D. G. Grier, 'Microscopic measurement of the pair interaction potential of charge-stabilized colloid', *Phys. Rev. Lett.* **73**, 352-355 (1994); 'When like charges attract: effects of geometrical confinement on long-range colloidal interactions', *ibid.* **77**, 1897-1900 (1996).
3. W. R. Bowen and A. O. Sharif, 'Long-range electrostatic attraction between like-charge spheres in a charged pore', *Nature* **393**, 663-665 (1998).
4. A. E. Larsen and D. G. Grier, 'Like-charge attractions in metastable colloidal crystallites', *Nature* **385**, 230-233 (1997).
5. J. A. Weiss, A. E. Larsen, and D. G. Grier, 'Interactions, dynamics, and elasticity in charge-stabilized colloidal crystals', *J. Chem. Phys.* **109**, 8659-8666 (1998).
6. M. O. Robbins, K. Kremer, and G. S. Grest, 'Phase diagram and dynamics of Yukawa systems', *J. Chem. Phys.* **88**, 3286-3312 (1988).
7. F. A. Lindemann, 'Über die Berechnung molekularer Eigenfrequenzen', *Phys.*

Zeitschr. **11**, 609-612 (1910).
8. *Rare Gas Solids*, edited by M. L. Klein and J. A. Venables (Academic, London, 1977).
9. H. M. Lindsay and P. M. Chaikin, 'Elastic properties of colloidal crystals and glasses', *J. Chem. Phys.* **76**, 3774-3781 (1982).
10. A. J. Hurd, N. A. Clark, R. C. Mockler, and W. J. O'Sullivan, 'Lattice dynamics of colloidal crystals', *Phys. Rev. A* **26**, 2869-2881 (1982).
11. J. Bongers and H. Versmold, 'Microscopic investigations of the single particle dynamics in colloidal crystals', *J. Chem. Phys.* **104**, 1519-1523 (1996).
12. J. Bongers, H. Manteufel, K. Vondermassen, and H. Versmold, 'Video microscopy: investigations of the structure and dynamics of colloidal dispersions', *Colloids and surfaces A* **142**, 381-385 (1998).
13. S. Tandom, R. Kesavamoorthy, and S. A. Asher, 'Image charge effects on colloidal crystal ordering', *J. Chem. Phys.* **109**, 6490-6496 (1998).
14. A. Bierbaum, C. H. Dux, and H. Versmold, 'Observation of the Debye-Waller factor in a colloidal single crystal', *Mol. Phys.* **93**, 615-618 (1998).
15. A. Guinier, *X-ray Diffraction in crystals, imperfect crystals, and amorphous bodies* (Dover, New York, 1994).
16. P. N. Pusey, in *Liquids, freezing and glass transition*, edited by J. P. Hansen, D. Levesque, and J. Zinn-Justin (North-Holland, Amsterdam, 1991), pp. 763-942.
17. C. Dux, H. Versmold, V. Reus, T. Zemb, and P. Lindner, 'Neutron diffraction from shear ordered colloidal dispersions', *J. Chem. Phys.* **104**, 6369-6374 (1996).
18. B. E. Warren, *X-ray diffraction* (Addison-Wesley, Reading, MA, 1975).
19. P. Debye, 'Interferenz von Röntgenstrahlen und Wärmebewegung', *Ann. d. Physik* **43**, 49-95 (1914).
20. I. Waller, 'Zur Frage der Einwirkung der Wärmebewegung auf die Interferenz von Röntgenstrahlen', *Zeit. f. Physik* **17**, 398-408 (1923).
21. D. A. Young and B. J. Alder, 'Studies in molecular dynamics. XIII. Singlet and pair distribution functions for hard-disk and hard-sphere solids', *J. Chem. Phys.* **60**, 1254-1267 (1974).
22. A. Kyrlidis and R. A. Brown, 'Model for density-functional thermodynamic perturbation analysis of Lennard-Jones solids', *Phys. Rev. E* **47**, 427-438 (1993).
23. C. A. Burns and E. D. Isaacs, 'Debye-Waller factor in solid ^{4}He crystals', *Phys. Rev. B* **55**, 5767-5771 (1997).
24. P. A. Rundquist, R. Kesavamoorhty, S. Jagannathan, and A. Asher, 'Thermal diffuse scattering from colloidal crystals', *J. Chem. Phys.* **95**, 1249-1257 (1991).
25. J. P. Hansen and I. R. McDonald, *Theory of simple liquids* (Academic, London,

1986).
26. R. Piazza and V. Degiorgio, 'Single-particle dynamics in a colloidal crystal', *Phys. Rev. Lett.* **67**, 3868-3871 (1991).
27. J. X. Zhu, P. M. Chaikin, M. Li, W. B. Russel, W. V. Meyer, and R. B. Rogers, *OSA Conference 'Photon Correlation and Scattering'*, Capri, Italy, August 21-24, 1996; J. X. Zhu, M. Li, R. Rogers, W. Meyer, R. H. Ottewill, STS-73 space shuttle crew, W. B. Russel, and P. M. Chaikin, 'Crystallization of hard-sphere colloids in microgravity', *Nature* **387**, 883-885 (1997).
28. E. J. Meijer and D. Frenkel, 'Melting line of Yukawa system by computer simulation', *J. Chem. Phys.* **94**, 2269-2271 (1991).
29. M. J. Stevens and M. O. Robbins, 'Melting of Yukawa systems: a test of phenomenological melting criteria', *J. Chem. Phys.* **98**, 2319-2324 (1993).
30. S. B. Dierker, R. Pindak, R. M. Fleming, I. K. Robinson, and L. Berman, 'X-ray photon-correlation spectroscopy study of brownian-motion of gold colloids in glycerol', *Phys. Rev. Lett.* **75**, 449-452 (1995).
31. T. Thurn-Albrecht, W. Steffen, A. Patkowski, G. Meier, E. W. Fischer, G. Grübel, and D. L. Abernathy, 'Photon correlation spectroscopy of colloidal palladium using a coherent x-ray beam', *Phys. Rev. Lett.* **77**, 5437-5440 (1996);
T. Thurn-Albrecht, G. Meier, P. Müller-Buschbaum, A. Patkowski, W. Steffen, G. Grübel, D. L. Abernathy, O. Diat, M. Winter, M. G. Koch, and M. T. Reetz, 'Structure and dynamics of surfactant-stabilized aggregates of palladium nanoparticles under dilute and semidilute conditions: Static and dynamic x-ray scattering', *Phys. Rev. E* **59**, 642-649 (1999).
32. D. O. Riese, W. L. Vos, G. H. Wegdam, F. J. Poelwijk, D. L. Abernathy, and G. Grübel, 'Photon correlation spectroscopy: x-rays versus visible light', submitted to *Phys. Rev. E*.
33. J. E. G. J. Wijnhoven and W. L. Vos, 'Preparation of photonic crystals made of air spheres in titania', *Science* **281**, 802-804 (1998);
M. S. Thijssen, R. Sprik, J. E. G. J. Wijnhoven, M. Megens, T. Narayanan, A. Lagendijk,and W. L. Vos, 'Inhibited light propagation in photonic air-sphere crystals', *Phys. Rev. Lett.* **Oct.**, (1999).

Samenvatting

Dit proefschrift gaat over licht in zogeheten fotonische kristallen, materialen die de voortplanting van licht beïnvloeden door hun structuur. Het doel van fotonische kristallen is om als het ware een kooi voor licht te verwezenlijken. Zo'n ingrijpende verandering van de voortplanting van licht is niet alleen vanuit een wetenschappelijk standpunt interessant, maar ook van belang voor bijvoorbeeld de telecommunicatie. In de moderne telecommunicatie wordt veel gebruik gemaakt van licht, om snel grote hoeveelheden gegevens te transporteren via glasvezels. In de toekomst zal het belang van licht voor de informatievoorziening waarschijnlijk nog toenemen. Er is voorspeld dat de veranderde voortplanting van licht in fotonische kristallen aanleiding zal geven tot vele nieuwe natuurkundige verschijnselen. Controle over de voortplanting van licht biedt bijvoorbeeld de mogelijkheid om het uitzenden van licht te beïnvloeden en zo de efficiency van lasers te verbeteren, of ruis te verminderen onder de grens van het normaal mogelijke.

De voortplanting van licht kan worden beïnvloed door doorzichtige materialen samen te voegen tot een geschikte structuur, en gebruik te maken van interferentie. Fotonische materialen kunnen bijvoorbeeld als spiegel gaan werken. Een belangrijk verschil met gewone spiegels is dat fotonische kristallen ook *binnenin* weerspiegelen: ze weerkaatsen niet alleen het licht dat er van buitenaf op valt, maar ook licht dat van binnen komt. Deze inwenige weerspiegeling kan belangrijke gevolgen hebben voor lichtbronnen binnen fotonische kristallen. Zulke lichtbronnen krijgen hun licht dan meteen teruggespiegeld, waardoor zij nooit licht kunnen uitzenden. Als een bepaalde kleur licht in alle richtingen goed weerspiegeld wordt, dan is die kleur licht opgesloten. Om te begrijpen hoe doorzichtige materialen als spiegel kunnen werken, is het van belang om je te realiseren dat doorzichtige voorwerpen eigenlijk zelden onzichtbaar zijn. Dit komt doordat ze ook licht weerkaatsen. Meestal weerkaatst maar een klein gedeelte van het licht: een etalageruit bijvoorbeeld is op de eerste plaats doorzichtig, al kun je er jezelf ook in weerspiegeld zien. De weerspiegeling is genoeg om de ruit op te merken, maar er weerkaatst veel minder licht dan van een echte spiegel. Om een goede spiegel te maken is véél weerkaatsing nodig.

Om een sterkere reflectie te krijgen, maken we gebruik van het feit dat licht zich gedraagt als golf. Golven kunnen elkaar versterken, als de toppen van de ene golf samenvallen met de toppen van de andere golf, of juist uitdoven, als de toppen van de ene golf samenvallen met de dalen van de andere, zie de figuur. Het verschijnsel

wordt ‘interferentie’ genoemd; het doet zich ook bij licht voor. De afstand tussen opeenvolgende golfdalen van lichtgolven – de golflengte – nemen wij waar als de kleur van het licht. Zichtbaar licht heeft een golflengte van ongeveer 0.0005 mm.

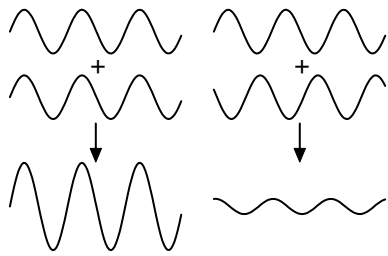

Interferentie: golven die elkaar versterken of uitdoven

Als licht weerspiegelt aan een dun laagje doorzichtig materiaal, ontstaan heldere kleuren als gevolg van interferentie. Een alledaags voorbeeld hiervan zijn de regenboogkleuren die je ziet als er een druppel olie in een plas water terecht is gekomen. De olie spreidt zich uit tot een dunne laag op het water. De lichtgolven die terugkaatsen van het spiegelende wateroppervlak interfereren met lichtgolven die terugkaatsen van het spiegelende olieoppervlak. Ze versterken elkaar of doven elkaar uit, afhankelijk van de dikte van het olielaagje en de golflengte (kleur) van het licht. Wit licht wordt op die manier door de oliefilm opgesplitst in de samenstellende kleuren. De kleuren van parelmoer en de heldere kleuren op de vleugels van vlinders ontstaan op een vergelijkbare manier. In deze gevallen zijn er meer laagjes bij de interferentie betrokken, daarom reflecteert er meer licht en zijn de kleuren feller.

De kleuren van een oliefilm veranderen als je er onder een andere hoek naar kijkt. Zulke veranderende kleuren zijn natuurlijk mooi om te zien, maar onwenselijk als je een bepaalde kleur licht op wilt sluiten. In een fotonisch kristal moet deze kleur licht worden weerkaatst, ongeacht de richting waarin het licht gaat. Dit kan bereikt worden door een ruimtelijke structuur te gebruiken in plaats van dunne laagjes. Omdat het materiaal er dan vanuit verscheidene gezichtspunten vergelijkbaar uitziet, reflecteert het steeds dezelfde kleur.

Om optimaal gebruik te maken van interferentie om de weerkaatsing van een bepaalde kleur te versterken, is het van belang dat de ruimtelijke structuur van fotonische materialen regelmatig is. Onregelmatig opgebouwde structuren zijn gewoonlijk ondoorzichtig wit, zoals matglas of poedersuiker. Door natuurkundigen wordt een regelmatige ruimtelijke structuur gewoonlijk een ‘kristal’ genoemd, naar analogie met de regelmatige rangschikking van atomen in gewone kristallen. De gelijkenis gaat nog verder: vele eigenschappen van gewone kristallen, zoals stroom- en warmtegeleiding, houden verband met hun regelmatige structuur, net als de gewijzigde voortplanting van licht in fotonische kristallen. Deze gelijkenis verklaart de benaming ‘fotonische kristallen’. Materialen met een regelmatige bouw worden niet alleen kunstmatig gemaakt, er zijn ook fotonische kristallen van natuurlijke oorsprong; een voorbeeld is de edelsteen opaal, een opeenstapeling van kleine glazen bolletjes, die zijn glimmende kleuren ontleent aan interferentie.

Wij hebben fotonische kristallen gemaakt van kleine bolletjes in water en daarin de voortplanting van licht onderzocht. We hebben gemeten welke kleuren licht er doorheen gaan en welke weerkaatst worden. De golflengtes van het tegengehouden licht stemmen goed overeen met de afstanden tussen de lagen bolletjes, die bekend zijn uit onze metingen met behulp van Röntgenstraling. Het kleurenbereik van de spiegeling klopt met onze berekeningen. Het blijkt dat er een optimale volumeverhouding bollen:water is waarbij de kristallen zo veel mogelijk kleuren tegelijk weerspiegelen. Als het volume-aandeel water veel groter is dan het volume-aandeel bolletjes of vice versa, dan worden er minder kleuren weerspiegeld. Dit zou men ook verwachten, immers het water en het materiaal van de bolletjes zijn ieder apart gewoon doorzichtig.

Om te zien of fotonische kristallen nu inderdaad invloed hebben op het uitzenden van licht, is het noodzakelijk om lichtbronnen binnenin de kristallen te maken. Hiervoor hebben we bolletjes gemaakt met een fluorescerende kleurstof erin. Zulke kleurstoffen kunnen licht opnemen, en zenden dan specifieke kleuren licht uit. Fluorescerende kleurstoffen zijn echter niet alleen gevoelig voor de weerspiegeling van fotonische kristallen maar ook voor de scheikundige samenstelling van hun omgeving, en de kleurstofmoleculen beïnvloeden elkaar als ze dicht bij elkaar zitten. Daarom hebben we eerst gekleurde bolletjes apart bestudeerd, zonder weerspiegelingseffecten. We hebben gemeten welke kleuren licht de kleurstof uitzond en hoe lang het licht opgeslagen bleef in de kleurstof, voor verschillende hoeveelheden kleurstof in de bolletjes. Het bleek dat een grote hoeveelheid kleurstof een kortere opslagtijd van het licht tot gevolg heeft. De waargenomen variatie in opslagtijden suggereert dat de kleurstof niet gelijkmatig verdeeld is, maar samenklontert binnenin de bolletjes. Deze ongewenste invloeden kunnen vermeden worden door maar een heel klein beetje kleurstof in de bolletjes in te bouwen.

We hebben kristallen met inwendige lichtbronnen gemaakt van glazen bolletjes met een heel klein beetje fluorescente kleurstof erin. De glazen bolletjes zijn allemaal even groot, en zweven rond in een glazen buisje gevuld met water. Onder invloed van de zwaartekracht zakken de bolletjes langzaam naar de bodem van het buisje. Door het uitzakken neemt de dichtheid van bolletjes toe en ontstaan er vanzelf kristallen. De bolletjes stoten elkaar enigszins af doordat ze geladen zijn. Deze afstoting kan verminderd worden door zout aan het water toe te voegen. Extra zout vergroot zowel de snelheid van het naar beneden zakken van de bolletjes als de dichtheid van de uiteindelijke kristallen. Door hier gebruik van te maken hebben we kristallen verkregen met de optimale bolletjes/water-verhouding. De kristallen zijn opzettelijk zo gemaakt dat de kleur van de weerspiegeling overeenkomt met de kleur van de kleurstof.

De invloed van de weerkaatsing binnenin de kristallen op de kleurstof is heel duidelijk merkbaar in de uitgezonden kleuren licht die je buiten het kristal ziet: de

kleur licht die binnenin weerkaatst wordt is een stuk zwakker. De verzwakking blijkt echter minder dan de verzwakking van licht dat van buitenaf komt. uit onze experimenten blijkt dat de verminderde verzwakking niet afhangt van de plaats van de lichtbron in het kristal. Er is meer aan de hand dan alleen maar weerspiegeling van regelmatige lagen bollen: de weerkaatsing aan onregelmatigheden in de kristallen speelt ook een belangrijke rol. Deze onregelmatigheden weerkaatsen licht in willekeurige richtingen. Als gevolg hiervan komt er van alle kleuren licht wel een gedeelte naar buiten, ook van kleuren licht die binnenin weerkaatst worden.

De tijd die het licht in de kleurstof opgeslagen blijft, hebben we ook gemeten. In tegenstelling tot de schakering van uitgezonden kleuren, blijkt de gemeten tijd niet af te hangen van de wisselwerking tussen licht en de fotonische kristallen. Dit is een gevolg van de richtings- en kleurafhankelijkheid van de weerspiegeling van de kristallen. De tijd die verstrijkt tussen het opnemen en uitzenden van licht, de spontane-emissietijd, is een maat voor de mogelijkheden die de kleurstof heeft om licht af te geven. De kleurstof kan in allerlei richtingen en kleuren uitzenden, ook richtingen waarvoor geen weerkaatsing optreedt. Hierdoor blijven er nog genoeg mogelijkheden over om het licht kwijt te raken, en de spontane-emissietijd verandert niet merkbaar.

De kleine glazen bolletjes in water waar we de kristallen van gemaakt hebben, zijn een voorbeeld van een colloïd, een materiaal dat bestaat uit een fijn verdeeld mengsel van twee fasen. Colloïden zijn alom tegenwoordig in het dagelijks leven; slasaus (druppeltjes olie in azijn), gel, inkt (vast stoffen in vloeistoffen), en scheerschuim (gas in vloeistof) zijn er voorbeelden van. Ook het menselijk lichaam bestaat uit colloïden. Colloïden zijn bijzonder geschikt om fotonische kristallen van te maken, aangezien ze van nature ongeveer de juiste grootte hebben en vanzelf kristallen kunnen vormen. Het is echter ingewikkeld om de opbouw van zulke kristallen te achterhalen met behulp van licht, immers de fotonische kristallen zijn bedoeld om de voortplanting van licht te veranderen! Met behulp van Röntgenstraling zijn we er toch in geslaagd om informatie te verkrijgen over de opbouw van colloïdale fotonische kristallen. Hiervoor hebben we experimenten gedaan in Grenoble in Frankrijk, waar een zeer felle Röntgenbron beschikbaar is. Het blijkt dat de kristallen bijzonder goed geordend zijn, honderden bolletjes liggen keurig op rijtjes, zowel in de breedte en hoogte als in de diepte. De experimenten tonen aan dat kleine-hoek Röntgenverstrooing met een synchrotronbron en twee-dimensionale detectie bijzonder geschikt is voor het bestuderen van colloïdale systemen.

Als voortvloeisel van deze zeer nauwkeurige metingen hebben we de groottes, groottevariaties, scherpte van het oppervlak en de dichtheid kunnen bepalen van verschillende soorten colloïdale bolletjes, in hun natuurlijke omgeving. Het blijkt dat de meeste colloïden beantwoorden aan het beeld van homogene, eenvormige

bolletjes met een scherpe rand. De gemeten groottes en groottevariaties komen goed overeen met resultaten van andere technieken, maar zijn nauwkeuriger en volgen uit één enkele meting aan de bolletjes in hun natuurlijke omgeving. Bovendien hebben we een handige nieuwe methode gevonden om zelfs zeer kleine variaties in bolletjesgrootte te kunnen bepalen.

Samenvoeging van bovenstaande Röntgenwaarnemingen levert interessante informatie op over de nauwkeurigheid waarmee de bolletjes op hun plaats zitten in de colloïdkristallen. Vanwege de warmtebeweging maken de bolletjes voortdurend kleine uitstapjes rond hun plaats in het kristal. We hebben systematisch de grootte van deze uitwijkingen in kaart gebracht in kristallen waarin de bolletjes dicht op of juist verder van elkaar af zitten. Opmerkelijk genoeg blijkt dat de uitgestrektheid van de warmtebeweging in allerlei verschillende colloïden voornamelijk bepaald wordt door het verschil tussen de dichtheid van de bolletjes en de dichtheid waarbij de bolletjes geen kristal meer vormen maar wanordelijk door elkaar gaan zitten. Het soort wisselwerking tussen de bolletjes blijkt alleen van belang voor zover het de dichtheid bij de smeltovergang beïnvloedt. Verrassend is ook dat de warmtebeweging minder is dan op grond van berekeningen was verwacht. Wellicht spelen wisselwerkingen tussen meer bolletjes tegelijkertijd een rol, of beïnvloedt de aanwezigheid van een vloeistof de beweging.

Een belangrijk doel van het onderzoek aan fotonische materialen is om een kristal te maken dat ten minste één kleur licht goed tegenhoudt, ongeacht de richting waarin het licht gaat. Dit onderzoek laat zien dat colloïden bijzonder geschikt zijn om fotonische kristallen te maken. Kort geleden zijn er nieuwe fotonische kristallen ontwikkeld die veel meer kleuren weerspiegelen, en in veel meer richtingen tegelijk. Deze kristallen zijn opgebouwd uit van nature al beter weerkaatsende doorzichtige materialen, zoals titaandioxide, dat om deze reden ook gebruikt wordt in de betere kwaliteiten witte verf (“titaanwit”). De kristallen worden gevormd met behulp van een soort mal die bestaat uit een colloïdkristal. Het lijkt aannemelijk dat verdere ontwikkelingen binnen afzienbare tijd zullen leiden tot kristallen met de gewenste volkomen weerspiegeling van tenminste één kleur. Zulke kristallen werken dan als kooi voor die kleur licht.

Dankwoord

Het spreekt vanzelf dat dit werk alleen tot stand kon komen door samenwerking met en hulp van velen. In dit dankwoord wil ik al degenen bedanken die bijgedragen hebben aan dit proefschrift.

Allereerst Ad Lagendijk, mijn promotor, die altijd tijd voor je heeft – een vermeldenswaardige eigenschap voor een promotor, als je de verhalen mag geloven – en pragmatisch is ingesteld, zonder zijn principes uit het oog te verliezen. Ik dank hem voor het gestelde vertrouwen en het enthousiasme.

Willem Vos ben ik bijzonder dankbaar voor alle hulp, en voor alles wat ik van hem geleerd heb, vooral over presentatie, essentieel als je je enthousiasme ook over wilt brengen als de wetenschap eens een keer gestaag, in plaats van zeer spectaculair vordert. Gedeeltes van hoofdstuk 2, 7 en 9 zijn gebaseerd op teksten van zijn hand.

Carlos van Kats wil ik bedanken voor het maken van silica bolletjes en kristallen van uiteenlopende colloïden, en voor de gezelligheid op de colloïdenwinterschool in Han-sur-Lesse. Judith Wijnhoven wil ik bedanken voor het maken van de colloïden met kleurstof, de meer dan honderd kristallen, en talloze metingen daaraan; en voor de gezelligheid en de bezoekjes thuis natuurlijk. Groetjes aan Jip en Diede, en bedankt voor de vele 'post'.

Judith en Carlos hebben de colloïdsyntheses gedaan aan de Universiteit Utrecht, in samenwerking met Alfons van Blaaderen, die specialist is op dat gebied. Alfons dank ik voor de hulp, de vele nuttige opmerkingen en de discussies. Met veel plezier heb ik deelgenomen aan het colloïdenwerkoverleg met Jacob Hoogenboom, Krassimir Velikov, en Alexander Moroz. Alfons en Arnout Imhof wil ik ook bedanken voor het gebruik van colloïden die hij en Arnout eerder gesynthetiseerd hadden. Ook Jan Verhoeven wil ik bedanken, voor zijn belangstelling, en de bolletjes die hij schonk.

Arnout Imhof, Dennis de Lang en Rudolf Sprik wil ik bedanken voor de prettige samenwerking die resulteerde in hoofdstuk 3. De levensduurmetingen in dit hoofdstuk zijn oorspronkelijk gemeten op initiatief van Arnout, en daarna verfijnd door Dennis aan de hand van Rudolf's modelmatige inzichten. Anouk Noordervliet dank ik voor de voortvarende eerste calibratie van de prismaspectrometer.

Henry Schriemer wil ik bedanken voor het enthousiasme en de wetenschappelijke degelijkheid, en voor de prettige samenwerking bij het schrijven van een Comment aan de hand van de levensduurmetingen in hoofdstuk 6. Henry heeft in-

middels fluorescentie gemeten van de nieuwste fotonische kristallen; het was een genoegen om het er met hem over te hebben tijdens het schrijven van dit boekje.

Cor Snoek wil ik bedanken voor het gebruik van enkele van zijn dyes, en voor het lenen van zijn catalogi.

Peter Bösecke en Olivier Diat wil ik bedanken voor alle hulp bij de metingen in het ESRF in Grenoble, samen met het geslaagde team van Willem, Carlos, Judith, Mark, Dirk, en Michiel, in wisselende combinaties. (Zie hoofdstuk 8, 7, en 9.) Speciale dank aan Peter, voor zijn geduldige en bereidwillige uitleg van de finesses van de gas-gevulde detector, en zijn aandacht voor een nauwgezette uitwerking van de metingen.

Gerard Wegdam wil ik bedanken voor zijn enthousiasme en belangstelling (onder andere voor de polydispersiteiten in hoofdstuk 8), en de prachtige verhalen, zowel op wetenschappelijk gebied (vraag hem maar eens naar het 'netje' SF_6 bijvoorbeeld) als maatschappelijk geëngageerd ('Het punt is, *du* moment dat je.… Daar klopt dus helemaal geen *lór* van.'). Menige koffiepauze wordt opgeluisterd door zijn enthousiaste ideeën voor gewaagde nieuwe experimenten.

Rudolf Sprik dank ik voor zijn praktische hulp, bijvoorbeeld bij het temmen van de YAG laser, en voor zijn uitgebreide bibliotheek, waar ik veelvuldig gebruik van heb mogen maken.

Daan Frenkel en Friso van der Veen wil ik bedanken voor hun belangstelling, en voor hun inzichtelijke opmerkingen.

Femius Koenderink wil ik bedanken voor het lezen van het manuscript.

Met Wim Koops heb ik met veel plezier een kamer gedeeld, en veel gelachen met hem, Johan van de Ridder, en Joost Overtoom. Ik wil hen en de andere mensen van de werkplaats graag bedanken voor de vele hulp op technisch gebied – de onvolprezen kunde van de mechanische en elektronische werkplaats is onmisbaar voor het vlot slagen van experimenteel onderzoek.

Speciale dank aan Flip de Leeuw voor zijn hulp met elektronica; aan Eddy Inoeng en Bert Zwart voor hun hulp in de glasblazerij (de glazen capillairen); aan Thijs Post, Henk Pot en Frank Hondeman voor hun hulp met computers; aan Mariet Bos, Ina Zwart en Irma Brouwer voor hun hulp op administratief gebied; en Truus Klebach voor haar fantastische hulp bij het regelen van een promotiedatum.

Verder wil ik mijn leuke collega's bedanken voor de goede sfeer. Op de eerste plaats natuurlijk Frank Schuurmans, voor de vele discussies waarbij we het altijd zo met elkaar eens zijn, de vrijdagmiddagproefjes, en de gezelligheid in de trein naar Utrecht; verder Gijs van Soest, ook een groot vrijdagmiddagexperimentator; Jaime Gomez-Rivas, altijd bereid om gevolg te geven aan de vraag 'Zo, vertel 'ns iets leuks.' op commando; Dirk Riese, die er het zijne van denkt en zich niet van de wijs laat brengen; Michiel Thijssen, een enthousiaste zeiler die wel te vinden is voor een uitstapje; Frank Poelwijk, die altijd tijd heeft, ook als er geen tijd is; De-

nis Fenistein; Johannes de Boer, die mij zijn huis uitleende; Martijn Wubs, die mij opvolgde als huurder; Mark Kroon, voor het logeren en voor definitievere huisvesting – zonder Mark haalde de middagpauze nooit meer het niveau van voorheen; de ‘oude garde’, Pedro de Vries, Rik Kop ‘kat in ’t bakkie’, Peter den Outer, Mark van Rossum, Diederik Wiersma, en Boris Nieuwenhuis; de waterstofgroep, Allard Mosk, Pepijn Pinkse, Tom Hijmans, Meritt Reynolds, Kai Dieckmann, Matthias Weidemüller, Peter Fedichev, Gora Shlyapnikov en Bert Holsbeke; en nog vele anderen.

Nathalie Muller, Ronald van Elburg, Martijn Wubs en Sander Bais wil ik bedanken voor de prettige samenwerking bij het voorbereiden van de werkcolleges en tentamens quantumfysica.

Wel heel speciale dank natuurlijk aan André en Mirjam, mijn ouders, voor alle goede zorgen en de aanmoediging, en aan mijn lieve zus Toeja.

Tenslotte wil ik Feike Hacquebord bedanken voor de vele uitstapjes ter afleiding en de gezelligheid; en natuurlijk het strijkorkest Zoroaster, speciaal Margriet, Marcel, en Nathalie, voor het samenspelen en de ontspanning, voor het aanhoren van alle verhalen en de aanmoediging.

Mischa